

A study of the reaction $\pi^- P \rightarrow N + \text{Photons}$
(A search for the η_c)

Alfred Mike Halling

A DISSERTATION
PRESENTED TO THE
FACULTY OF PRINCETON UNIVERSITY
IN CANDIDACY FOR THE DEGREE
OF DOCTOR OF PHILOSOPHY

RECOMMENDED FOR ACCEPTANCE BY THE
DEPARTMENT OF
PHYSICS

June 1982

I hereby declare that I am the sole author of this thesis.

I authorize Princeton University to lend this thesis to other institutions or individuals for the purpose of scholarly research.

Alfred Mike Halling

I further authorize Princeton University to reproduce this thesis by photocopying or by other means, in total or in part, at the request of other institutions or individuals for the purpose of scholarly research.

Alfred Mike Halling

ABSTRACT

A double arm spectrometer was used to study the reaction $\pi^- P \rightarrow N + \text{photons}$ with beam energies of 5, 8.5, and 13 GeV. The experiment placed a sensitive upper limit on the production cross sections of mesons of narrow width decaying to two photons. No narrow resonances are seen within the mass region of 2.3-3.1 GeV, where an upper limit of 114 pico-barns, 90% confidence level, is placed on the production cross section times branching ratio. This limit conflicts with earlier observations of a state with a mass of 2.83 GeV produced in pion-nucleon collisions, a state that was suggested as the pseudoscalar bound state of a charmed quark and anti-quark, commonly called the η_c . An upper limit of 2.1 nano-barns, 90% confidence level, is placed on the production cross section times branching ratio of narrow resonances near the mass of the E(1420) particle, where there is speculation that a resonance formed by the bound state of two gluons might exist.

ACKNOWLEDGEMENTS

The success of Brookhaven Experiment 732, the subject of this thesis, was brought about by the combined skills and hard work of a large team of physicists and research staff. I am deeply indebted to all those associated with this experiment for their commitment towards making it a success.

My adviser, Professor Stew Smith, played a leading role in shaping the directions the research would follow. His endless enthusiasm for the project helped drive everyone to perform his or her best. Professor Kirk McDonald provided valuable insight necessary in solving the day-to-day problems encountered during the experiment and contributed greatly to the development of the Monte Carlo simulation program. My collaborators from Brookhaven, the Peking Institute of High Energy Physics, and the University of Illinois offered their inspiration and also helped build many crucial portions of the apparatus.

Howard Edwards of the Elementary Particles Laboratory at Princeton designed many parts of the apparatus, including the hodoscope portion of the detector and most of the detector elements in the target region of the experiment, and also supervised their construction at Princeton and assembly at Brookhaven. The skillful machining and excellent workmanship of the staff at the Elementary Particles Laboratory, Walter Bell, Walter Davidson, Nick Diaczenko, Sam Morreale, John Quinn, Richard Rabberman, and William Sands, contributed greatly to the high reliability of the apparatus.

The experiment involved the use of a great deal of custom electronics, most of which was designed by Marius Isailia and built under the supervision of Ann David. Their skillful craftsmanship was responsible for the high reliability and performance of this equipment. Carl Bopp designed and built the large memory buffer used on

the PDP15 computer and also played an important role in keeping that computer running reliably during the course of the experiment.

This work would not have been possible without the support and encouragement of all my friends throughout the course of my research. My warmest thanks go to Linda Coleman, who in addition to her love and faith in me also helped enormously with her careful editing of this manuscript.

TABLE OF CONTENTS

ABSTRACT	iii
ACKNOWLEDGEMENTS	iv

<u>Chapter</u>	<u>Page</u>
I. INTRODUCTION	1
Charmonium	1
The Four Quark Model	3
Current Status of Pseudoscalar States of Charmonium	4
The Goals of This Experiment	5
Hadronic Production of η_c	6
Expected Yield of η_c in Pion Nucleon Collisions	6
II. THE APPARATUS	9
General Layout of Experiment	10
The Target	11
Charged Particle Vetoes	11
Photon Veto Counters	12
Photon Detector Arms	12
Main Trigger Logic	14
Instrumentation	15
Calorimeter Counter Instrumentation	16
Hodoscope Instrumentation	17
Lead Glass Instrumentation	17
Transistor Phototube Base	18
Cable Dispersion Canceling Devices	19
Veto Counter Instrumentation	20
Phototube Gain Tracking Devices	21
Radioactive Sources	22
Light Flasher System	22
Data Acquisition System	23
Setting the High Voltage of the Detector Elements	23
Special Diagnostic Triggers	24
Electron Runs	24
Single Arm Runs	25
III. CALIBRATION PROCEDURES AND FIRST PASS ANALYSIS	26
ADC Pedestal Processing	26
Light Flasher Event Processing	27
Gain Calibration	27
Primary Lead Glass and Calorimeter Counter Calibration Procedures	28
Hodoscope Counter Calibration Procedure	28
Calibration Consistency and Problems	30

	Radioactive Source Processing and Results	30
	Systematic Drifts in the Calibration Procedures	31
	Time of Flight Calibration and Performance	33
	Lead Glass TOF Problems	34
IV.	PATTERN RECOGNITION AND EVENT SELECTION	36
	Pattern Recognition in Detector	36
	Rear Lead Glass Wall Processing	37
	Front Lead Glass Wall Processing	38
	Hodoscope Counter Processing	39
	Calorimeter Processing	40
	Determining the Photon Energies	41
	Distinguishing Between One- and Two-Photon Showers	42
	Measuring the Effectiveness of the Cuts	43
	Measuring Effects of Cuts on Event Quality	44
	Measuring the Background Level	44
	Event Selection - Cuts for Detecting Soft Photons	45
	Veto Counter Cuts	45
	Extra Calorimeter Counter Cuts	45
	Extra Hodoscope Peaks	46
	Extra Hits in the Front Lead Glass Wall	46
	Extra Hits in the Rear Lead Glass Wall	47
	Event Selection - Identifying Symmetrically Decaying π^0 's	47
	Hodoscope - Rear Wall Position Matching Cut	47
	Extra Single Hodoscope Peak Cut	48
	Event Selection - Elimination of Events with Missing Energy	49
V.	MEASUREMENTS OF THE CROSS SECTIONS OF KNOWN RESONANCES	50
	Calculation of Cross Sections	50
	Measuring the Geometrical Efficiency of the Apparatus - The Monte Carlo	50
	Rate Dependence to Acceptance After All Cuts	52
	Effective Number of Target Nucleons	53
	Neutron Self Vetoing	54
	Estimates of Systematic Errors	55
	The Test Run Results	55
	Five GeV/c η'	55
	Five GeV/c η	57
	Eight GeV/c η'	57
	Five GeV/c ω	58
VI.	RESULTS - SEARCH FOR NARROW TWO PHOTON RESONANCES	59
	Feed-down from $\pi^0 \pi^0$ Events	59
	Limits on Narrow $\gamma \gamma$ Resonances in the 1.6 to 1.9 GeV Mass Range	60
	Limits on X(2.83) Production	61
	Limits on Other Narrow $\gamma \gamma$ Resonances in the 2.2 to 3.0 GeV Mass Range	63

Limits on Narrow $\gamma\gamma$ Resonances in the 1.3 to 1.6 GeV

Mass Range	63
Exotic Channels	64
$\eta\pi^0$ Cross Section	65
$\eta\eta$ and $\eta\gamma$ Cross Sections	65
Conclusion	65
Future Prospects	66

Appendix

	<u>page</u>
A. SOLVING HODOSCOPE COUNTER OVERLAP PROBLEMS	68
B. TUNING THE VETO COUNTER CUTS	71
Tuning the Veto Time of Flight Windows	71
Investigation of Uses of the ADC and Latch Information . .	72
C. TUNING THE EXTRA HODOSCOPE COUNTER PEAK CUTS	75
Cuts on Extra Hodoscope Peaks with More Than One Counter .	76
Cuts on Extra Hodoscope Peaks with One Counter	76
Cuts on Extra Hodoscope Peak Pairs	77
D. TUNING THE EXTRA FRONT WALL SHOWER CUT	78
E. PROCESSING OF LONE REAR WALL LEAD GLASS SHOWERS	80

Chapter I INTRODUCTION

1.1 Charmonium

The discovery¹ of the J/ψ in 1974 and its subsequent interpretation as the first evidence for a new family of particles composed of heavy quark anti-quark pairs bound by the strong interaction were major turning points in the investigation of the hadrons and their interactions. Because the charmed quarks are so massive with respect to their binding energy, the properties of their bound states can be described rather well by the non-relativistic treatment of two massive particles in a static potential well. The new particles are simply interpreted as different states of the heavy quark analog of the "positronium atom" of elementary particle physics. The charmonium system², the states formed as bound states of a charmed quark and anti-quark, and the recently discovered Upsilon system³ are therefore excellent testing grounds for the rapidly developing models describing the interaction of quarks.

Figure 1 shows the charmonium system of resonances as it was known in 1979. The standard models had no problems fitting the masses and electromagnetic transition rates between the triplet S states and the P states, but the η_c candidate at 2.83 GeV was in serious disagree-

¹ J. J. Aubert, et al., Phys. Rev. Lett. 33, p1404 (1974).

J. E. Augustin, et al., Phys. Rev. Lett. 33, p1406 (1974).

² There are many excellent reviews of the charmonium system. See for example:

T. Appelquist, R. M. Barnett, K. Lane, Ann. Rev. Nuc. Part. Sci. 28, p387 (1978).

R. J. Cashmore, Progress in Particle and Nuclear Physics 7, p225 (1981).

³ S. W. Herb, Phys. Rev. Lett. 39, p252 (1977).

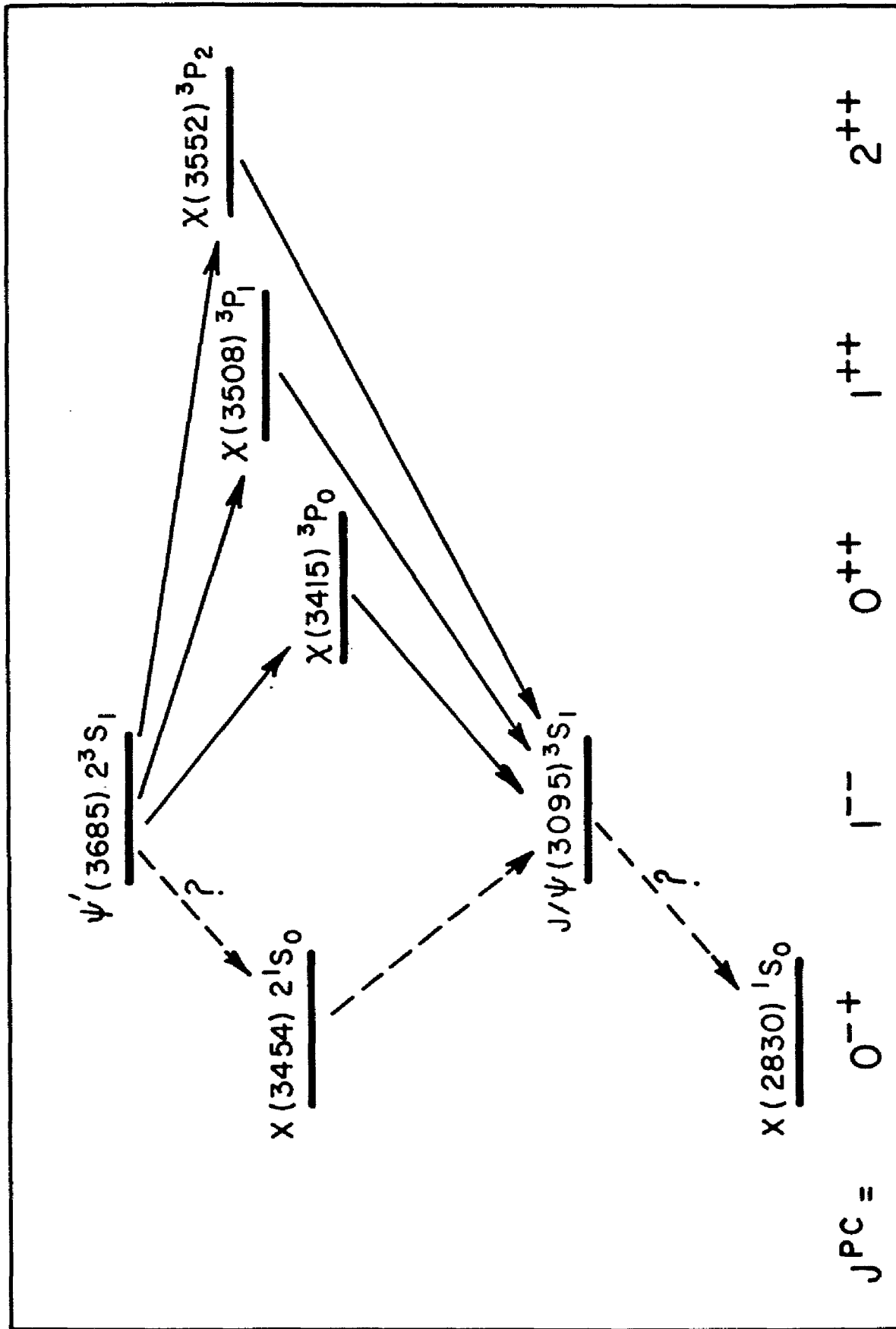


Figure 1 Low Mass Charmonium States and Their Electromagnetic Transitions in 1979

ment with the theoretical predictions. The first evidence for the existence of this state came from two experiments at the DESY storage rings⁴ that observed the decay of the J/ψ into three photons. The energies of the photons, which were not measured, were determined by a 1-constraint fit assuming that they were indeed photons. In this manner both experiments observed evidence for the radiative decay of the J/ψ to the $X(2.83)$ and its subsequent decay into two photons with a rate of:

$$BR(J/\psi \rightarrow X(2.83)\gamma) \cdot BR(X(2.83) \rightarrow \gamma\gamma) = 1.3 \pm .4 \times 10^{-4}$$

Although the observed product of the branching ratios was consistent with the expected value, earlier limits⁵ placed on the first term in the product required both to be at least an order of magnitude from their expected values. In addition, the mass of this state was much lower than that expected for the η_c .

Additional evidence for the existence of the $X(2.83)$ came from a Russian experiment⁶ at the Serpukhov accelerator in the USSR. This group observed a state produced in pion nucleon collisions that had roughly the same mass as the state seen by the DESY groups and that decayed into two photons. The observed cross section times branching ratio for this reaction was about 100 pb at a beam momentum of 40 GeV/c. This cross section was roughly two orders of magnitude larger than that expected from simple estimates⁷, which led several authors to propose that the $X(2.83)$ state was not the η_c but rather an

⁴ B. H. Wiik, Proc. 1975 Int. Symp. on Lepton Photon Interactions, Stanford, Calif., p69.

J. Heintze, Proc. 1975 Int. Symp. on Lepton Photon Interactions, Stanford, Calif., p97.

W. Bartel, et al., DESY Preprint 76/65 (1976).

⁵ C. J. Biddick, et al., Phys. Rev. Lett. 38, p1324 (1977).

⁶ Apel, et al., Phys. Lett. 72B, p500 (1978).

⁷ G. Eilam, B. Margolis, S. Rudaz, Phys. Lett. 80B, p306 (1979).

exotic meson⁷, such as a four quark state⁸ or a $c\bar{c}g$ bound state⁹.

1.2 The Four Quark Model

The standard quark model proposed in 1964 by Gell-Mann¹⁰ and Zweig¹¹ considers the mesons to be formed only of quark anti-quark pairs. A natural expansion of this idea is the formation of mesons with two quark anti-quark pairs, or simply the bound states of two mesons. In 1977 Jaffe¹² not only suggested that states composed of four quarks could exist, but gave rather convincing evidence that some of the most well-known mesons were indeed four quark states. His argument centered on the properties of the $S^*(980)$ and the $\delta(980)$, both of which are within a few MeV of the $K\bar{K}$ threshold but are thought to couple strongly to this channel¹³ and only minimally to light quarks. The $\delta(980)$ is an isovector state, which in the standard quark model must be composed of light quarks, but it decays preferentially¹⁴ into objects with strange quarks. The charmed analog to these states would be bound states of two D mesons as suggested by

⁸ Y. Afek, C. Leroy, V. Margolis, Phys. Lett. 83B, p238 (1979).

H. J. Lipkin, H. R. Rubinstein, N. Isgur, Phys. Lett. 78B, p295 (1978).

⁹ K. F. Liu, C. W. Wong, Phys. Rev. D 21, p1350 (1980).

¹⁰ M. Gell-Mann, Phys. Lett. 8, p214 (1964).

¹¹ G. Zweig, CERN report 8182/th401; 8419/th412 (1964) (unpublished).

¹² R. J. Jaffe, Phys. Rev. D 15, p267 (1977).

¹³ C. Defoix, et al., Nuc. Phys. B44, p125 (1972).

J. B. Gay, Phys. Lett. 63B, p220 (1976).

¹⁴ This is not Jaffe's argument, which is based on the masses of the $J^{PC} = 0^{++}$ nonet of mesons. This presentation is more direct, but the coupling of the $\delta(980)$ to $K\bar{K}$ is subject to some controversy. See for example:

H. J. Lipkin, Preprint ANL-HEP-PR-81-23 (1981).

De Rujula and Jaffe¹⁵ in 1977.

Lipkin et al.⁸ have suggested that the X(2.83) could be such a four quark state. If this were true, it could be mixed to a large extent with lighter quarks since the mass of a pure $D\bar{D}$ state is expected to be roughly 3.6 GeV. Such a particle, with a large coupling to light quarks, would be produced with comparatively large cross sections in hadronic collisions. Afek et al.⁸ have suggested that it could have a large partial decay width into two photons.

1.3 Current Status of Pseudoscalar States of Charmonium

Figure 2 shows a more recent view of the charmonium system, as modified by the Crystal Ball and MARK II groups at SPEAR. The two earlier candidates for the pseudoscalar states have been eliminated¹⁶, and two new candidates have been added¹⁷. Both the masses and the transition rates of these new candidates fall neatly in line with the theoretical expectations of the charmonium model. The Russian observation of the X(2.83) in the reaction:

$$\pi^- P \longrightarrow \gamma \gamma N$$

has not been confirmed, and the two photon decay mode of the new η_c candidate has not been observed in pion nucleon collisions or in the radiative decays of the J/ψ or the ψ' .

¹⁵ A. De Rujula, R. L. Jaffe, Proc. of 5th Int. Conf. on Experimental Meson Spectroscopy (1977), edited by E. Von Goeler and R. Weinstein (Northeastern Univ. Press, Boston, 1977) p83.

¹⁶ R. Partridge, et al., Phys. Rev. Lett. 44, p712 (1980).
E. Bloom, Proc. Int. Symp. on Lepton Photon Interactions (1979), edited by T. Kirk and H. Abarbanel (FNAL, Batavia, Illinois) p92.

¹⁷ T. M. Himel, Phys. Rev. Lett. 45, p1142 (1980).
R. Partridge, Phys. Rev. Lett. 45, p1150 (1980).
D. Scharre, 1981 International Symposium on Lepton and Photon Interactions at High Energies, Bonn, August 24-29, 1981. (to be published).

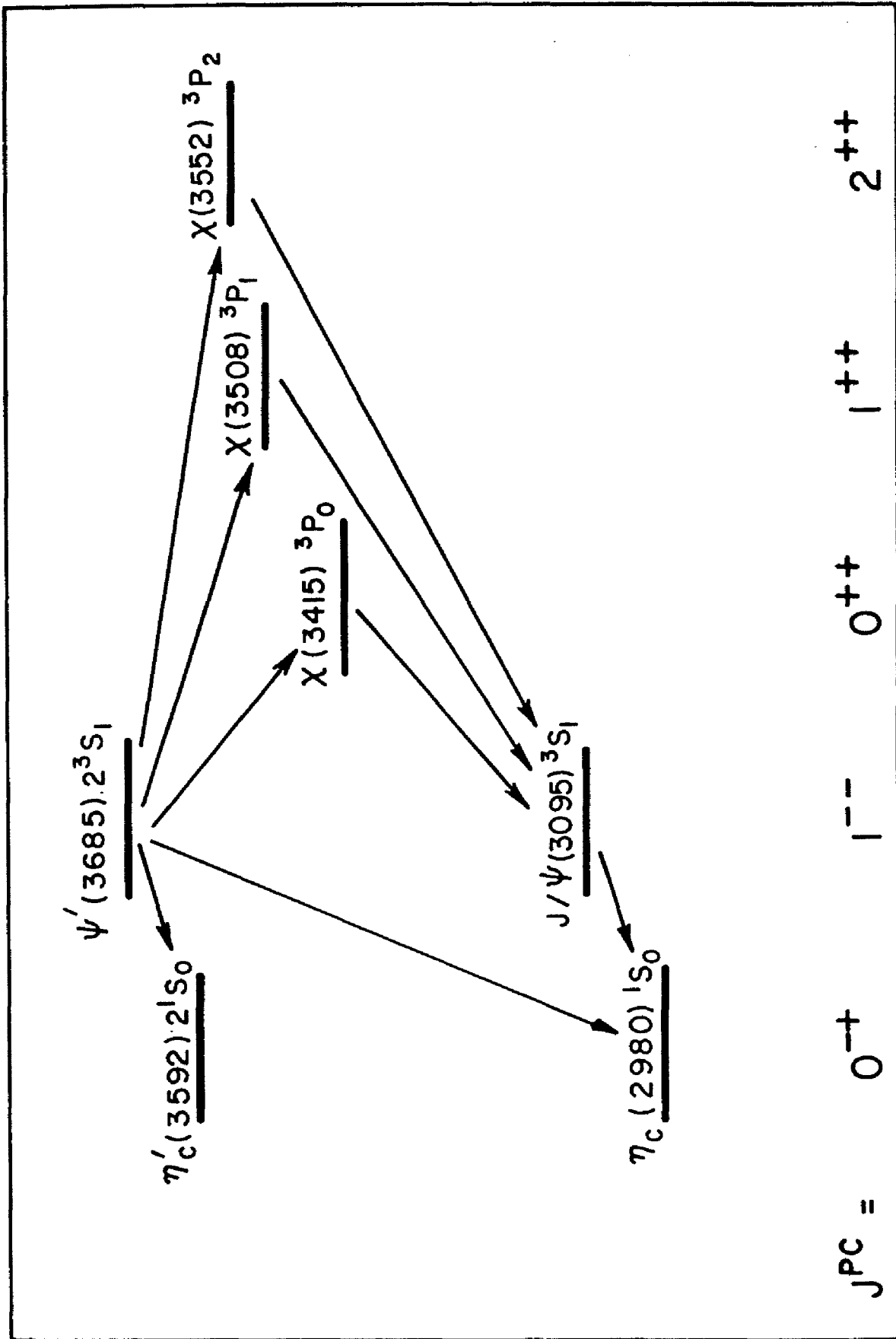


Figure 2 Current Low Mass Charmonium States and Their Radiative Transitions

1.4 The Goals of This Experiment

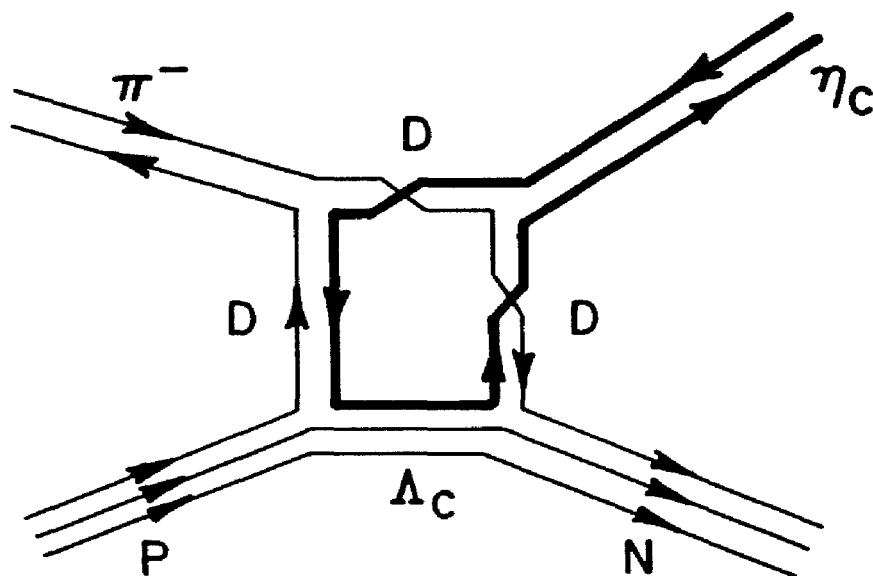
The 3 GeV mass region is known to contain a large number of states, and if the four quark model of Jaffe or the quark anti-quark gluon model of Horn and Mandula¹⁸ is correct, there could be quite a few more states in this region, many of which may be difficult to observe in $e^+ e^-$ storage rings. This thesis will present the results of an experiment carried out at Brookhaven National Laboratory in an attempt to clarify this situation. Many of these states may be produced in hadronic collisions with large enough cross sections to be seen. The Russian results may in fact be correct, and there may be more states to find. In addition to the two photon spectra, such an experiment is sensitive to a large number of other final states, decaying to: $\pi^0 \gamma$, $\pi^0 \pi^0$, $\eta \gamma$, $\eta \pi^0$, $\eta \eta$, and $e^+ e^-$.

There are several factors that made the choice of a 13 GeV/c beam momenta seem warranted. Of greatest importance was the fact that well above threshold the cross section for the exclusive production of almost any particle rises with decreasing beam energy. This behavior is simply explained, since the number of channels increases with increasing beam energy while the total cross section remains roughly constant. In addition, there is a possibility that near the kinematic threshold the cross section may be enhanced by alternate production mechanisms. Such a possibility is considered by Berger and Sorensen¹⁹, who describe the possible effects of a baryon-meson resonance in the s-channel, as is shown in Figure 3. There is, however, one disadvantage to using such a low beam energy. It will be shown that the background levels rise significantly with decreasing beam energy.

¹⁸ D. Horn, J. Mandula, Phys. Rev. D 17, p898 (1978).

¹⁹ E. L. Berger, C. Sorensen, Phys. Lett. 62B, p303 (1976).

POSSIBLE THRESHOLD ENHANCEMENT
MECHANISM



$$\sqrt{s} = M(\Lambda_c) + M(D)$$

$$\approx 10-12 \text{ GeV}/c^2$$

Figure 3 Possible Five Quark Threshold Enhancement Mechanism

1.5 Hadronic Production of η_c

Most estimates of exclusive η_c production cross sections in pion nucleon scattering are rather similar. The basic production mechanism is expected to be the same as in the exclusive production of η_s , as is shown in Figure 4, with a suppression term²⁰ arising from the small coupling of the η_c to light quarks.

There are several different methods used to estimate the suppression factor, or the coupling of the η to the η_c . Recently Fritzsche and Jackson²¹ have estimated the amount of mixing of light quarks into the η_c wavefunctions and have shown that their values are consistent with those deduced from the radiative decay widths of the J/ψ . These results support a quark wavefunction for the η_c of:

$$|\eta_c\rangle = |c\bar{c}\rangle + .01*|\eta\rangle + .022*|\eta'\rangle$$

This mixing can not only affect the hadronic decay width of the η_c and the J/ψ , but can also cause the mass of the η_c to be lower²² by a few hundred MeV than that expected for a pure $c\bar{c}$ state. The amount of mixing required to produce a mass of 2.83 GeV, however, is much more than that estimated by Fritzsche and Jackson²¹.

1.6 Expected Yield of η_c in Pion Nucleon Collisions

To obtain a numerical value for the production cross section of the η_c it is necessary to multiply the η or η' cross section by the suppression factor of Fritzsche and Jackson²¹ and then correct for the limited amount of phase space available near the kinematic threshold. For example, if one scales from the η' production cross section, the η_c production cross section is:

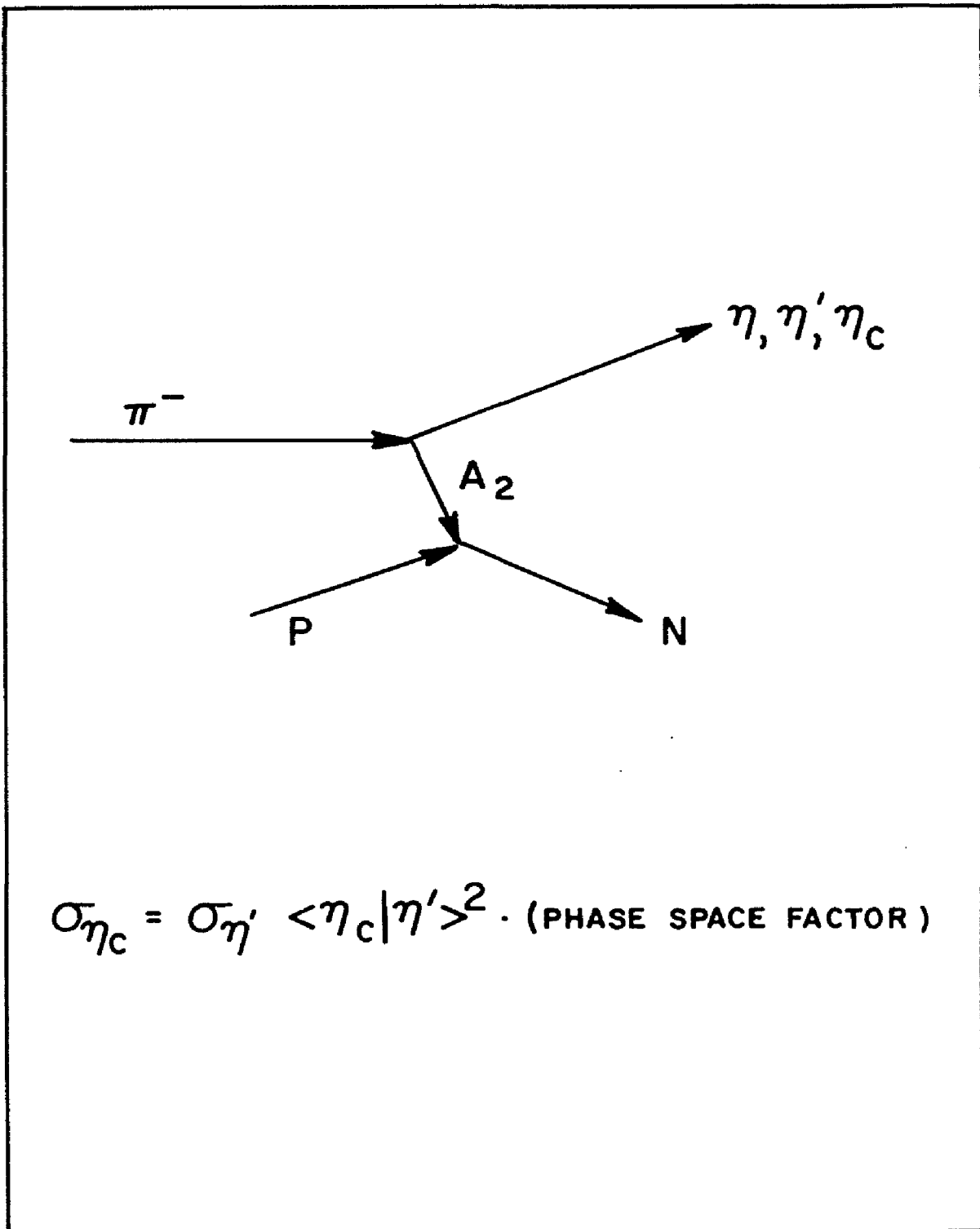


Figure 4 η_c Production Mechanism in Hadronic Collisions

$$\begin{aligned}\sigma_{\eta_c} &= \sigma_{\eta'} \langle \eta_c | \eta' \rangle^2 \text{ (phase space factor)} \\ &= [\sigma_{\eta'} \langle \eta_c | \eta' \rangle^2] R\end{aligned}$$

where:

$$R = 1/\sigma_{\eta'} \int_{t_{\min}}^{t_{\max}} d\sigma/dt dt$$

I have divided the above expression into two factors, one related to the amplitude for the process and one to the available phase space. To estimate the phase space factor it is necessary to know the dependence of the production cross section on "t", the momentum transfer to the nucleus. On the basis of the results of Apell et al.⁶, I choose several t-distributions similar to the η and η' results²³ and display the phase space suppression factors in Table 1. The phase space correction to the cross section is roughly a factor of one-half at masses near the $X(2.83)$ or the η_c , but for masses near the η_c' the cross section is reduced by an order of magnitude.

The branching ratio of the η_c to two photons is, comparatively speaking, on much firmer ground than the hadronic production cross section. The two photon width is calculated using QED, and the hadronic width is calculated from QCD. The result, to first order, for the branching ratio is:

$$\frac{\Gamma(\eta_c \rightarrow \gamma\gamma)}{\Gamma(\eta_c \rightarrow \text{all})} = \frac{9Q^4\alpha^2}{2\alpha_s^2}$$

where: Q = charge of charmed quark = 2/3
 α_s = strong coupling constant $\approx .2$ to $.3$

$$\text{B.R.} \approx .5 \times 10^{-3} \text{ to } 1 \times 10^{-3}$$

This value is sensitive to the number of gluons, currently believed to be eight, and to the strong coupling constant, which is constrained by numerous other reaction data. The higher order corrections to the branching ratio are much more difficult to calculate. The expected two photon signal observed by our experiment, on the basis of the first order QCD calculation of the branching ratio, is between .5 and 2 pb. If, however, the large mixing predicted by Harari²² is correct, the cross section could be several orders of magnitude larger.

For comparative purposes it is useful to estimate the magnitude of the two photon signal expected from the production of an ordinary light quark resonance. A typical meson might have a total width of 200 MeV and be produced with a 10 μ b cross section. Furthermore, its partial decay width into two photons might be as large as 10 KeV. Such a particle would be seen as a 500 pb signal in the two photon channel.

Mass	$d\sigma/dt=(1-38t)e^{9.1t}$	$d\sigma/dt=(1-31t)e^{7.5t}$
2830 MeV	.55	.63
2980 MeV	.42	.51
3454 MeV	.06	.13

²⁰ C. Quigg, R. Field, Fermilab Report 75/15 THY (1975) (unpublished).

²¹ H. Fritzsch, J. D. Jackson, Phys. Lett. 66B, p365 (1977).

²² H. Harari, Phys. Lett. 60B, p172 (1976).

²³ N. R. Stanton, et al., Preprint C00-1545-266, (1979).

Chapter II THE APPARATUS

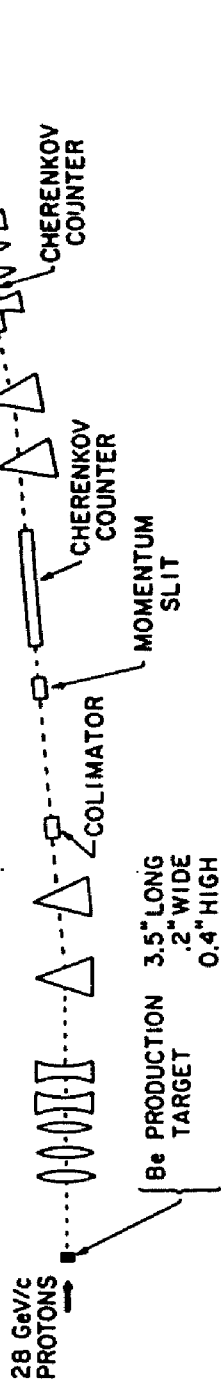
The experiment was conducted in an unseparated secondary hadron beam generated by the A.G.S. (Alternating Gradient Synchrotron) at Brookhaven National Laboratory. The transport system for this beam line, the B1 beam line, is shown in Figure 5. The 28 GeV/c protons from the accelerator were directed to a 3.5 inch long Be target. Secondary particles produced by this interaction were collected by a set of quadrupole magnets, momentum analyzed by two sets of dipole magnets and a collimator, and then focused onto our target by another set of quadrupole magnets. The beam delivered to our target had a spot diameter of roughly 1/2 inch. Under typical running conditions the momentum spread of the beam was limited to $\pm 1/2\%$.

The beam was delivered in spills of one second duration once every 2.4 seconds. Its intensity during the spill was periodic on two widely separate time scales. The lowest modulation frequency was approximately 360 Hz, caused by AC ripple from AGS magnet power supplies. The other modulation period was approximately 180 ns, which was the synchrotron RF period. Because the RF power was turned off and the beam "de-bunched" before the spill, the beam should have had no short-term structure. In practice, however, there was always a small amount of modulation, which varied from one part of the spill to another. For most of the running period the duty factor²⁴ was around 70%.

²⁴ The duty factor is simply the ratio of the average beam intensity to the instantaneous intensity observed at the time of a typical beam interaction. It is therefore a measure of the effective beam intensity.

²⁵ G. M. Bunce, BNL Report 50874 (1974).

B1 BEAM LINE



PLAN VIEW SCALE: $\frac{20 \text{ Feet}}{1}$

Figure 5 Secondary Beam Layout

Pions comprise almost 99% of the beam²⁵, while kaons, anti-protons, and electrons comprise between .1 and 1% of the beam. Two Cherenkov counters were positioned in the beam line. These were not used for the data taking period but were used during special calibration runs to identify electrons.

2.1 General Layout of Experiment

The basic experimental layout is shown in Figure 6. Two large photon detectors with an active area of 1.05 x 2.1 meters were placed at a 16.4 degree angle to the beam line, approximately 6 meters downstream of the target. The goal was to detect all events in which the final state was composed of all neutral particles, all of which deposited their energy in the two large photon detectors. The remaining solid angle not covered by the photon detectors was instrumented with anti-coincidence counters.

The main source of background in this experiment was from $\pi^0 \pi^0$ events in which both π^0 s were misidentified as γ s. There are three common mechanisms by which this could occur. First, the π^0 could decay with minimum opening angle, resulting in two photons that were too close to each other in the detector to distinguish as two photons. The photon detectors were designed to minimize this occurrence. Second, one medium-energy photon from a π^0 may escape detection, possibly by passing through the hole in the photon vetoes left for the noninteracting beam. Third, the π^0 may decay very asymmetrically, resulting in one high-energy photon hitting the detector and an undetected very low-energy photon. Both the veto counters and the photon detectors were used to detect these low-energy photons. This section will describe the event selection cuts that were used to identify events with these low-energy photons.

The arrival of a beam particle was sensed by three scintillation counters, labeled B0, B1, and B2 in Figure 6, that were located

PLAN VIEW OF EXPERIMENT

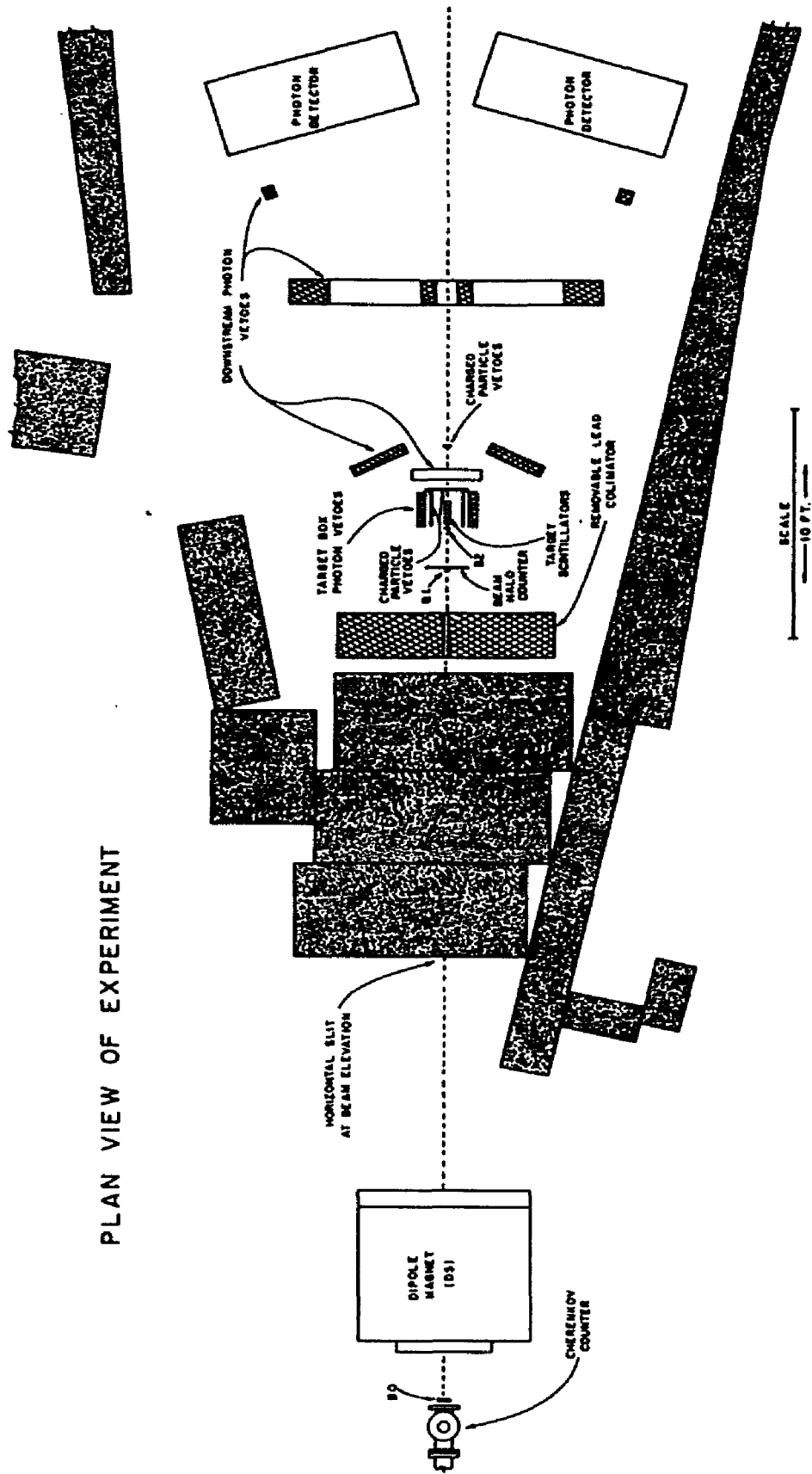


Figure 6 Plan View of Experiment

upstream of the target. The downstream beam counter had a 1.125 inch diameter and was placed approximately 1 inch in front of the 1.25 inch diameter target. In addition, the beam was surrounded by a scintillation counter that was used to veto beam particles arriving in coincidence with a halo particle. An exploded view of the target region is shown in Figure 7.

2.1.1 The Target

The target, which was 12 inches in length, or roughly $1/3$ of a pion interaction length, was composed of plastic scintillator and was divided into six segments of equal length. This segmentation allowed the beam particle to be tracked from where it entered the target to the point where it interacted. No target counters downstream of the interaction should have been hit, since there were no charged particles in the final state. In this manner the location of the interaction was determined with a precision of about 2 inches, which corresponded to an error of about 1% in the opening angle of the photons, and hence in the reconstructed mass.

2.1.2 Charged Particle Vetoes

All reactions with which this thesis is concerned have an all neutral final state. To enforce this requirement the entire target was surrounded by scintillation counters. These counters are labeled "charged particle vetoes" in Figures 6 and 7. The signals from these counters vetoed approximately 99.9% of the incoming beam particles, approximately $1/3$ of which interacted in the target. This is roughly in agreement with the known neutral final state cross section at 13 GeV/c.

The charged particle veto counters presented one of the most significant rate limitations for the experiment. Even with the use of state of the art electronics, the time resolution of the veto decision could not be reduced to less than 10 ns. Since every beam particle hit one or more of these counters, it is clear that for beam

EXPLODED VIEW OF TARGET REGION

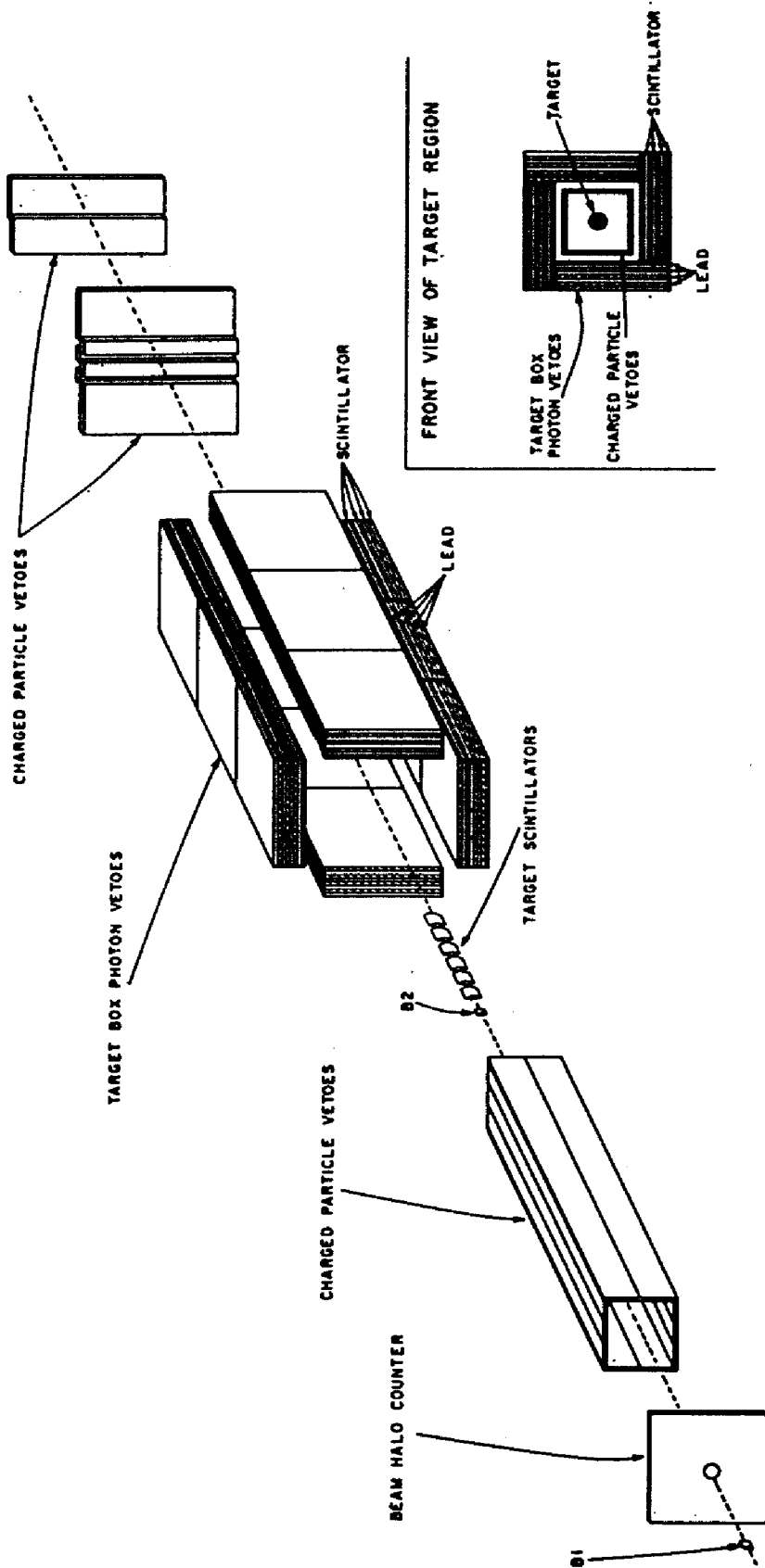


Figure 7 Exploded View of Target Region

intensities in excess of 10 MHz the probability of accidental vetoing exceeded 10%.

2.1.3 Photon Veto Counters

A set of lead scintillator sandwich shower counters surrounded the target. These counters, which are labeled "target box photon vetoes" in Figures 6 and 7, were primarily used to ensure that a neutron²⁶ rather than an excited baryon state was produced in the reaction. To some extent these counters also helped veto photons resulting from the asymmetric decay of π^0 's.

The primary defense against low-energy photons from π^0 decays was the wall of veto counters placed approximately 3 meters downstream of the target. These are labeled "downstream photon vetoes" in Figures 6 and 7. The structure of a typical counter is shown in Figure 8. Most of these counters had more than one phototube, all of which viewed the same scintillation counters.

Figure 9 shows the downstream photon vetoes viewed looking downstream from the target. Roughly 99% of the solid angle was covered by either the detector or by the two sets of photon veto counters. To reduce the accidental rate in the main detector, non-interacting beam particles were allowed to escape through a small hole without striking the veto counters. The veto counters were very important for the reduction of background, as will be described below.

2.1.4 Photon Detector Arms

Each detector arm had a structure as shown in Figure 10. The design of the detector was influenced by the availability of a large number of lead glass blocks from a previous²⁷ Brookhaven experiment, as well as by the need to distinguish between a single photon and two photons from π^0 decay, in which the distance between two photons could

²⁶ A small fraction of the neutrons were detected by these veto counters, as is discussed in Section 5.1.4.

²⁷ A. S. Carroll, et al., Nuc. Inst. and Methods 179, p229 (1981).

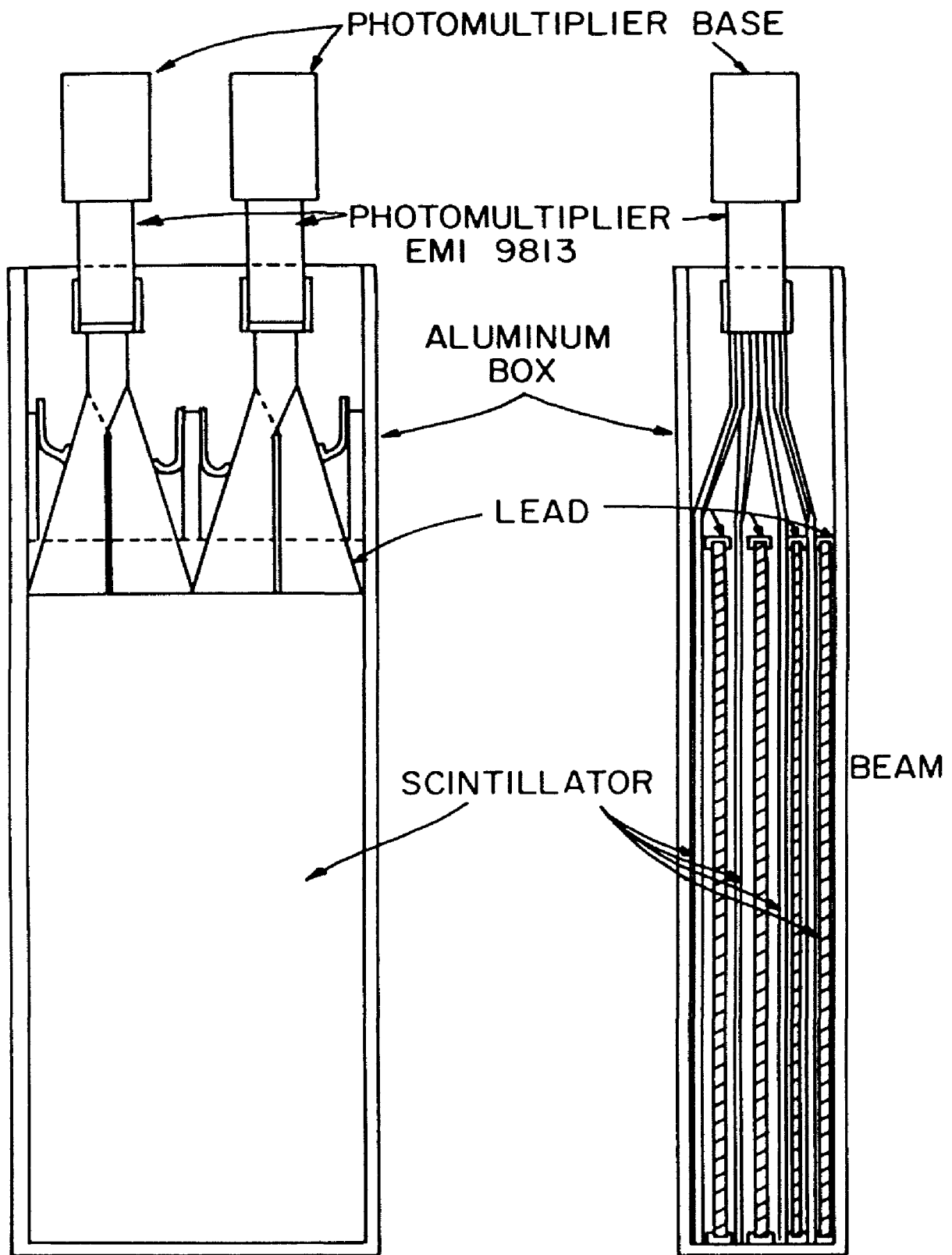


Figure 8 Typical Photon Veto Layout

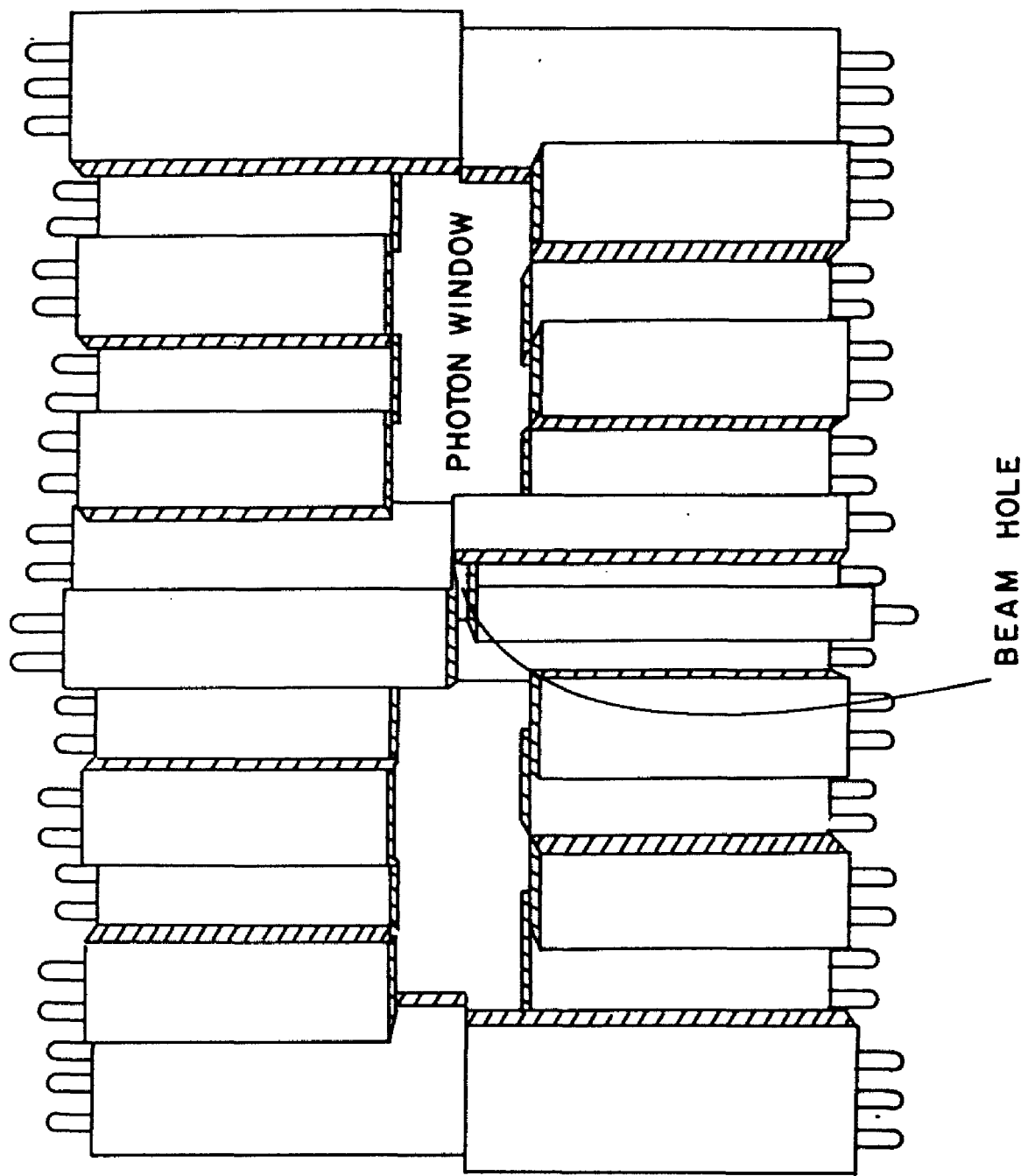


Figure 9 View of Downstream Photon Vetoes from Target

be as small as 6 inches. Because of the latter requirement, good position information from the detector was essential.

Each detector arm was composed of four layers. Two layers were lead glass and two were lead scintillator sandwich. The photons emerging from the target first encountered a 4.5 radiation length lead-scintillator sandwich converter section, which is labeled "calorimeter" in Figure 10. Figure 11 is a side view showing the two layers of calorimeter counters, each of which was 1 meter long, 6 inches wide, and 1/4 inch thick. The light from the two calorimeter counters in each section was optically added and viewed by a single phototube.

The detector element that gave the most detailed position information was the scintillator hodoscope. This was placed directly behind the converter section. The thickness of the converter section was chosen such that in roughly 94% of the cases where both photons from a π^0 decay struck a detector arm both photons would convert before the hodoscope plane, forming two distinguishable showers. Each hodoscope counter was 42 inches long, 1 inch wide, and 1/4 inch thick. These were combined to form a 42x42 square hodoscope. Each arm had two of these hodoscopes placed side by side to fill the entire active area. The x-y position of an electromagnetic shower could be determined with an accuracy of better than 1/4 inch by the hodoscope.

The primary device used to measure the energy of the photon was the lead glass, which was divided into two sections labeled "front lead glass wall" and "rear lead glass wall" in Figure 10. The rear lead glass wall was formed of 15x15x25 cm lead glass blocks stacked as shown in Figure 10 forming a 7x16 matrix 9.3 radiation lengths in thickness. Because a typical electromagnetic shower hit several of these blocks, the position of the shower could be measured with a precision often better than one inch. This resolution was determined by comparing the position measured in the rear lead glass wall with that measured in the hodoscope.

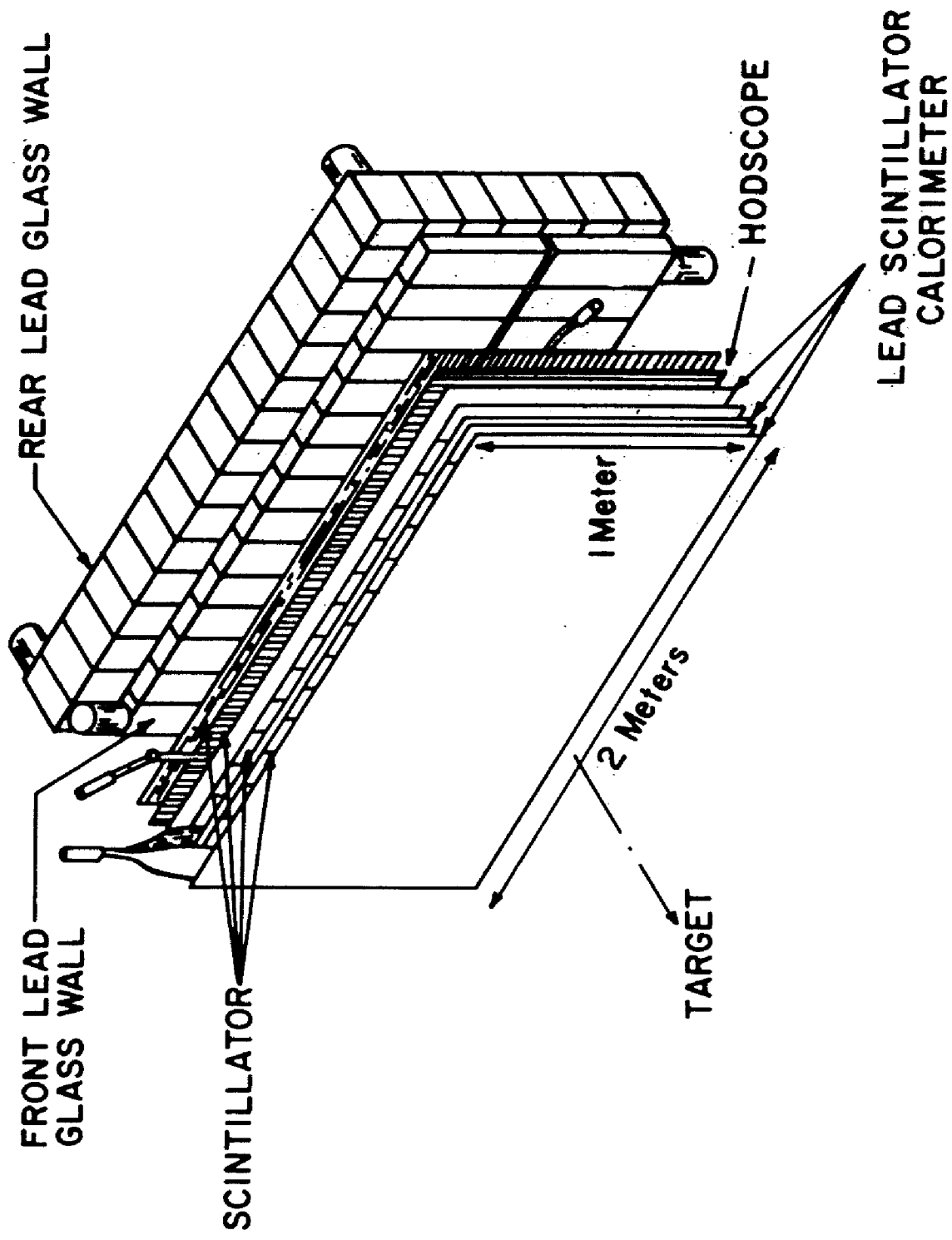


Figure 10 Layout of Photon Detector Arm

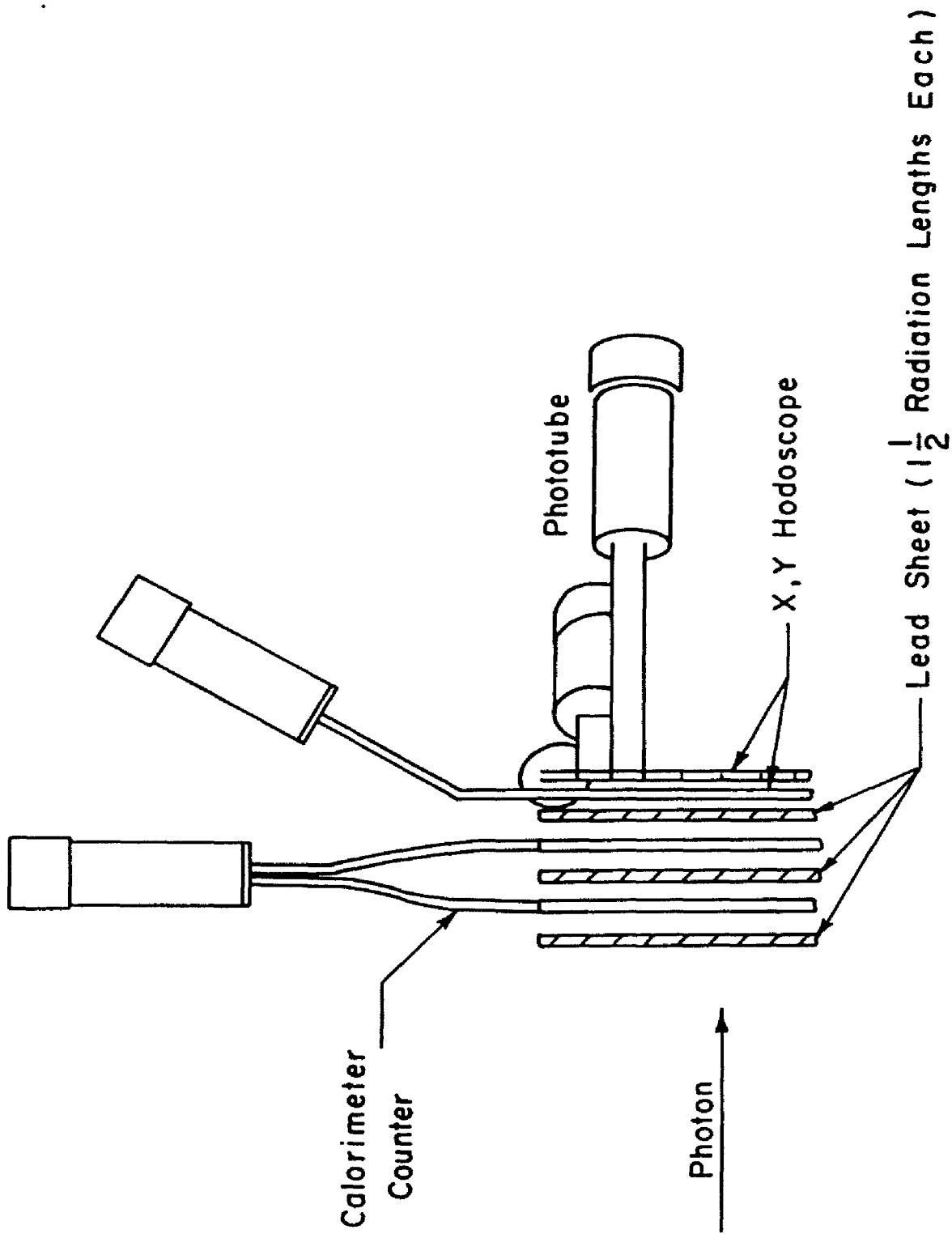


Figure 11 Converter Section Side View

The front lead glass wall, which was 2.8 radiation lengths in thickness, was formed of 7.5x15x45 cm lead glass blocks as shown in Figure 10. This was placed a few inches in front of the rear lead glass wall. Both lead glass layers were enclosed in a light-tight air-conditioned house.

The energies from all four layers were added to determine the photon energy. Section 4.2 describes how the weighting factors for the four detector layers were determined. A Monte Carlo simulation program (by K. McDonald) was used to estimate the energy resolution expected for a detector in this configuration. Although 80% of the energy of a typical photon was deposited in the lead glass, which should have an energy resolution of better than $6\%/\sqrt{E}$, where E is measured in GeV, the 4.5 radiation length converter section reduced the energy resolution to about $11\%/\sqrt{E}$. The overall fractional energy resolution actually obtained was approximately $14\%/\sqrt{E}$, as will be described in Section 4.2.

2.2 Main Trigger Logic

A block diagram of the trigger logic is shown in Figure 12. The trigger simply required that a beam particle enter the target, no charged or neutral particles be detected in the veto counters, and a substantial fraction of the beam energy be deposited in the detector. Only about ten events met these conditions in each spill, and almost all of these were consistent with being $\pi^0 \pi^0$ events.

The beam and veto counter logic was formed using high-speed NIM logic. One of the beam counters was used to define the interaction time. The accidental vetoing caused by the trigger logic was simulated and monitored by delaying the beam signals by one RF period and then subjecting them to the same veto signals as used in the trigger logic, as is shown in Figure 12. Typically 10-15% of the beam particles were lost due to accidental vetoing by the hardware trigger. This result is used in Chapter 5 to normalize the cross sections.

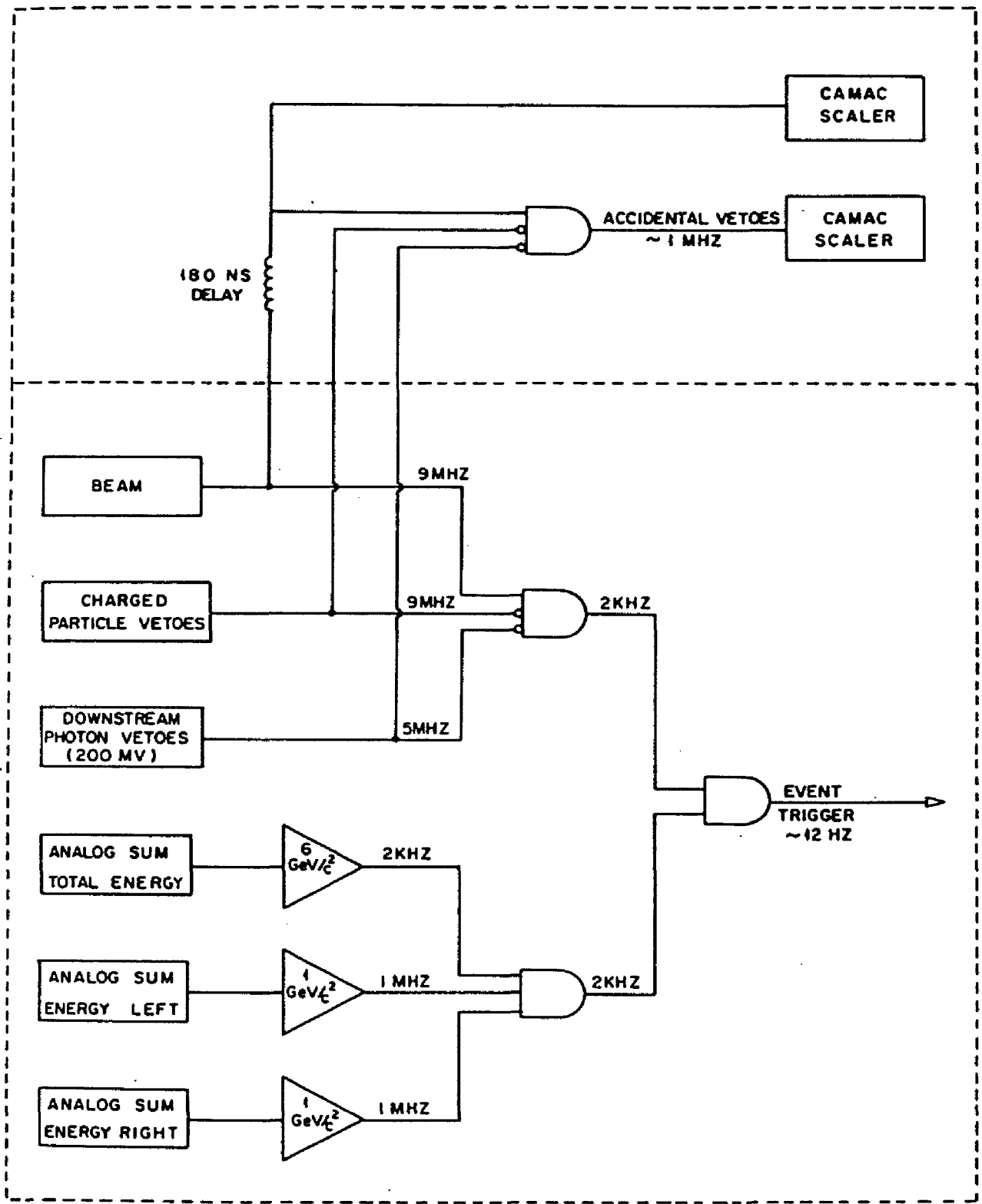


Figure 12 Trigger Logic Block Diagram

The energy requirement was formed using the weighted analog sum of the pulse heights in all four detector layers. These were fed into burst guard²⁸ type discriminators, whose outputs formed a 60 ns wide window that was required to bracket the beam pulse to trigger an event. This type of discriminator was necessary to minimize dead time in the trigger logic. At least 1 GeV of energy was required to be deposited on each arm, and the total energy had to exceed about 7 GeV.

2.3 Instrumentation

A recurring theme throughout this thesis is the need to detect very low-energy photons in a very high rate environment. This need is illustrated by the fact that roughly 2% of the photons produced by the decay of a 5 GeV π^0 will have an energy of less than 50 MeV. In order to reduce the background from the $\pi^0 \pi^0$ events to the 10^{-3} level, we needed to detect the majority of such photons in the presence of a background of 5 GeV hadronic showers with rates of several MHz.

The instrumentation for the detector elements had to satisfy two conflicting requirements. We needed both a precision measurement of the energy deposited in each detector element, often several GeV, while still maintaining good detection efficiency for low-energy photons. The maximum pulse size from each detector element was chosen to give a full scale reading on the charge integrating ADCs (analog to digital converters). Since the phototube signals from some of the detector elements were quite long, the resultant pulse heights produced by low-energy photons were quite small. Table 2 shows the typical signal size that a 50 MeV photon was expected to have produced in each of the various counter types. The vulnerable time period, during which confusion was possible with a pulse caused by another beam particle, is also shown in the table. To accomplish our goal of reducing the background to the 2% level without extreme losses in

²⁸ Burst guard discriminators respond normally to short pulses, but for pulses longer than the output width the output remains on until the input level passes below threshold.

efficiency every detector element in the experiment was instrumented with an ADC, a TDC (time to digital converter), and a latch, all capable of responding to a 50 MeV equivalent signal. The ADC measured the energy deposited in each detector element. The TDC and latch were needed to correlate the deposited energy with the proper beam interaction, since the rates were up to several MHz in many detector elements. Because of the small signal size, some of the detector elements required special instrumentation, which will be described below.

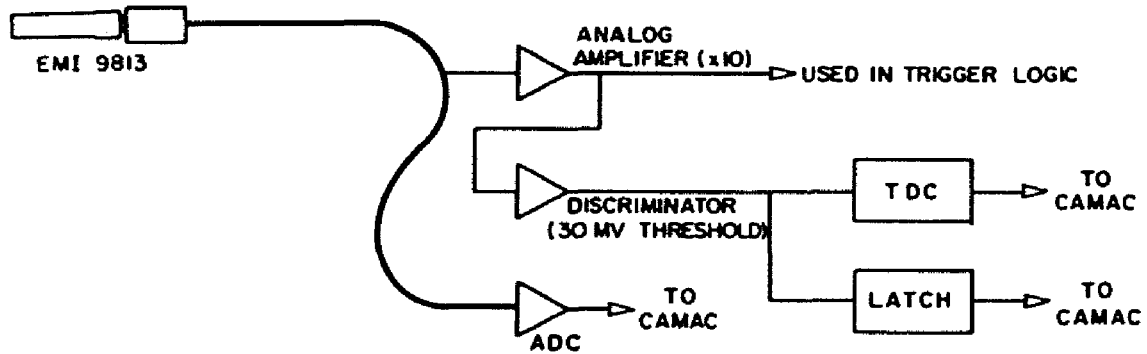
TABLE 2
Approximate Signal Size for 50 MeV Photons

	Signal size	Vulnerable time
Photon vetoes	50 mV	10 ns
Calorimeters	4 mV	20 ns
Hodoscope	3 mV	40 ns
Lead glass	.5 mV	150 ns

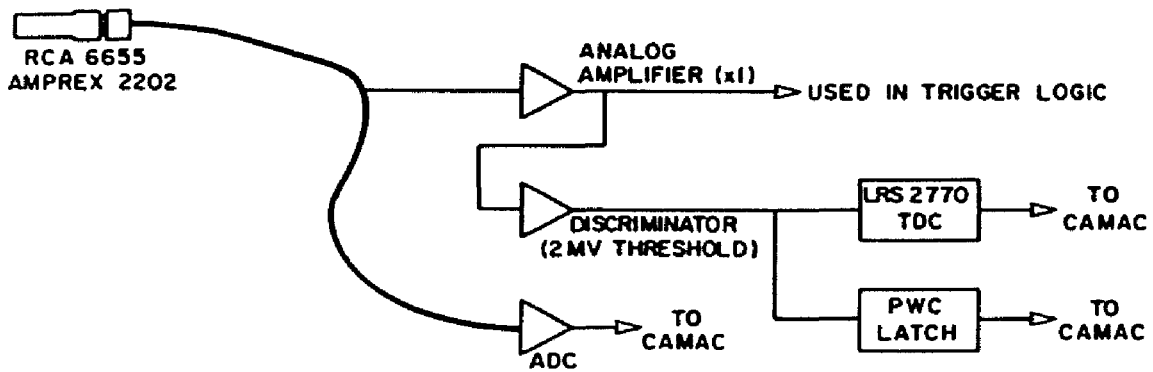
2.3.1 Calorimeter Counter Instrumentation

A block diagram of the calorimeter counter instrumentation is shown in Figure 13. The signals were fed past a special amplifier, the circuit of which is shown in Figure 14. This analog amplifier, as did the others shown in Figure 13, had a high input impedance, which allowed most of the signal to be collected by the ADC. In addition, the analog sum of all the input signals was formed and used in the trigger logic. The individual channel outputs, which were amplified by a factor of 10, were fed into a discriminator that fed a CAMAC latch and TDC. This discriminator threshold was set to 30 mV, allowing the detection of minimum ionizing particles passing through one of the two layers of calorimeter counters.

CALORIMETER INSTRUMENTATION



HODOSCOPE INSTRUMENTATION



LEAD GLASS INSTRUMENTATION

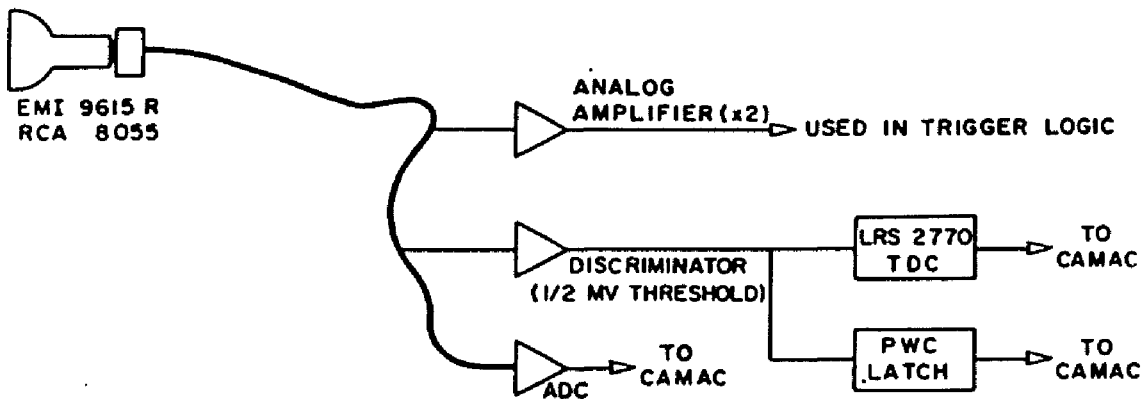


Figure 13 Detector Instrumentation Block Diagrams

2.3.2 Hodoscope Instrumentation

A block diagram showing the instrumentation of a typical hodoscope counter is shown in Figure 13. The phototube signals were fed past an amplifier used to generate both an amplified analog output signal and a discriminated logic output signal. The discriminator thresholds were set at about 2 mV, which corresponded to roughly 5 ADC counts or about 2/3 the signal size expected for a minimum ionizing particle. In addition, the analog sum of all 25 amplifier channels in a box was formed. The circuit diagram of this amplifier is shown in Figure 15. The outputs of the discriminators were sent to an LRS (Lecroy Research Systems) model 2770 drift chamber TDC system and to a PWC (proportional wire chamber) latch system, on loan from the CERN-Heidelberg collaboration²⁹. The PWC latch system was read out serially using a PWC scanner³⁰ module.

2.3.3 Lead Glass Instrumentation

Figure 13 shows a block diagram of the instrumentation used for a typical lead glass counter. The 5-inch phototubes used on these counters had a rise time of approximately 40 ns. The signals from the phototubes first passed an amplifier, whose circuit diagram is shown in Figure 16. The outputs of these amplifiers were added using LRS 428F linear fan-in fan-out modules and were used in the trigger logic.

The lead glass signals were next sent past a low level discriminator. The circuit diagram of this device, which is shown in Figure 17, is similar to that of a drift chamber pre-amplifier designed for a recent FNAL³¹ experiment. The discriminator threshold

²⁹ P. Schilly, et al., Nuc. Inst. and Methods 91, p221 (1971).

H. Cunitz, W. Sippach, J. Dieperink, Nuc. Inst. and Methods 91, p211 (1971).

³⁰ T. A. Nunamaker, Nuc. Inst. and Methods 106, p557 (1973).

³¹ G. Gollin, et al., IEEE Trans. Nuc. Sci. Vol. NS-26, No. 1, p59 (1979).

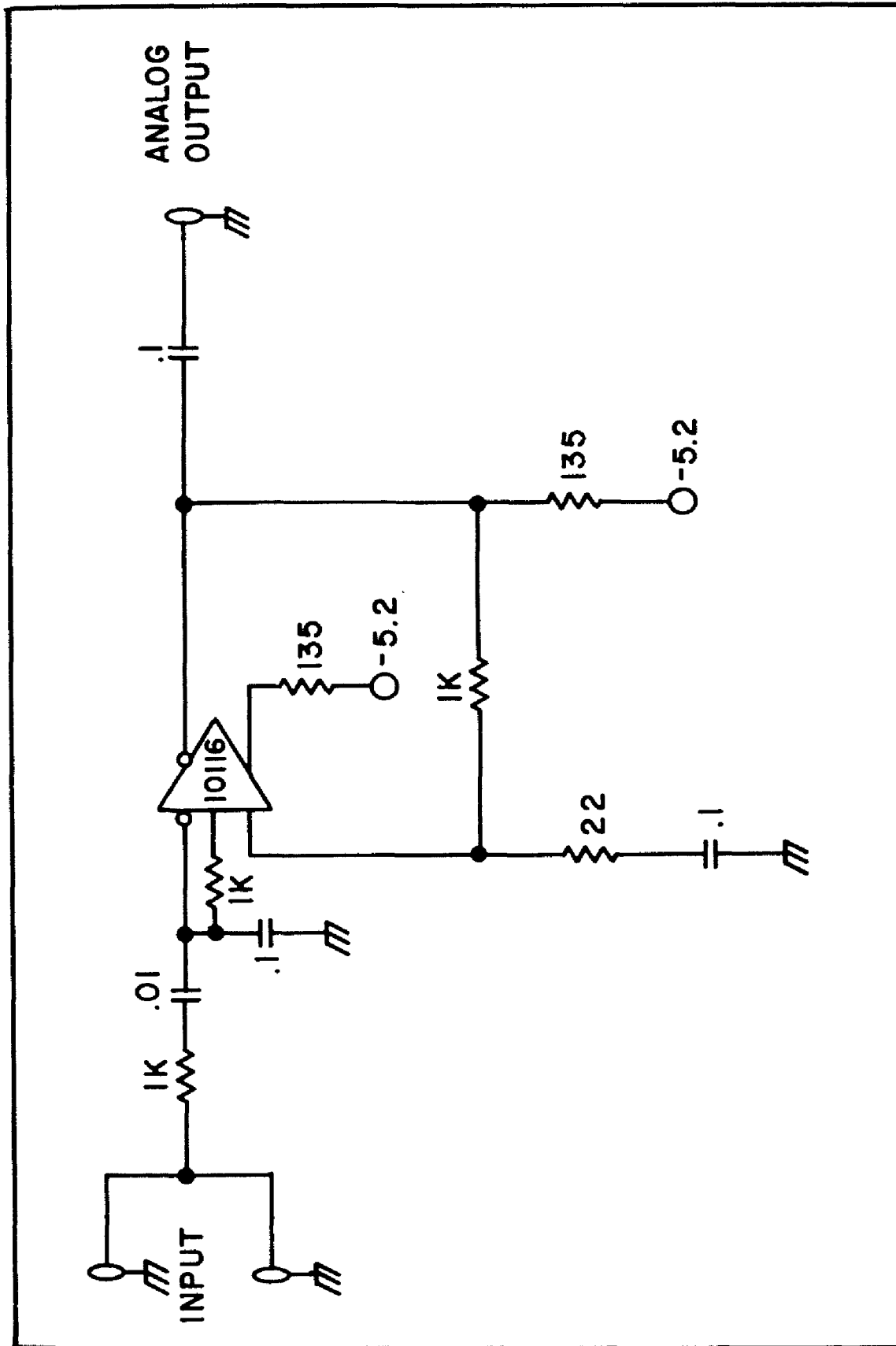


Figure 16 Analog Amplifier Used on Lead Glass Counters

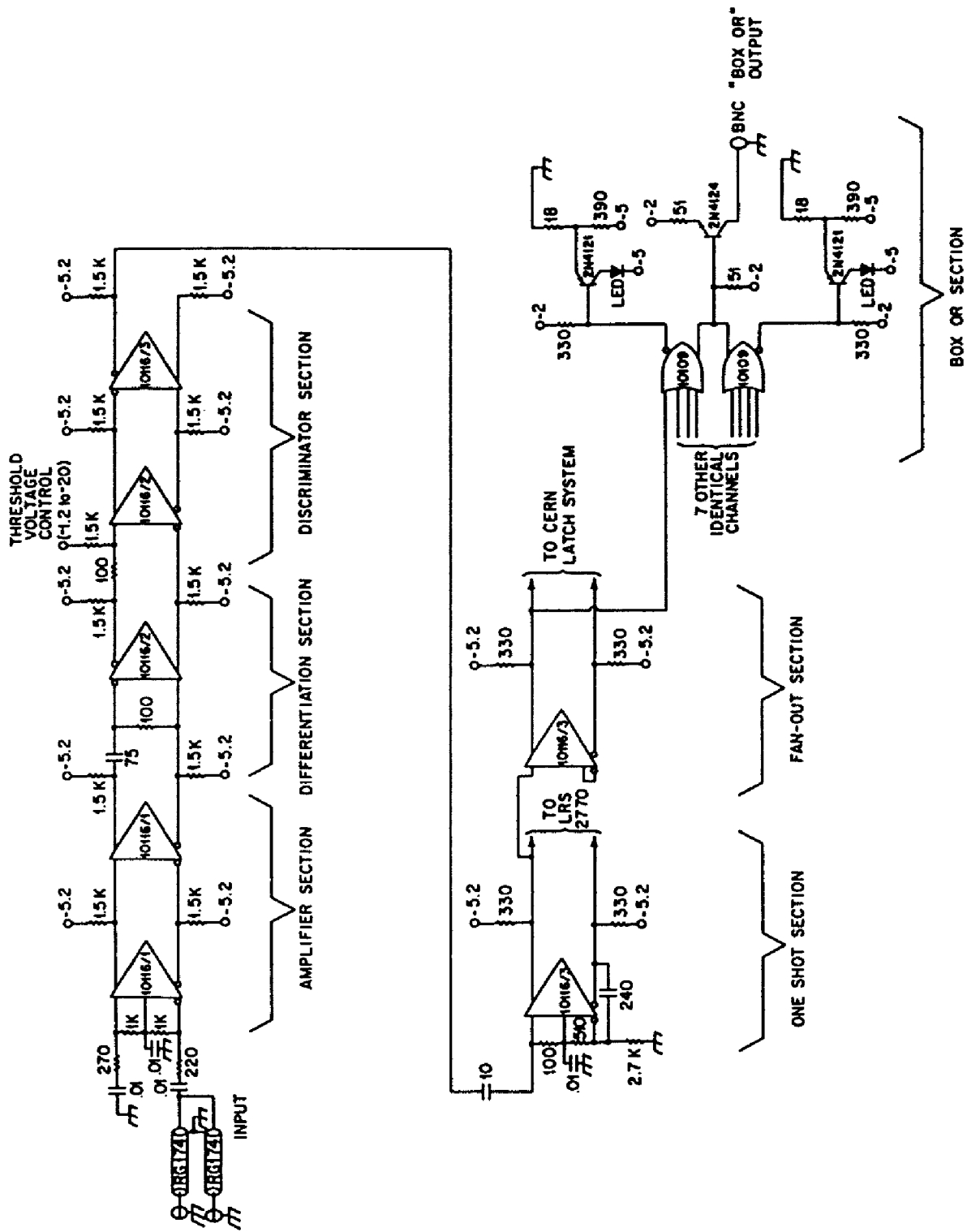


Figure 17 Low Level Discriminator Used on Lead Glass Counters

was set at about 1/2 mV, which corresponded to about 4 ADC counts, or about 40 MeV of deposited energy. The outputs of the discriminators were sent to the same latch and TDC system used for the hodoscope counters.

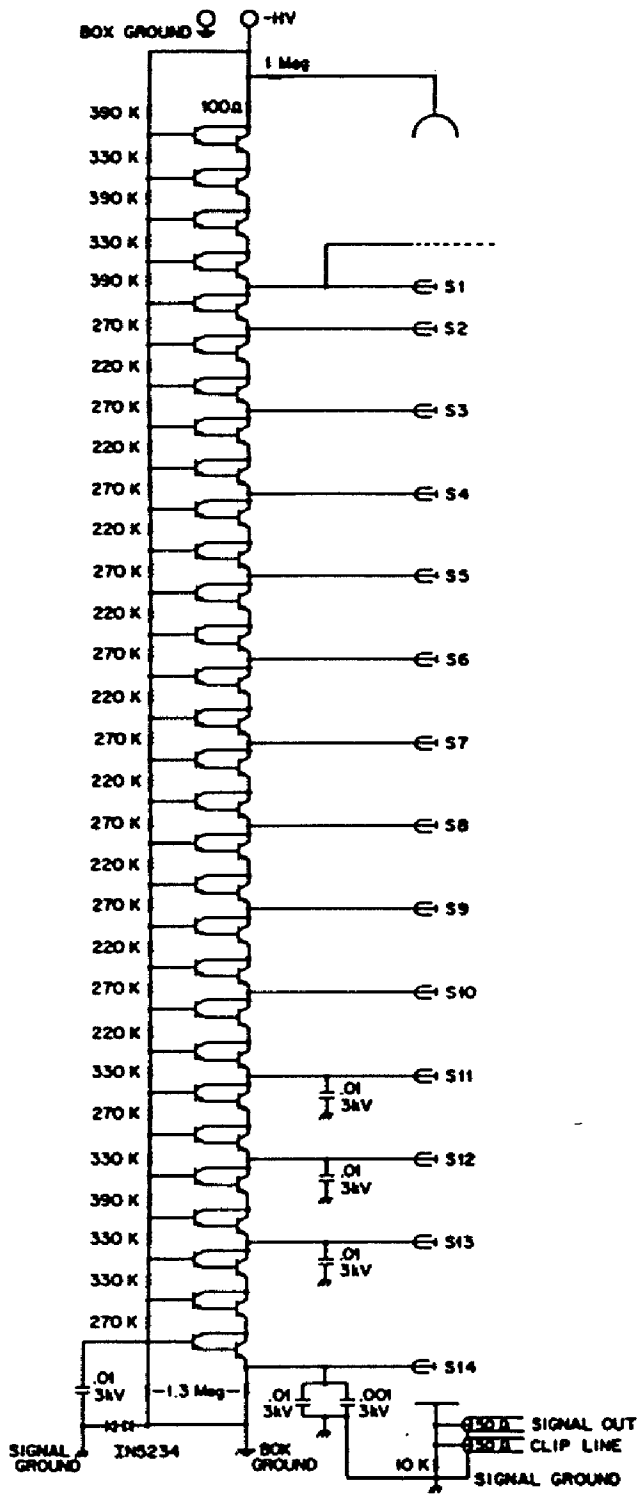
In designing the discriminators we took advantage of the fact that extremely high circuit density was not required. The individual channels were widely separated on the circuit boards, and the input signals were brought in on 50 ohm coaxial cable. Small LED (light emitting diode) indicators were mounted on the front panel to warn of any oscillating channels. No oscillations were ever observed in any of the channels, but the LEDs did prove very useful for detecting channels having RG 8 connectors with improper contacts, which caused excessive noise to be picked up by the pre-amp. Cross-talk between channels was shown to be essentially nonexistent.

2.3.4 Transistor Phototube Base

Although a large number of low-energy photons struck the detector, the majority hit the photon veto counters. Some of these counters had singles rates of several MHz, so it was important to have precise TOF information for them. Good TOF information required large pulse sizes, which in turn required large amounts of current to power the phototubes.

To provide the large currents needed by our highest rate phototubes, we built special transistor phototube bases. The circuit diagram of the base is shown in Figure 18. Unlike most other high current bases, this type of base will provide any amount of current the phototube requires as long as the transistors remain undamaged, yet the quiescent current drawn by the base is less than 1/2 ma. The bases were tested with pulsed currents of up to 20 ma with no difficulty.

The transistor base circuit was built on a small printed circuit board. A resistor voltage divider was used to generate reference



HIGH-RATE TRANSISTOR BASE
FOR EMI 9813

RESISTORS - 1/4 WATT
RECOMMENDED TRANSISTOR - MOTOROLA 2N5401

Figure 18 Circuit Diagram of Transistor Phototube Base

voltages for the 30 emitter follower amplifiers, each of which provided power to the amplifier directly below. Darlington pairs of high voltage PNP transistors were used to increase the current gain of the amplifiers. Some of these transistors showed excessive leakage currents on their cases in high-humidity environments, which we corrected for by covering all the transistors with Dow Corning R-4-3117 conformal coating. A 10-inch clip line with an 18-ohm terminator was built into the base, making it necessary to isolate the high voltage and signal grounds to avoid ground-loop currents.

We used approximately thirty of these bases on the highest rate veto counters, target counters, and beam counters. Each base was powered by its own power supply, and under typical running conditions the average current drawn by the phototubes during the spill was about 3-4 ma. Most of the bases worked quite reliably under these conditions throughout the entire two-month running period. One exception occurred during a week in which the spill conditions were very poor. During this week the upstream beam counter, which often counted at rates in excess of 20 MHz, could not be used.

The currents drawn by the phototubes were well in excess of the manufacturers' guidelines. Because of this we were not surprised that the gains of the phototubes changed somewhat. After a shutdown period of several days the gain typically would slowly double during the first day of operation. After this initial warmup period the performance was fairly stable, and during the shutdown periods the gain would slowly return to its normal value. We did not observe the presence of any permanent damage to the phototubes.

2.3.5 Cable Dispersion Canceling Devices

When short pulses are transmitted through long distances of coaxial cable, the signal is often distorted considerably. To counteract this effect we used a simple passive filter on most of the photon veto counters. The filter was designed to take advantage of the fact that

the long dispersion tail is roughly exponential in shape. The three principal components, R1, R2, and C1 in Figure 19, were adjusted to produce an overshoot at the input end of the cable with the proper amplitude and time constant necessary to cancel the dispersion tail at the receiving end of the cable. The filter works for all pulse sizes but must be adjusted to match the pulse shape.

The benefit of the filter is illustrated by Figure 20, which shows its effect on signals passing through 140 feet of RG 58 plus 160 feet of RG 174 coaxial cable. The dispersive effects were essentially eliminated. This combination of cables was originally proposed to be used on most of the detector elements, and it was for this situation that the dispersion filters were designed. In the final configuration, however, all the detector cabling was either RG 58 or RG 8, eliminating the need for the filter on the detector elements. The filters were used instead on the veto counters, where, as is shown in Figure 21, they provided a pulse shape of somewhat shorter duration than the unfiltered pulse. This method was considered superior to the use of a clip line. To avoid the generation of ground loop currents the phototube bases were required to have isolated high voltage and signal grounds.

2.3.6 Veto Counter Instrumentation

The target box photon vetoes were divided into four quadrants, as is shown in Figure 7. Each quadrant had four layers of scintillation counters with separate phototubes, all of which had dispersion canceling filters installed. The phototube signals from each section were added by LRS 428F linear fan-in fan-out modules. The output of these modules drove an updating discriminator, whose outputs were fed into an EG&G TD811 CAMAC TDC and a CAMAC latch.

All but a few percent of the hits registered in the latch were accompanied by a hit in the appropriate TDC channel. Since the same signal was sent to both the latch and the TDC, it appears as if the

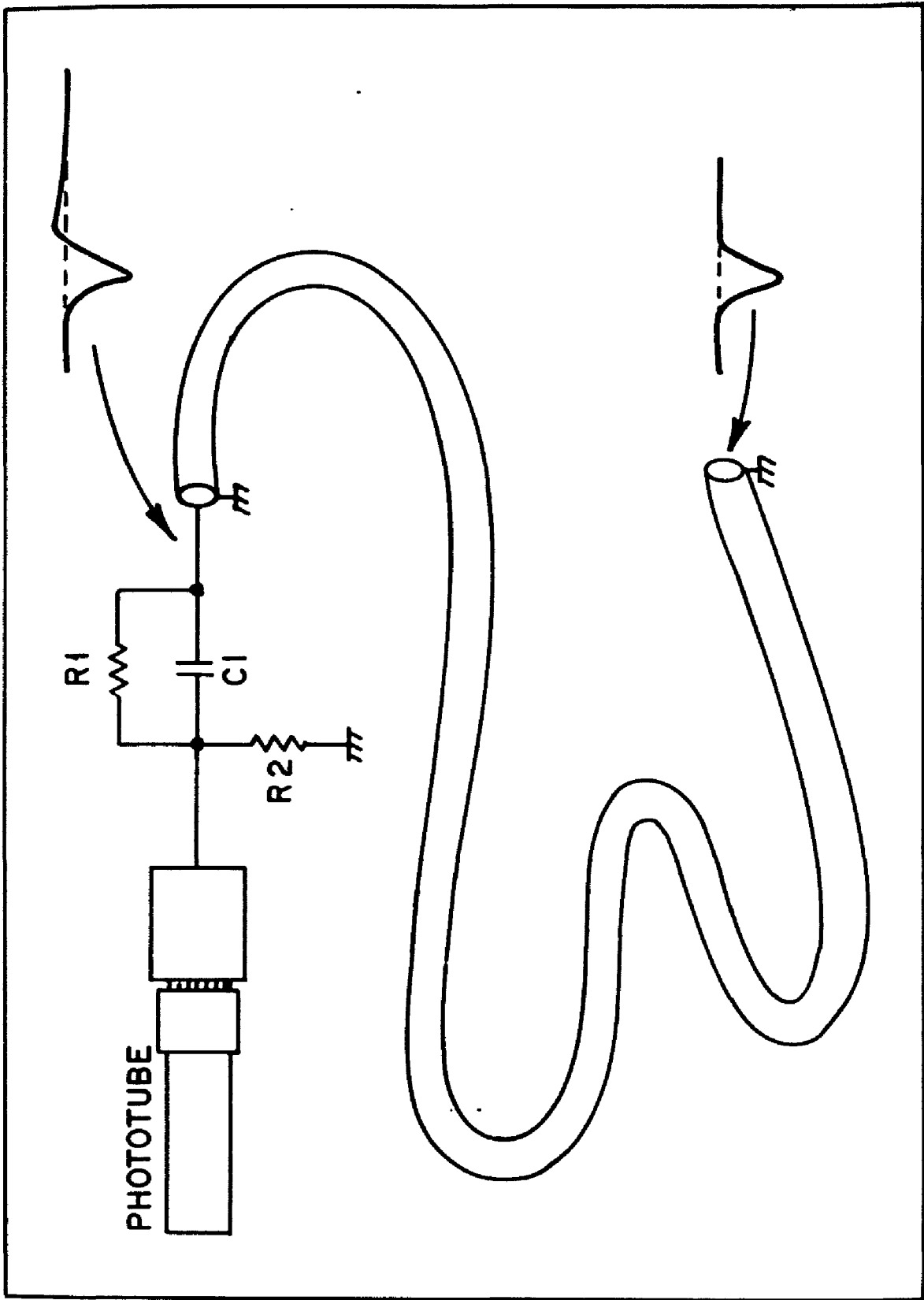
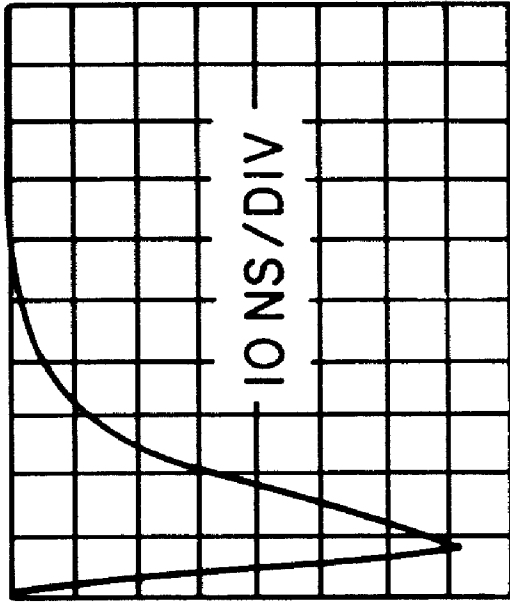
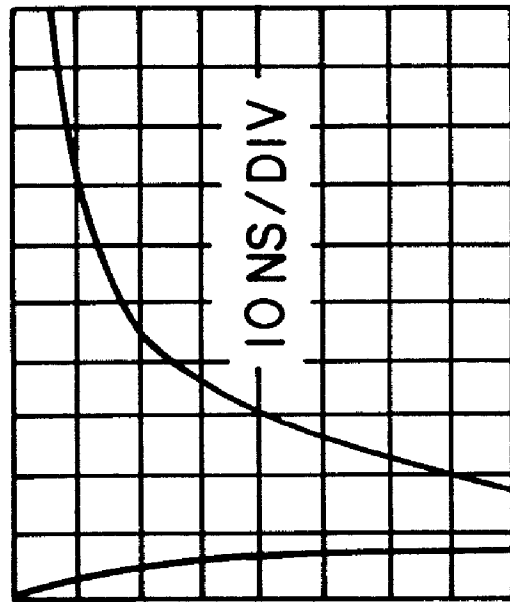


Figure 19 Cable Dispersion Canceling Circuit

EMI 9813

140' RG 58+165' RG 174



NO FILTER

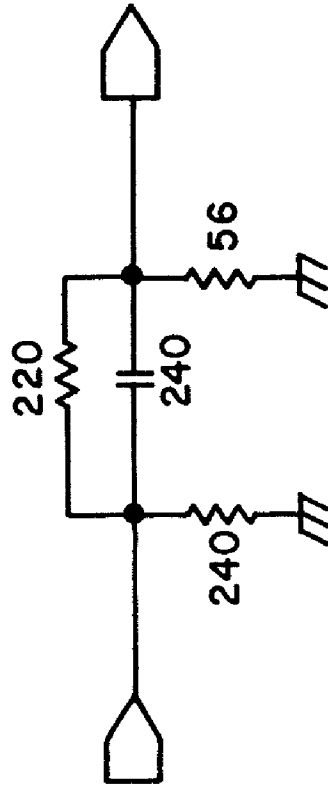


Figure 20 Effectiveness of Dispersion Canceling Filter on Signals Passing through RG 174 Cable

EMI 9813

140' RG 58

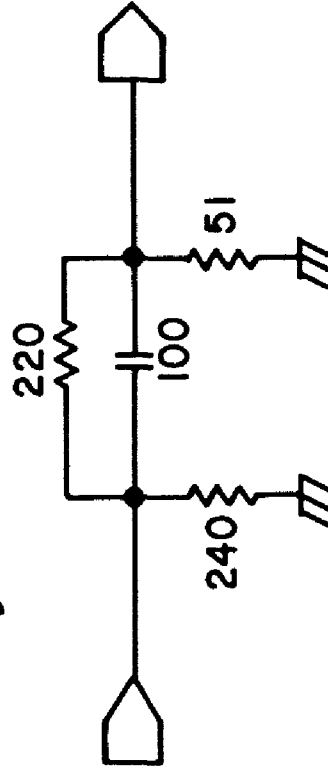
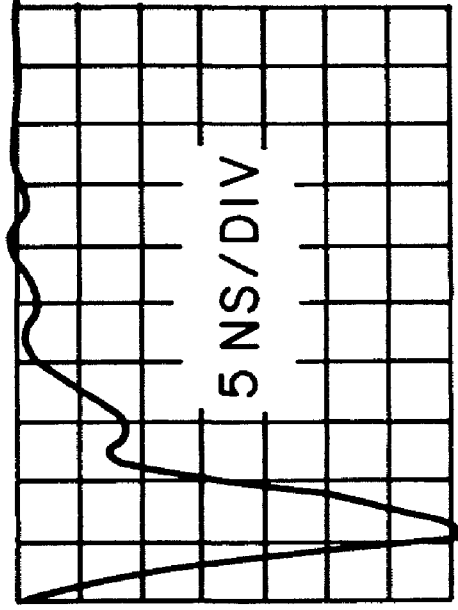
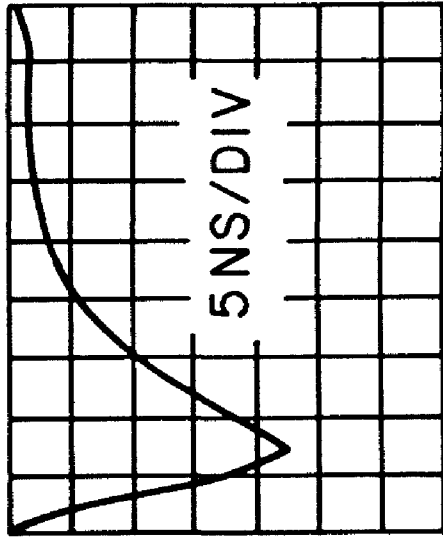


Figure 21 Effectiveness of Dispersion Canceling Filter on Signals
Passing through RG 58 Cable

TDC was slightly inefficient. This small inefficiency was probably caused by the presence of an early hit in addition to the one causing the latch signal. This early hit, if it came just before the start signal, could cause the TDC to be dead for the event while not registering either hit. This effect was confirmed by bench tests of the TDC module.

The high voltages of the target box photon veto counters, and of some charged particle veto counters, were set by comparing the spectra obtained from Compton scattered electrons using a Co^{60} source. These counters were set such that the 50 mV discriminator was sensitive to a single minimum ionizing particle in one layer, as was later confirmed by the offline analysis.

The phototube signals from each downstream photon veto counter were combined by LRS 428F linear fan-in fan-out modules, which were modified to prevent baseline shifts at high rates. The highest rate counters used the transistor phototube base, and all the other counters had dispersion canceling filters installed. One output of the fan-out module drove an updating discriminator set at 50 mV, or roughly the signal size expected for one minimum ionizing particle traversing one of the four scintillators in the veto counter. The outputs of this discriminator were fed into LRS 2228A CAMAC TDCs and a CAMAC latch. Another output of the fan-out module was used to drive a 200 mV updating type discriminator, which was used in the trigger logic. In this manner very large hits in the veto counters were used to reduce the trigger rate, while the small hits were subjected to more refined cuts by the offline analysis.

2.4 Phototube Gain Tracking Devices

To track their gain as a function of time, most detector elements had two devices: a small radioactive source and a fiberoptic light guide connected to a spark gap. The fiberoptic light flasher system

was used as the primary gain tracking device. The gains of all the phototubes were measured with this system once every other spill during all data and calibration runs. The sources were not monitored during normal data runs, but rather special runs were taken approximately once per week to obtain the source calibration.

2.4.1 Radioactive Sources

There are two types of sources used to calibrate the detector elements. A small NaI crystal doped with Am^{241} was glued to the lead glass blocks, while the hodoscope and calorimeter counters each had a small piece of scintillator with an embedded Bi^{207} source attached to their light pipes. During source calibration runs a special trigger allowed the pulse height spectrum of each individual source to be collected and saved on magnetic tape for later analysis. The spectra of the NaI sources showed a peak from the 5.5 MeV α radiation, and the Bi^{207} spectrum had a number of peaks, the most prominent of which was caused by 1.05 MeV internal conversion electrons. The locations of the peaks in the pulse height spectra indicated the relative gain of the phototubes.

2.4.2 Light Flasher System

Figure 22 is a block diagram of the light flasher system for one of the two detector arms. A computer generated trigger caused a 10 ns wide high voltage pulse³² to be sent to a spark gap. The resulting flash was viewed by all the phototubes on the arm through fiberoptic³³ light guides, which were glued to the light pipes. The intensity of each flash was monitored by a photodiode. In this manner the response of each detector element was measured with respect to the photodiode. The performance of this system will be discussed in Section 3.4.

32 H.V. pulser and spark gap manufactured by:
Xenon Corp. Wilmington, Mass.

33 Fiberoptic light guides manufactured by:
Galleo Electronics. Sturbridge, Mass.

LIGHT FLASHER SYSTEM BLOCK DIAGRAM

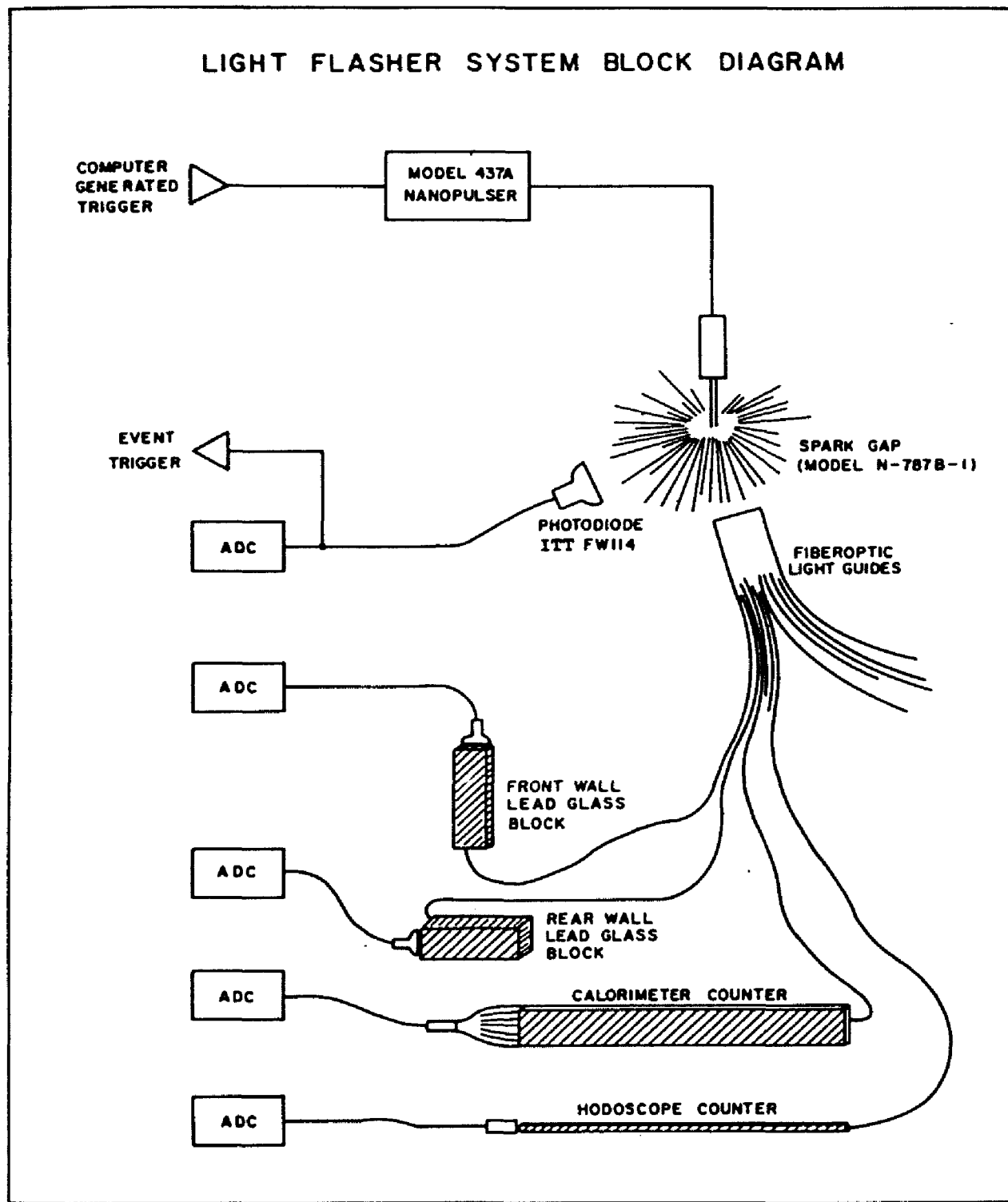


Figure 22 Light Flasher System Block Diagram

2.5 Data Acquisition System

The experiment was controlled by an online PDP15 computer with 64K of memory. Information generated by the events was read from the CAMAC system into the core memory during the spill and copied to magnetic tape between spills. Approximately 21 events could be stored in the memory buffer during the spill. At the end of each spill the CAMAC scalars were also read out and copied to tape. In addition to the data logging tasks, the computer made extensive checks on the data to insure that all the detector elements were functioning properly.

The readout time for an event was approximately 10 ms. The data were written on 800 BPI 7-track magnetic tape at a maximum rate of three tapes per hour. Typically two tapes were written in an hour.

In addition to the main data acquisition program, a number of smaller special purpose programs performed such tasks as taking source and calibration runs or testing the CAMAC system and its modules.

2.6 Setting the High Voltage of the Detector Elements

It is important when using an energy sum as a trigger requirement that the energy response of the individual detector elements be normalized. To accomplish this a special program on the PDP15 collected the pulse height of 6 GeV electrons during the electron calibration runs for events in which most of the energy in the layer was deposited in the block under test. On the basis of this procedure, the energy responses of the calorimeter and lead glass counters were quickly set to within about 10% of the correct values by adjusting the high voltages of the phototubes. The hodoscope counter high voltages could not be set by this method; rather each was initially calibrated with minimum ionizing particles in a test beam, and then the Bi²⁰⁷ sources were used to monitor their gain afterwards.

2.7 Special Diagnostic Triggers

In addition to the main trigger, a number of other triggers were used to monitor the performance of the apparatus. For instance, the energy response of the veto counters was measured by triggering on minimum ionizing particles passing through the veto counters. This information was used to adjust the high voltage on these counters. Another such trigger, which we called the "open trigger", simply required energy to be deposited on each detector arm in coincidence with a beam particle. These events were taken at the start of each spill, just as the beam intensity was beginning to build up and the rate was substantially less than 10 MHz, and were used to calibrate the veto counter TDCs. In addition, special runs were taken at lower beam energies to measure the cross sections of several well-known resonances, as is described in Chapter 5.

2.7.1 Electron Runs

To calibrate the energy response of the detector elements, special runs were taken in which the two Cherenkov counters were used to trigger on electrons. The electrons were bent horizontally into the detector arms by a dipole magnet placed directly in front of the experiment, as is shown in Figure 6. Each detector arm was mounted on a hydraulic table that allowed movement in the vertical dimension. In this way the electron beam could be aimed at almost every detector element. The calibration runs were performed with the detector arms in place, although the downstream photon vetoes had to be removed.

The electrons were also used to simulate photon showers in the detector. For all practical purposes electron and photon showers, although they start one radiation length apart in the detector, are indistinguishable in the detector; thus the pattern recognition efficiency for photons was determined using these electrons. The electron normalization runs were taken at five different beam momenta, 2, 4, 6, 8, and 10 GeV/c. The beam passed through a hole in a

2 radiation length thick lead scintillator shower counter in an attempt to remove events in which the electron was accompanied by a bremsstrahlung photon.

2.7.2 Single Arm Runs

Additional test runs were taken with the beam pointed at the center of one of the detector arms, as in the electron runs, but with the target moved into the beam approximately 6 meters in front of the detector. For these runs the downstream photon vetoes were rearranged to compensate for the different target position. These runs were taken at 5 different beam momenta, 2, 4, 6, 8, and 10 GeV/c, and provided test particles that were used to calibrate the photon energy scale as is described in Section 4.2.

Chapter III

CALIBRATION PROCEDURES AND FIRST PASS ANALYSIS

The analysis of the more than 1500 data tapes taken during the two-month running period was divided into two steps. The first pass involved such straightforward procedures as the conversion of TDC values into nano-seconds and ADC counts into energies. No event selection or pattern recognition was performed during the first pass. All data events were copied to secondary tapes in a special format optimized for the 60 bit word length of the CDC 7600 computer, which was used for the offline analysis. In addition, diagnostic information was generated that determined the quality of the data on the individual tapes. Although the tasks involved seem simple, this first pass analysis represented the major cost in the analysis project both in CPU usage and programming time.

3.1 ADC Pedestal Processing

By far the most difficult calibration task was that of determining the energy response of the detector elements as measured by the LRS 2249A ADC channels. We needed to determine both the slope and the intercept of their response to deposited energy. The slope was monitored by analysis of the light flasher events, and the intercept was measured by analyzing the pedestal events, which were simply events generated at times when no particles were in the detector.

In principle this should have been a simple process, but we found that quite often the pedestal values would change. In some cases this might not have been the fault of the ADC—for instance, loose cabling would cause such an effect—but we have evidence that at least some of these problems were caused by the ADC. Figure 23 shows a history of the pedestal values measured in the 12 ADC channels of one Camac

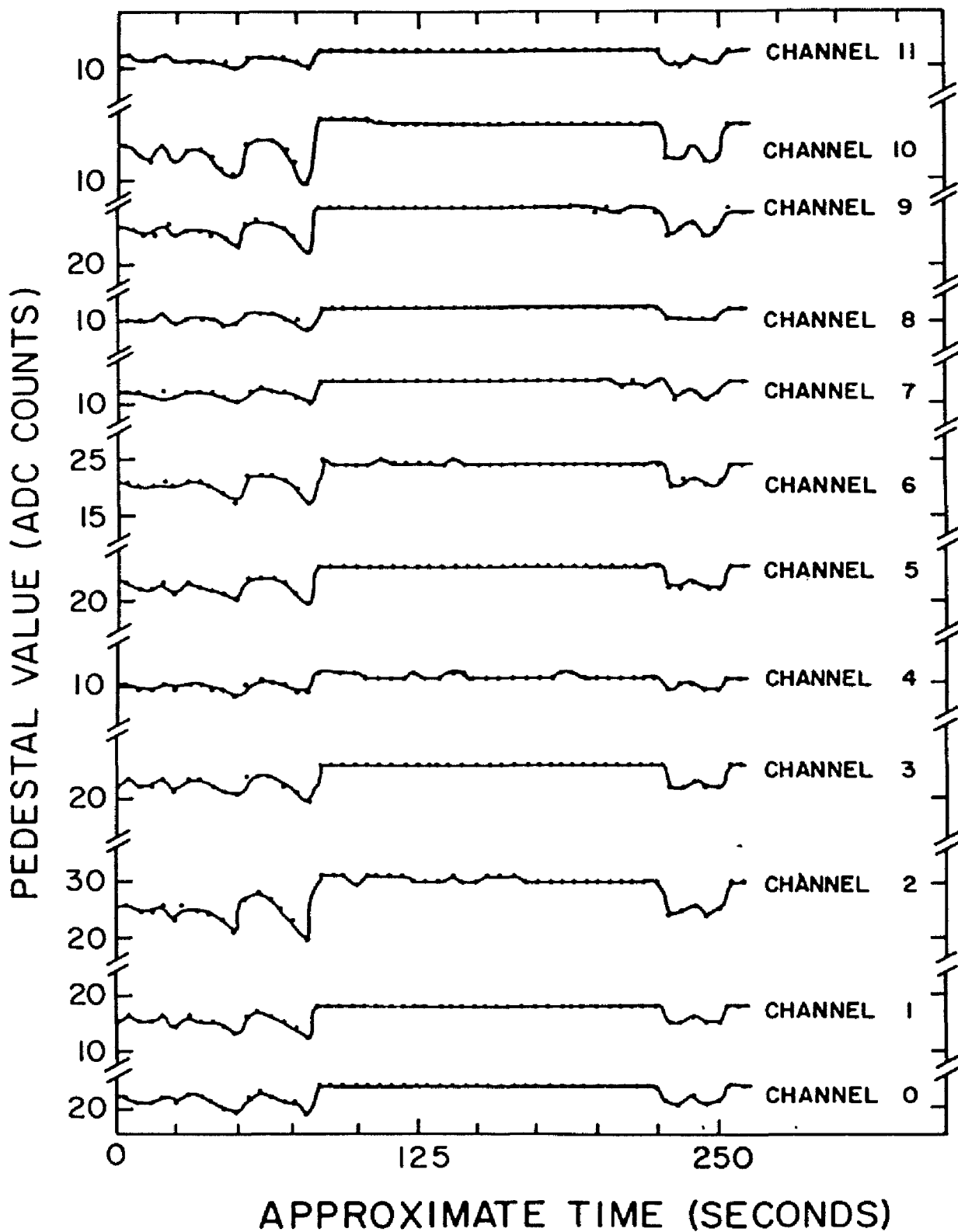


Figure 23 Short History of the 12 ADC Channels of One Bad ADC Module

module during one data run. All the channels drifted in unison, with one channel showing a shift of 12 ADC counts. The analysis program kept careful track of the ADC modules with drifting pedestal values. In addition, ADC modules with severe problems, such as that shown above, were identified and replaced during the run. All further references to the ADC data will assume that the pedestal has been subtracted.

3.2 Light Flasher Event Processing

The principal way in which we kept track of drifts in the gain of the detector elements was through use of the light flasher events. These were collected every other spill on each arm. The changes in gain of the phototubes were expected to be small over the time span of an hour or less, which usually represented one data tape, so the light flasher information for an entire data tape was combined to form one measurement of the relative gain per channel. For each light flasher event the ratio of the pulse height in each channel to the pulse height in the photodiode was formed. These ratios were averaged for the entire data tape and saved for use in the later steps in the analysis. They were subsequently compared with the corresponding value measured during the electron normalization run and used to determine the change in gain since that time. They will be referred to as the "normalized light flasher pulse height" in the sections below.

3.3 Gain Calibration

Neither the light flasher nor the radioactive sources served as an absolute measure of the energy responses of each channel but only tracked changes in the response relative to its value at a standard time. To determine the absolute gain of each channel special runs were taken with a well-collimated electron beam that was aimed at most

detector elements. This section will only describe how the responses of the phototubes in each layer were normalized to each other. The procedures used to determine the absolute energy response will be described in the next chapter.

Because of bremsstrahlung losses encountered in the beam line, the electron beam contained a spectrum of momenta that were spread across the detector by the dipole magnet used to bend the beam into the detector. By selection of electrons within a narrow position window centered on the spatial peak of the distribution, a momentum spread of approximately 1-2% was obtained.

3.3.1 Primary Lead Glass and Calorimeter Counter Calibration Procedures

Several different methods were used to analyze the electron calibration data. The most straightforward method was used on the lead glass blocks and calorimeter counters. These counters were wide enough (6 inches) to contain the transverse development of the electromagnetic shower within the element on which the beam was directed. It was important that the center of the beam spot be located near the center of this detector element. The relative energy response was then determined by measuring the average pulse height produced by electrons in the counter. Figures 24 and 25 show typical pulse height distributions obtained by this method.

This calibration procedure was repeated at several locations for the front lead glass and calorimeter counters. The resulting information was used to establish attenuation curves for each individual detector element. The calorimeter counters typically had an attenuation over their length of about 50%, and the front wall blocks had an attenuation of about 10%.

3.3.2 Hodoscope Counter Calibration Procedure

As the hodoscope counters were only 1 inch wide, the transverse spread of the electron shower was seldom contained in just one

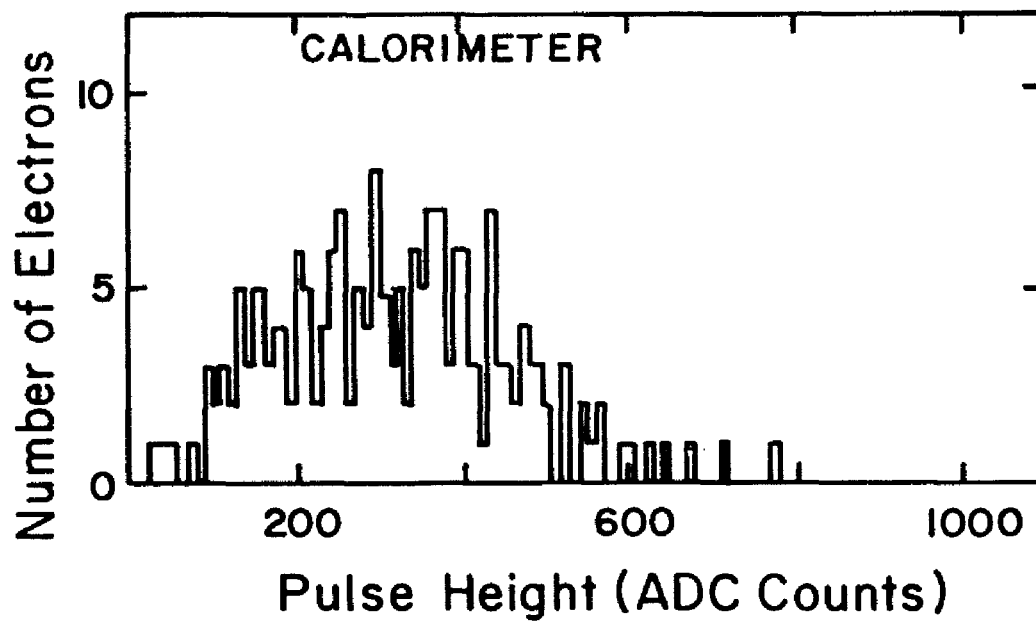
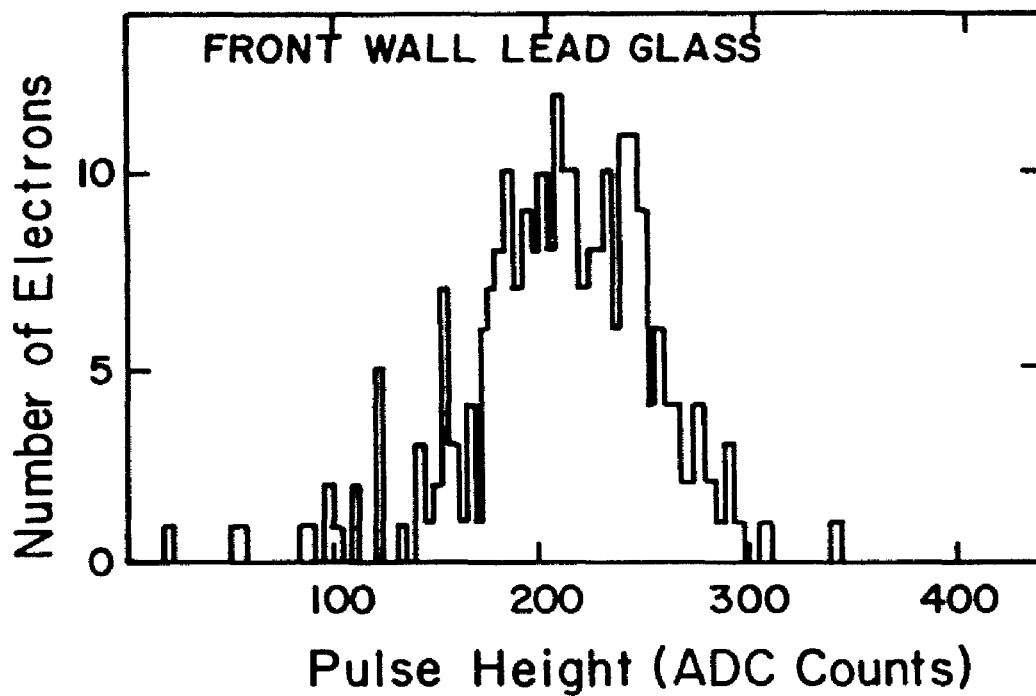


Figure 24 Pulse Height in Front Lead Glass Wall and Calorimeter for 6 GeV/c Electrons

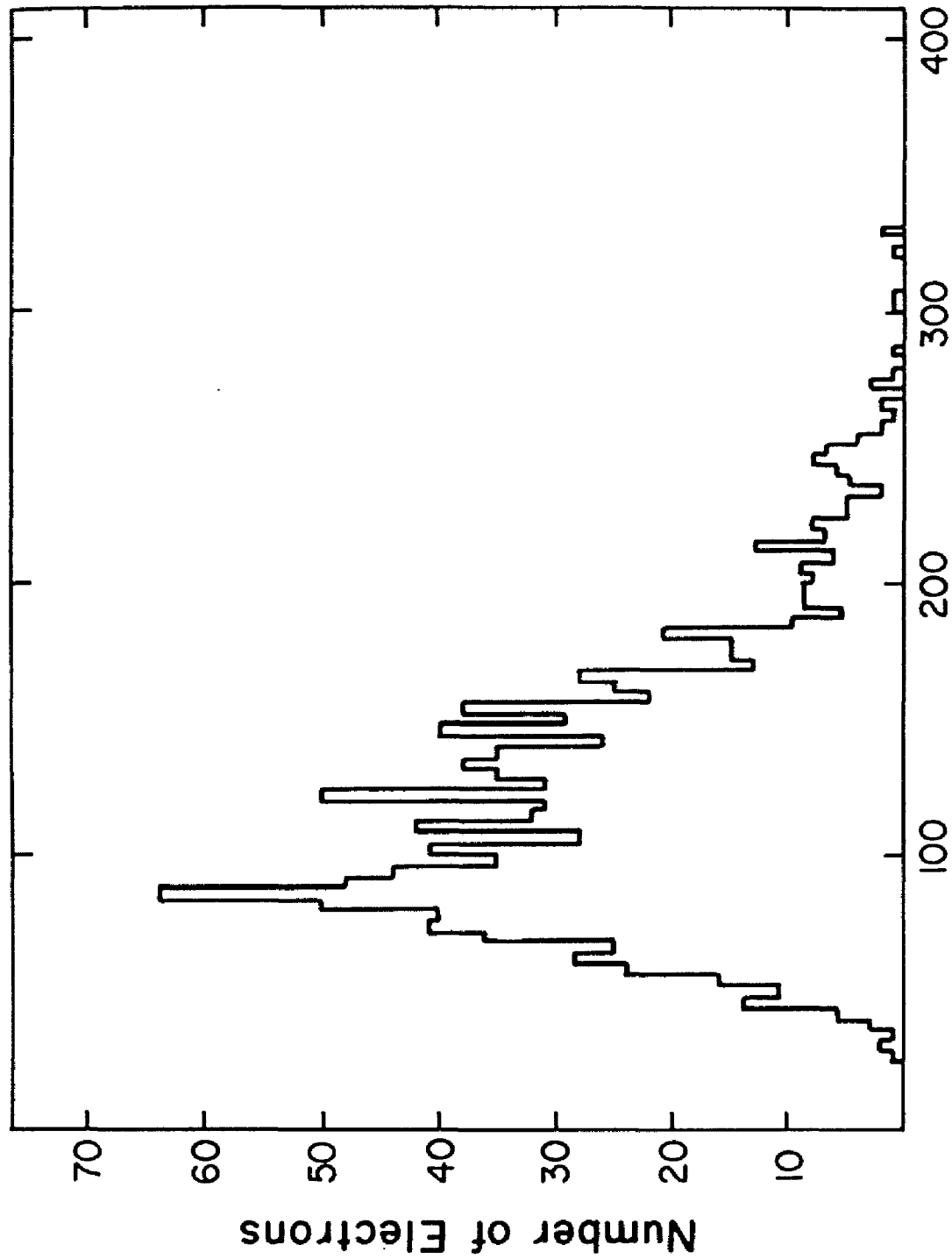


Figure 25 Pulse Height in Rear Lead Glass Wall for 6 GeV/c Electrons

counter. Typically two counters in each dimension shared the energy. The gain coefficients were therefore found by solving a set of coupled equations. If the gains of the counters were known and the measured pulse heights were perfect, the following equation would apply:

$$\langle \text{mean energy} \rangle = \sum_{i=\text{counters}} P_{i1} G_i$$

where: P_{i1} \equiv pulse height of i^{th} hodoscope counter in 1^{th} event
 G_i \equiv energy normalization factor of i^{th} hodoscope counter

We wanted to find the set of gains that minimized the chi-squared:

$$\chi^2 = \sum_{l=\text{events}} (\langle \text{mean energy} \rangle - \sum_{i=\text{counters}} P_{il} G_i)^2$$

The following gain vector minimized the chi-squared:

$$\begin{bmatrix} G_i \end{bmatrix} = \langle \text{mean energy} \rangle \begin{bmatrix} \sum_{l=\text{events}} P_{il} \end{bmatrix} \begin{bmatrix} \sum_{m=\text{events}} P_{im} P_{km} \end{bmatrix}^{-1}$$

The hodoscope gains were determined by solving the above matrix equation, which involved one matrix inversion. The gains were determined at several points along the length of the hodoscope counters by this method, allowing attenuation curves to be measured for every counter. The attenuation of a typical hodoscope counter was approximately a factor of 2-3 from one end to the other. Figure 26 shows the attenuation curve measured for a typical hodoscope counter.

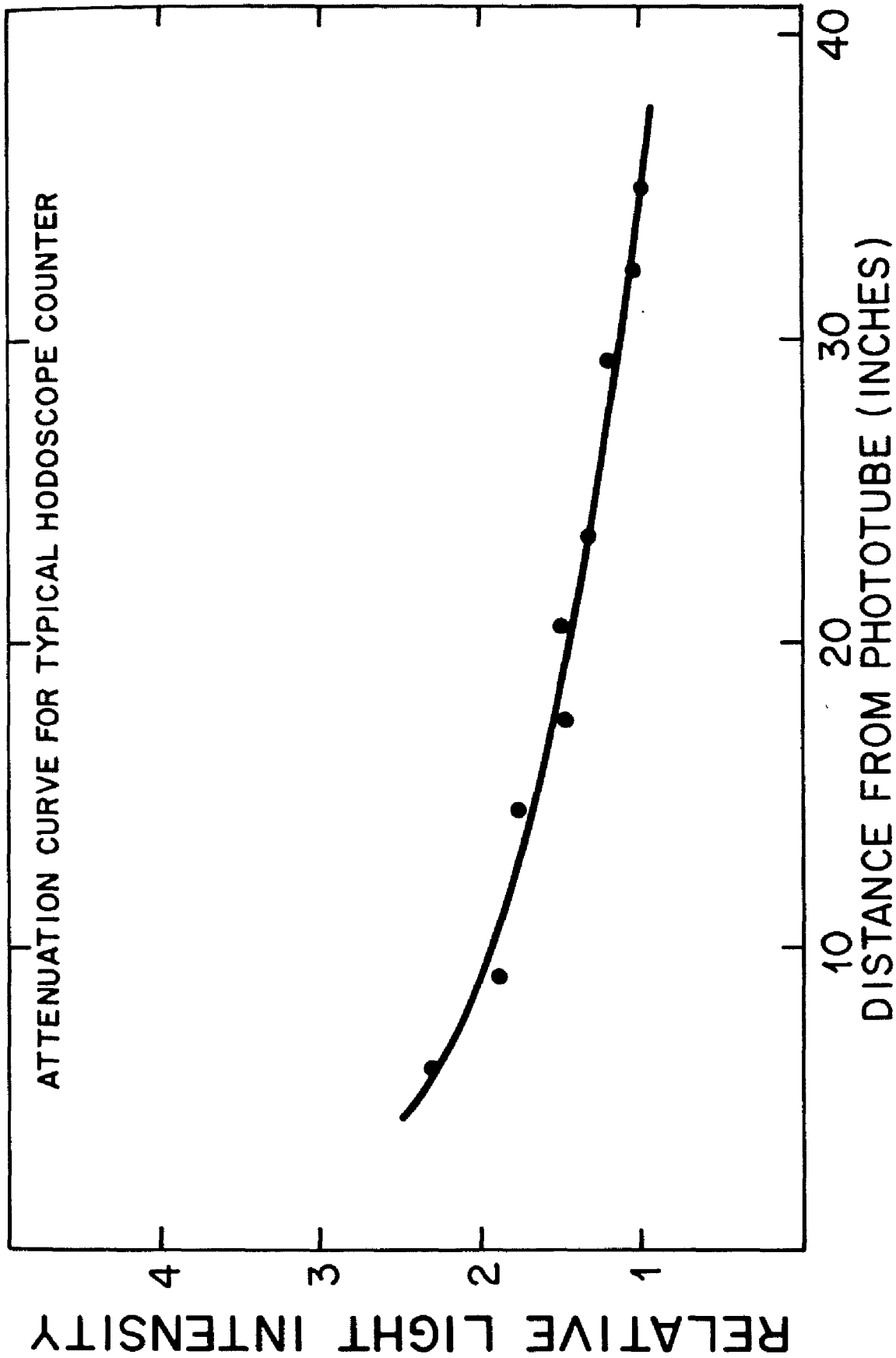


Figure 26 Typical Hodoscope Counter Attenuation Curve

3.4 Calibration Consistency and Problems

In principle we needed only one calibration run normalizing the response of the detector elements at one time, and forever afterward the light flasher system would determine the gain changes since that calibration. Fortunately we took several calibration runs, which allowed us to check how well the procedures worked. In addition, the radioactive source information was extremely useful as an independent measurement of the response of the detector elements.

3.4.1 Radioactive Source Processing and Results

To analyze the radioactive source data the peaks were found in the pulse height spectra for each channel. In addition, the normalized light flasher pulse height for each channel was found by the procedure described in Section 3.2. To compare the results of different source runs the ratio of these two quantities was formed. This ratio represented the light intensity of the sources, which should have remained invariant. A sample of these results is shown in Table 3 for several different NaI source runs.

The first channel in the table is a good example of one common type of problem encountered. The light flasher response for this channel suddenly dropped by a factor of two between different source runs, while the NaI signal remained roughly constant. This type of problem, which occurred in 5-10% of the channels, often occurred in channels where the fiberoptic light guide was loose or had fallen off the block.

A second type of problem shown in Table 3 was an apparent systematic drift in the light flasher response with respect to the NaI signals. This shows up more clearly in Figure 27, where the light intensity of the sources, as was measured in the source run of 6/26/80, is compared with that measured at several other times. We expect to see a gaussian distribution centered at 1, with a width representative of the random error in this calibration procedure.

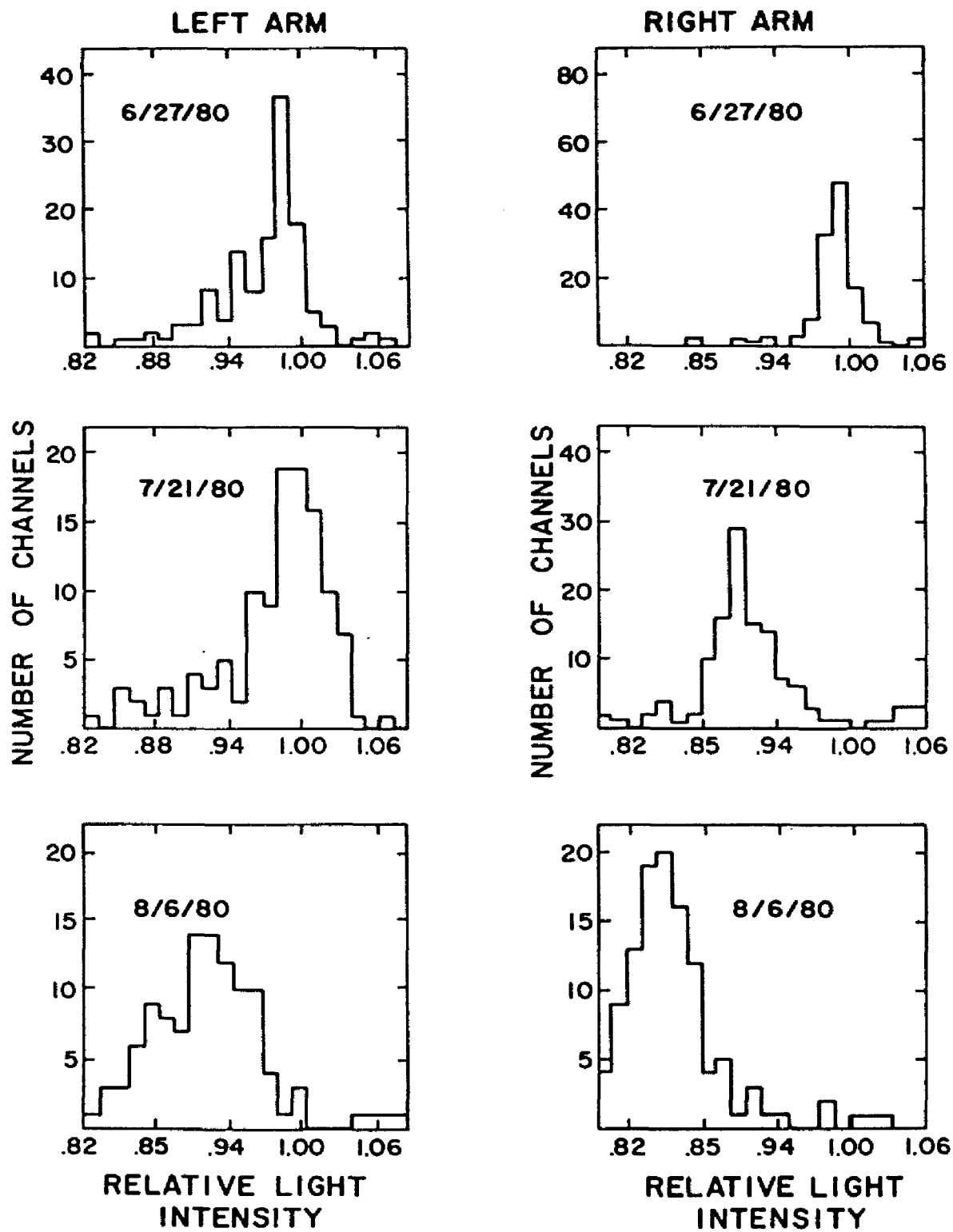


Figure 27 Relative NaI Light Intensity as Function of Time

Instead we see systematic shifts in the ratio by factors of up to 15%. These drifts were caused by a systematic error in the light flasher calibration procedure. This problem will be discussed in greater detail in the following section.

TABLE 3
Sample Results from NaI Runs

Counter	6/26/80	6/27/80	7/5/80	8/6/80	
L005	294	242	172	132	<LF>
	257	251	238	245	<NaI>
	1.14	.97	.73	.54	<LF>/<NaI>
L006	532	534	522	563	<LF>
	106	105	104	101	<NaI>
	5.02	5.08	5.05	5.56	<LF>/<NaI>
L007	335	340	333	343	<LF>
	96	95	94	93	<NaI>
	3.49	3.57	3.53	3.70	<LF>/<NaI>
L008	183	182	185	203	<LF>
	109	108	111	114	<NaI>
	1.67	1.68	1.67	1.78	<LF>/<NaI>
L009	98	97	98	104	<LF>
	76	74	72	75	<NaI>
	1.29	1.30	1.36	1.40	<LF>/<NaI>
L010	988	1010	1011	1057	<LF>
	107	107	109	106	<NaI>
	9.25	9.44	9.29	9.97	<LF>/<NaI>

3.4.2 Systematic Drifts in the Calibration Procedures

I will compare the results of two electron normalization runs, one taken at the beginning of the running period, and one taken in the middle of the running period. For purposes of comparison the ratio of the electron response to the normalized light flasher pulse height was formed. This ratio represented the light intensity produced by the

electrons and should have remained invariant. The ratio of the light intensities measured in the two calibration runs was then formed and is shown histogrammed for all channels in Figure 28 for the left and right arms. We expect to see a gaussian shape centered at 1, but instead we see a gaussian shape displaced by as much as 6-7% on the right arm. This is a clear indication of a systematic error in the energy measurement procedure. The source runs showed the same systematic drifts in response when normalized to the light flasher, as did the invariant mass of π^0 's detected on the two arms.

One very obvious cause of such a shift could be that the photodiode did not accurately measure the intensity of the light flasher as measured by the phototubes. There are two means by which this could have occurred. The first would involve changes in the photocathode response to light as a function of temperature. This effect, however, seems to be too small to have caused the large error observed. The second and more probable possibility involves the nature of the light flasher itself. I have little data on the light spectrum of the flasher, but it seems possible that the spectrum was not constant in time. This would be unfortunate, since in all certainty the spectral responses of the photodiode and the fiberoptic-phototube combinations differed. Another simple explanation for the systematic drift could be that the response of the ADC changed slowly over the two-month running period.

No matter what caused the systematic drifts in the light flasher response, the solution to the problem was not difficult, since the effective response of all detector elements on an arm changed in unison. We simply measured the invariant mass of the π^0 's on each arm and constrained it to be a constant.

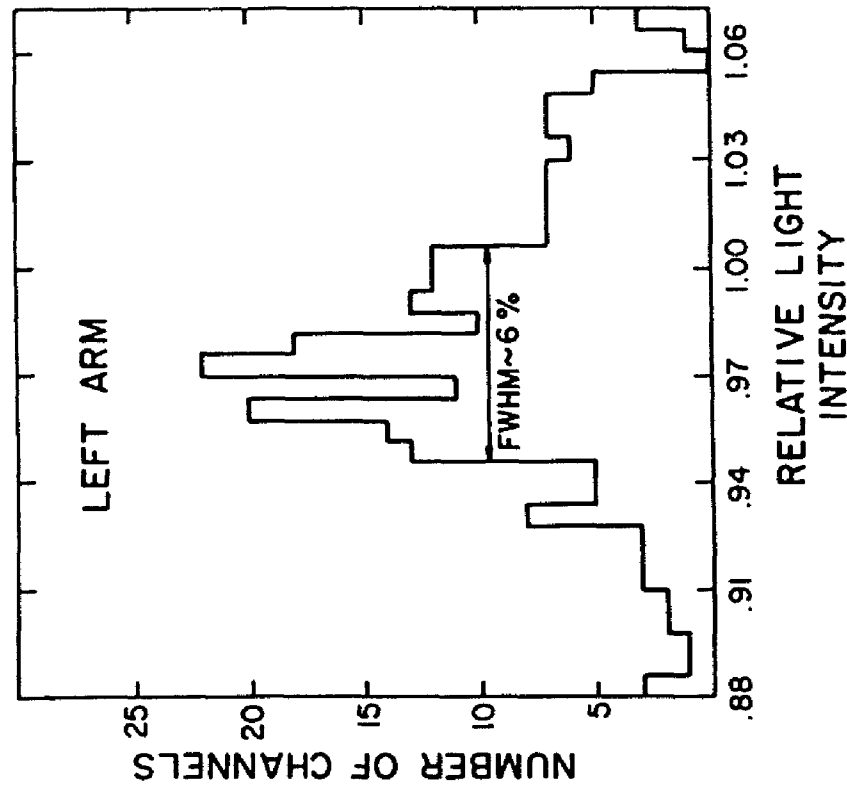
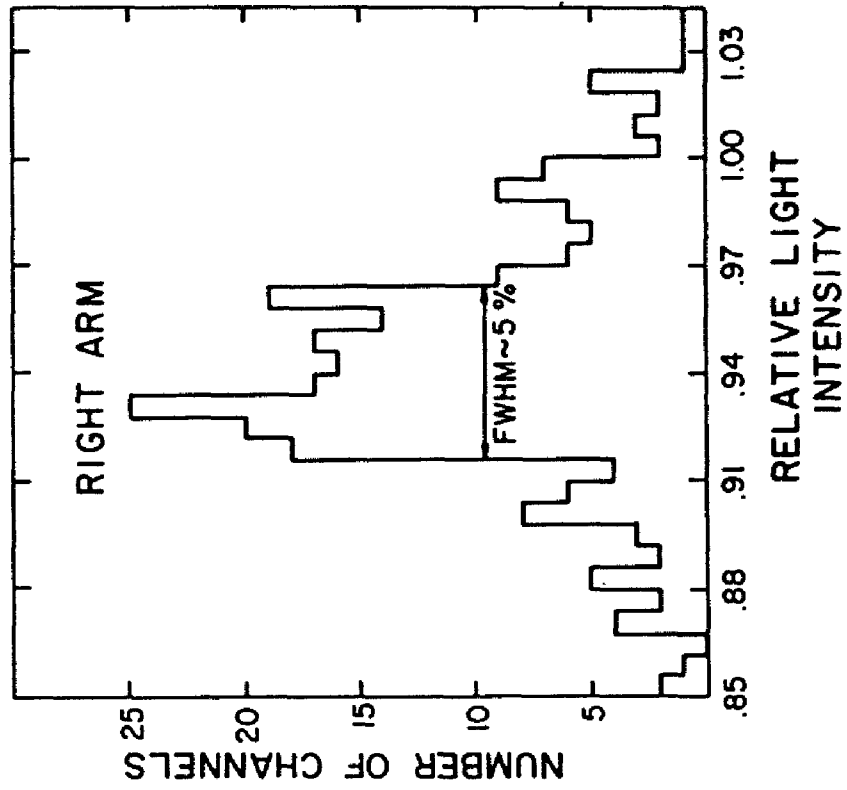


Figure 28 Relative Electron Light Intensity as Measured in Two Calibration Runs

3.5 Time of Flight Calibration and Performance

To fully calibrate the TDC information it was necessary to measure the slope (i.e., nanoseconds/channel), as well as determine the interaction time, but in our case the interaction time was the only critical parameter. This was because we only wanted to know if a hit in the detector was produced by reaction products from the beam particle that caused the trigger interaction, or by products of the reaction of another beam particle arriving in the detector at a different time. Since most hits in the detector elements were produced by the correct beam particle, the calibration task was very straightforward. A histogram of the TOF of large pulse height hits was made for each channel, and the resulting peak caused by the "in-time" hits was defined to be the "zero time". The process was similar for the veto counters, but good trigger events should not have had any veto counter hits, so these channels were calibrated using the open trigger³⁴ events.

An additional correction was made to the TOF to correct for "time-slewing". This was a very important correction, since we detected pulses with slow rise time at levels near the discriminator threshold. For example, a hit with 5 ADC counts was corrected by 4.5 ns in the calorimeter counters, 6 ns in the veto counters, 10 ns in the hodoscope counters, and 17 ns in the lead glass counters. A small correction was also made to the calorimeter and hodoscope TOFs to adjust for propagation delay of the light from hits at the far end of the counters. Table 4 shows the typical time resolution of the various counter types after these corrections had been made.

TABLE 4
Time Resolution of Detector Elements

<u>Counter Type</u>	<u>Resolution FWHM</u>
Veto Counters	4 ns
Calorimeter Counters	5 ns
Hodoscope (large pulse height)	4 ns
Hodoscope (small pulse height)	6 ns
Lead Glass (large pulse height)	6 ns
Lead Glass (small pulse height)	8 ns

3.5.1 Lead Glass TOF Problems

The discriminators for the lead glass counters had an unfortunate tendency to produce output pulses of different output widths dependent on the input pulse size. The normal output pulse width was 100 ns, but with large input signals the output pulse width changed to about 50 ns. This normally would not have been a problem, but it caused considerable difficulty when these signals were used to drive the LRS 2770 TDCs. These TDCs, which measured the time interval from the leading edge of an input signal to the common stop signal, required about 100 ns to digitize a hit. During that time they did not lock out other leading edges. If a second pulse came in while a previous one was digitizing, both were recorded incorrectly. We did not fully realize the importance of this problem until it was too late to be corrected.

Only 5-10% of the lead glass TDC channels are known to have had problems. What we saw in the problem channels was a near 100% correlation between TOF and pulse height. The most common type of problem involved a shift of 10 ns in measured TOF above a pulse height of 50 ADC counts, or approximately 500 MeV of energy. This fortunately was not a region in which the TOF information was very

³⁴ See Section 2.7 for a description of the open trigger events.

crucial. Most interactions deposited very little energy in the detector, and thus the chance that they would deposit 500 MeV in a single counter was small. Such large hits were almost certain to have been caused by the beam particle that satisfied the energy requirements of the trigger. The TOF information for these large hits was simply ignored.

Chapter IV

PATTERN RECOGNITION AND EVENT SELECTION

This chapter will describe the pattern recognition and event selection procedures used to classify the events, as well as the procedures used to measure the efficiency and effectiveness of the cuts. The hardware trigger was by far the main event selection process. It was responsible for a reduction in the data sample of almost six orders of magnitude, while the offline analysis cuts reduced the sample by only three orders of magnitude. The hardware trigger, however, selected events on the basis of very well-defined characteristics, whereas the offline event selection cuts generally attempted to identify the often subtle variations between $\pi^0 \pi^0$ and true $\gamma \gamma$ events. When such tight cuts are made in order to eliminate a large background, there is a danger that the true signal events will also be thrown out. Because of this a little more detail than usual will be given concerning the analysis procedures. I hope to make clear not only what cuts were made, but also how we chose the cuts and why we believe that these were the best cuts to make.

4.1 Pattern Recognition in Detector

Event reconstruction in the detector began with the rear lead glass wall and proceeded forward one layer at a time. The struck counters were grouped into showers, defined as collections of counters that were either in the same layer and adjacent to another counter in the same collection, or were in another layer and overlapped other counters in the collection from the layers behind. Showers could be caused by one or more incident particles. For instance, the two photons from a high energy π^0 decaying with minimum opening angle usually produced a single shower, which we call a "two-photon shower", while a low-energy π^0 could produce two distinct "one-photon

showers". Approximately 80% of the π^0 's detected during the normal 13 GeV/c running were detected as a two-photon shower. Only hits in the lead glass were used to create showers. Struck counters in the hodoscopes and calorimeters that did not overlap showers were recorded but were not used to start a new shower.

4.1.1 Rear Lead Glass Wall Processing

To find the showers in the rear lead glass wall the individual counters were first scanned to determine which counters had hits resulting from the neutral-final-state trigger. These requirements are listed in Table 5.

TABLE 5
Hit Requirements for Lead Glass Counters

- | | | | |
|--------|--------------------------|-----|-------------------|
| 1) | PH < 7 | and | -25 < TOF < 25 ns |
| or: 2) | PH > 7 | and | -20 < TOF < 20 ns |
| or: 3) | Latch was set but no TOF | | |
| or: 4) | PH > 40 | | |

The 7 x 16 matrix of lead glass blocks was scanned and broken into clusters of adjacent hit blocks. Each cluster was stored as a separate shower. Blocks touching on a diagonal were considered adjacent as well as blocks touching on a side. The pulse height distributions of the showers were projected in two dimensions, and showers with two peaks in either projection were flagged as having two photons, but no attempt was made to divide such clusters into two showers. This information was later compared with that from the hodoscopes, which bore the primary responsibility of distinguishing between one- and two-photon showers.

Position information was also gathered about the showers. An x-y window was formed equal to the maximum extent in blocks of the shower and was used to match hits in the forward layers to the shower. The x-y position and the error in the position were also calculated using the energies in the rear lead glass. Most showers had hits in a large number of blocks, allowing the "center of gravity" to be determined with an accuracy of better than an inch.

4.1.2 Front Lead Glass Wall Processing

Roughly 30% of the energy of a typical 6 GeV photon was deposited in the front lead glass wall. Low-energy photons, however, could deposit all of their remaining energy in the front wall and not be detected in the rear wall. This happened in approximately 5% of all cases where a π^0 produced two separate showers. To allow for this possibility a struck front wall block could either be added to a shower found in the rear wall or be used to start a new shower. Creating new showers had to be done with great caution though, since fluctuations in the shape of a one-photon shower could cause it to resemble a two-photon shower.

Hits in the front lead glass wall had to pass the same requirements as shown in Table 5 for the rear lead glass wall counters. Every front wall block with a hit within the position window set up by a rear wall shower was assigned to that shower. In addition, all front wall blocks with hits adjacent to another front wall block in the shower were assigned to that shower, even if they were outside the window of the shower.

Front wall blocks could be assigned to more than one shower. If a block was assigned to two showers and was within the window of only one, the pulse height was assigned to that shower. Otherwise the pulse height was split in proportion to the rear wall pulse heights of the two showers. If the block belonged to more than two showers, the pulse height was split proportional to the pulse heights of the rear wall showers.

After the process of matching front wall blocks to showers was complete, the front wall blocks were scanned again. Any remaining blocks with hits, but not yet assigned to showers, were grouped into clusters of adjacent blocks and used to form a new shower.

4.1.3 Hodoscope Counter Processing

The front and rear lead glass layers gave a good measurement of the energy of the shower, but with their cell size of 6 inches they did not give very detailed information regarding structure within the shower. For example, the photons produced by an 8 GeV π^0 could hit the detector within eight inches of each other. The chances of distinguishing such a shower from a true single photon shower using only the 6-inch-square matrix of lead glass counters were small, if not zero. We relied on the hodoscope counters with their one-inch segmentation to give a clear image of the two photons in such a case. To do this a finer distinction than "shower" was needed, and we named this entity the "hodoscope peak". Several hodoscope peaks in each dimension could be included in one shower. Ideally there would be a one-to-one correlation between a photon and one hodoscope peak in each of the horizontal and vertical hodoscopes.

Hodoscope peaks were found without reference to the showers in the lead glass. The hodoscope counters were first scanned to determine which were hit. The hit requirements were defined in a way similar to that in the lead glass, as shown in Table 6.

TABLE 6

Hit Requirements for Hodoscope Counters

- 1) $-20 < \text{TOF} < 20$ ns
- or: 2) Latch hit but no TOF
- or: 3) $\text{PH} > 3$ and (no latch) and (no TOF)

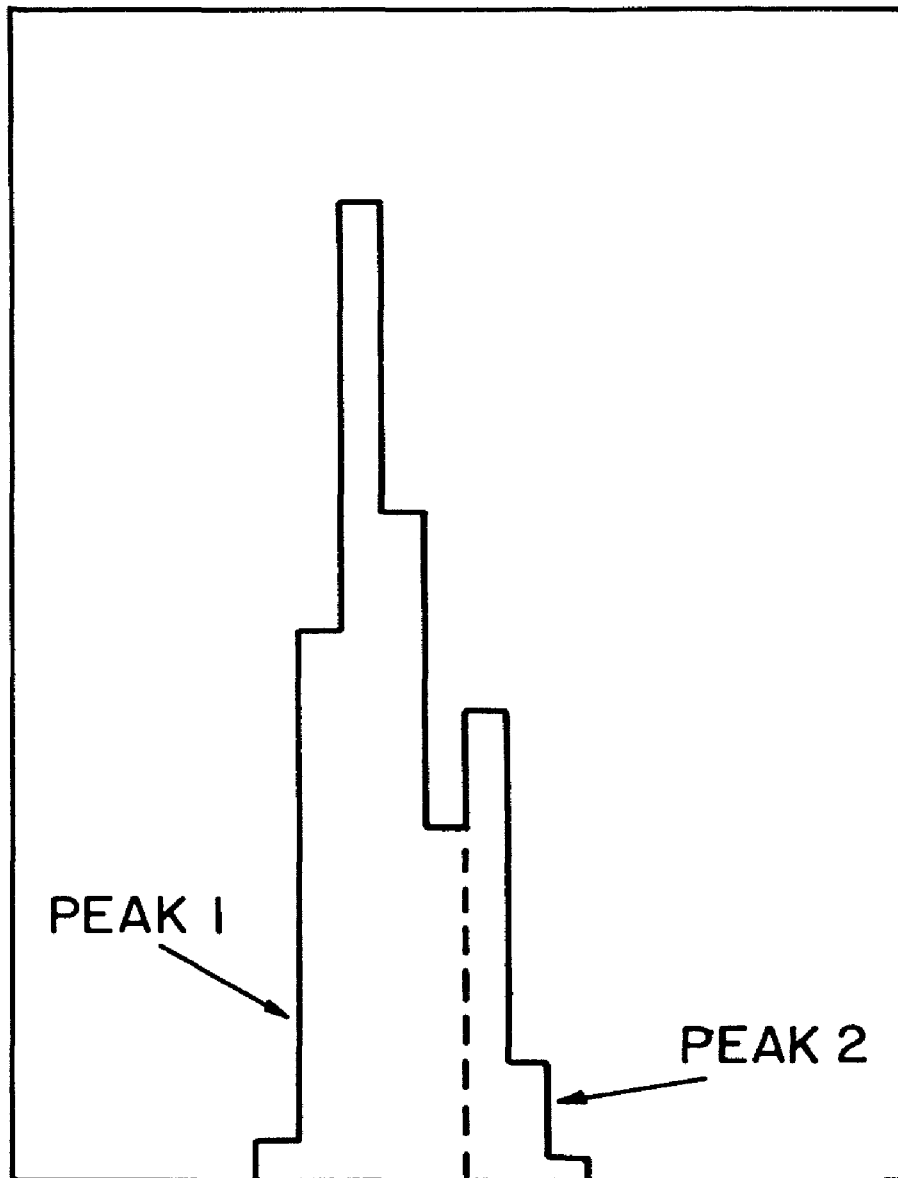
Hodoscope peaks were clusters of hit hodoscope counters. Typical hodoscope peaks consisted of three to four counters. To obtain the best granularity, groupings of counters such as in Figure 29 were divided into two peaks as shown. This may seem a little risky, but at this stage the task was to gather the most detailed information. The information was later reviewed and extra peaks caused by statistical fluctuations and dead counters were coalesced, as described in Section 4.3.

The hodoscope peaks were matched with the showers by projecting the window of each shower to the hodoscope plane and looking for peaks that fell within the window. To avoid confusion from showers with no hodoscope hits, a shower was required to have overlapping peaks in both dimensions before any peaks were assigned to it. A list of hodoscope peaks that did not overlap the showers was also kept. Note that not only could more than one hodoscope peak in each dimension overlap a shower, but a single hodoscope peak could overlap more than one shower. This was unrealistic, since a hodoscope peak should have represented just one photon, which could not be in two showers at once. Difficulties such as these, which occurred only in events with a large number of photons on an arm, were solved by a procedure described in Appendix A. The principal reactions that this affected were those with π^0 's in the final state, since π^0 's often produced two photons close together.

4.1.4 Calorimeter Processing

The calorimeter counters were not grouped into clusters or peaks but rather were treated individually without reference to one another. A calorimeter counter was considered to be hit if it had a TOF within the window of -10 to 20 ns and the latch bit was set. The position of each hit calorimeter counter was compared with the windows of all the showers on that arm. If the counter overlapped just one shower, its pulse height was assigned to that shower. If the calorimeter counter overlapped more than one shower, its pulse height was distributed

PULSE HEIGHT OF COUNTER



HODOSCOPE COUNTER

Figure 29 Example of Adjacent Hodoscope Peaks

among these showers in proportion to the hodoscope energies of the showers. Hit calorimeter counters that did not overlap any showers were used to make cuts on the event quality, as will be described in Section 4.5.2.

4.2 Determining the Photon Energies

The detector provided measurements of the energy of an electromagnetic shower at four locations in its development, and these had to be combined to determine the photon energy. The simplest way to do this is to use four constant weights, one for each layer, and form the sum of the energies deposited in the layers. This method was used to form a first approximation to the photon energy. The four parameters were chosen by MINUIT³⁵, a multivariable minimization program, which found the best simultaneous fit to the energy of electron showers.

The first approximation to the photon energy worked well, but the detector appeared to have a nonlinearity in the energy response of a few percent. To correct for this, as well as to determine the energy scale of the detector using photons rather than electrons, a second approximation to the photon energy was generated, in which the four weighting factors were each parameterized as a function of the energy measured in the first approximation. The parameters were chosen by the MINUIT³⁵ program to make the best simultaneous fit to the masses of 5, 8, and 10 GeV/c η s and of π^0 s with energies between 2 and 5 GeV produced as decay products of 5 GeV ω s. The η s were collected during the single arm runs³⁶, and the ω s were collected during one of the lower energy runs.

The composition of the photon sample was chosen to form as uniform a sampling of photon energies as possible between the energies of .8 and 8 GeV. The weights were parameterized as a linear function of the energy, since no improvement was observed with more complex solutions,

³⁵ F. James, M. Roos, Computer Physics Communications 10, p343 (1975).

³⁶ See Section 2.7.2 for a description of the single arm runs.

and were constrained to be constant for photon energies in excess of 8 GeV, since this range of photon energies was untestable. The calorimeter and front lead glass wall weighting factors were constrained to be constant as a function of the photon energy. The final weighting factors are shown in Figure 30 as a function of energy. The results of this fit were consistent with a fractional energy resolution of $13.7\%/\sqrt{E}$, where E is measured in GeV.

4.3 Distinguishing Between One- and Two-Photon Showers

Up to this point the goal of the pattern recognition was to cluster all detector information that was even remotely related into a single shower. If an error in assignment was made, we wanted to combine two separate photons into one shower. We did this because of our confidence in the hodoscope's ability to distinguish between one- and two-photon showers. This section will describe how the hodoscope information was used to determine whether a shower was caused by one or two incident photons. Only the case in which both photons from the π^0 converted before striking the hodoscope plane will be discussed. The case in which one of the photons failed to convert before the hodoscope plane is considered in Section 4.6.1.

If a shower contained two or more hodoscope peaks in either dimension, it was likely that these were caused by the two photons from a π^0 decay. A useful check would be to calculate the invariant mass of the two-photon hypothesis, but we knew only the sum of the photon energies. For a single shower to have contained two photons from π^0 decay, the opening angle must have been near minimum, for which the energies were equal. To estimate the mass we assumed that both photons shared half the total energy of the shower and calculated the resulting invariant mass. This approximation, which was a good one for the π^0 's in our detector, always led to a calculated mass higher than the real mass. We called this quantity, which was measured using the maximum opening angle found between any of the hodoscope peaks assigned to the shower, the "maximum mass".

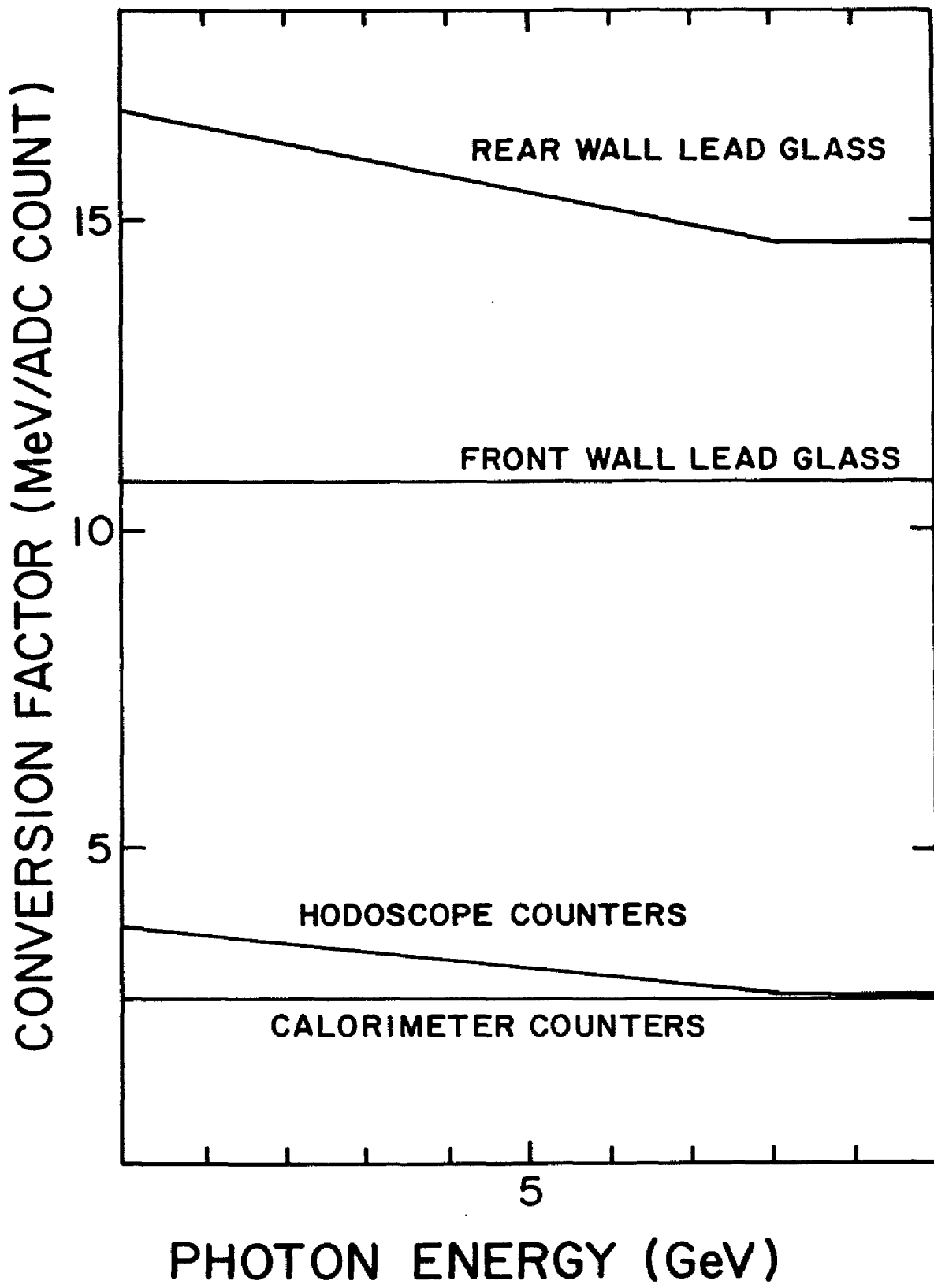


Figure 30 Energy Response of Detector Layers vs. Incident Photon Energy

The maximum mass is shown in Figure 31 for four different momenta of electrons³⁷ and in Figure 32 for all showers in the 13 GeV/c data. If a shower had a maximum mass of less than 100 MeV, it was called a single photon regardless of any other hodoscope information. Showers with maximum mass greater than 100 MeV would most likely be called a π^0 , but in some cases they could have been one photon of a separated π^0 pair in which both sets of hodoscope peaks overlapped each shower. Such difficulties were resolved by the procedure described in Appendix A.

4.4 Measuring the Effectiveness of the Cuts

Whenever several cuts are made to reduce a background contamination, there is a difficult task involved in choosing the proper settings for the cuts. What matters is usually not the total number of background or true signal events vetoed by the cut, but rather the number of these events passing all the other cuts but vetoed by the cut under test. The adjustment of cuts is therefore an iterative process, since whenever any cut is changed, the effectiveness of all the other cuts changes with it.

To know whether a cut is good or bad it is necessary to know both the efficiency and background levels as a function of the cut. If an event of interest hits the detector within the fiducial volume, the efficiency is simply defined as the probability that the event is correctly identified as a good event passing all the cuts. I define the background level as the number of background events divided by the efficiency. If, as a cut is applied, the efficiency for detecting the reaction of interest falls by the same fraction as the background level, the statistical significance of any small signal on a large background remains constant. A good cut therefore lowers the background levels by a larger fraction than the efficiency. Throughout this chapter the terms efficiency and background will refer to that

³⁷ See Section 2.7.1 for a discussion of the electron runs.

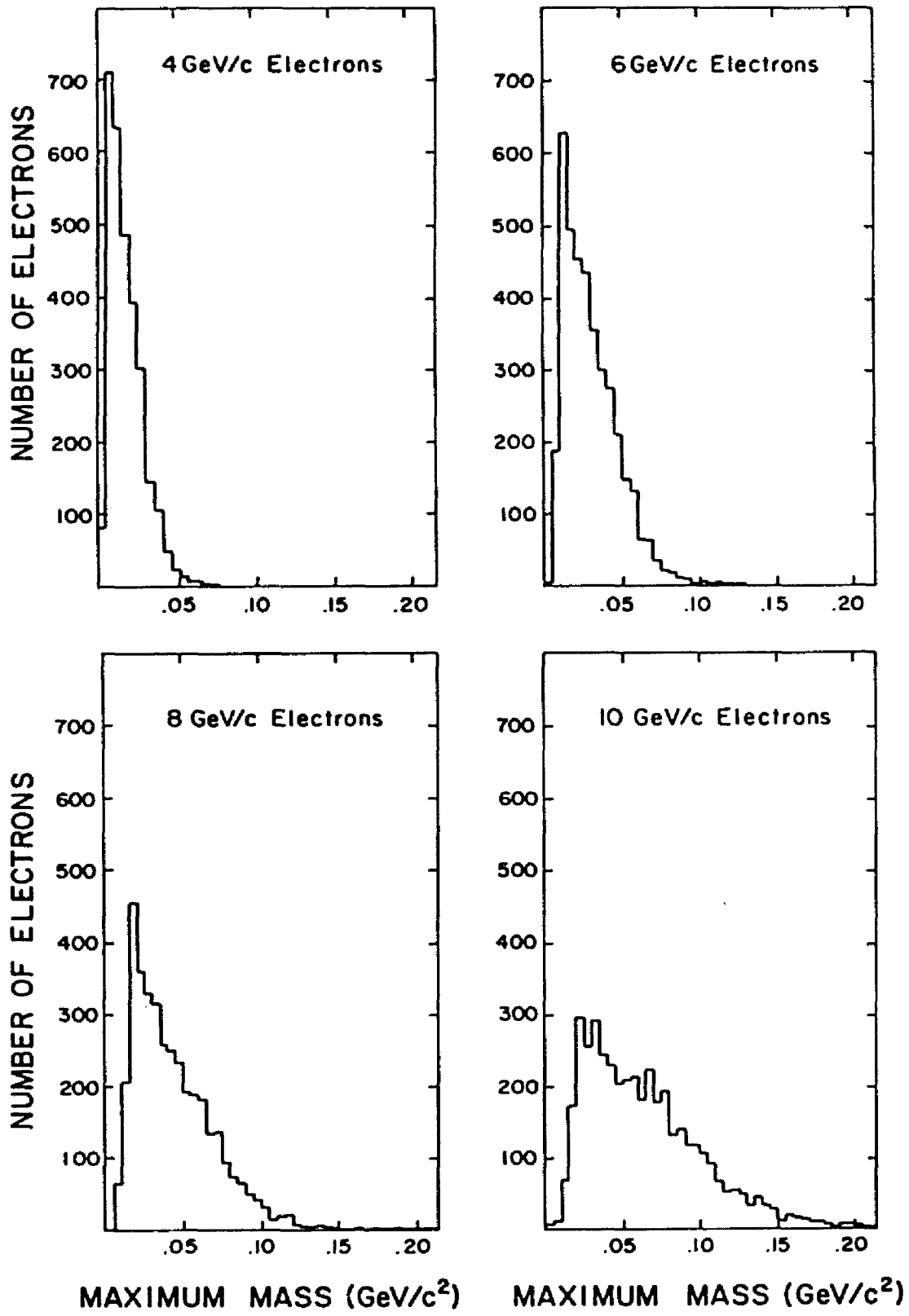


Figure 31 Maximum Mass of Shower as Measured for Electrons

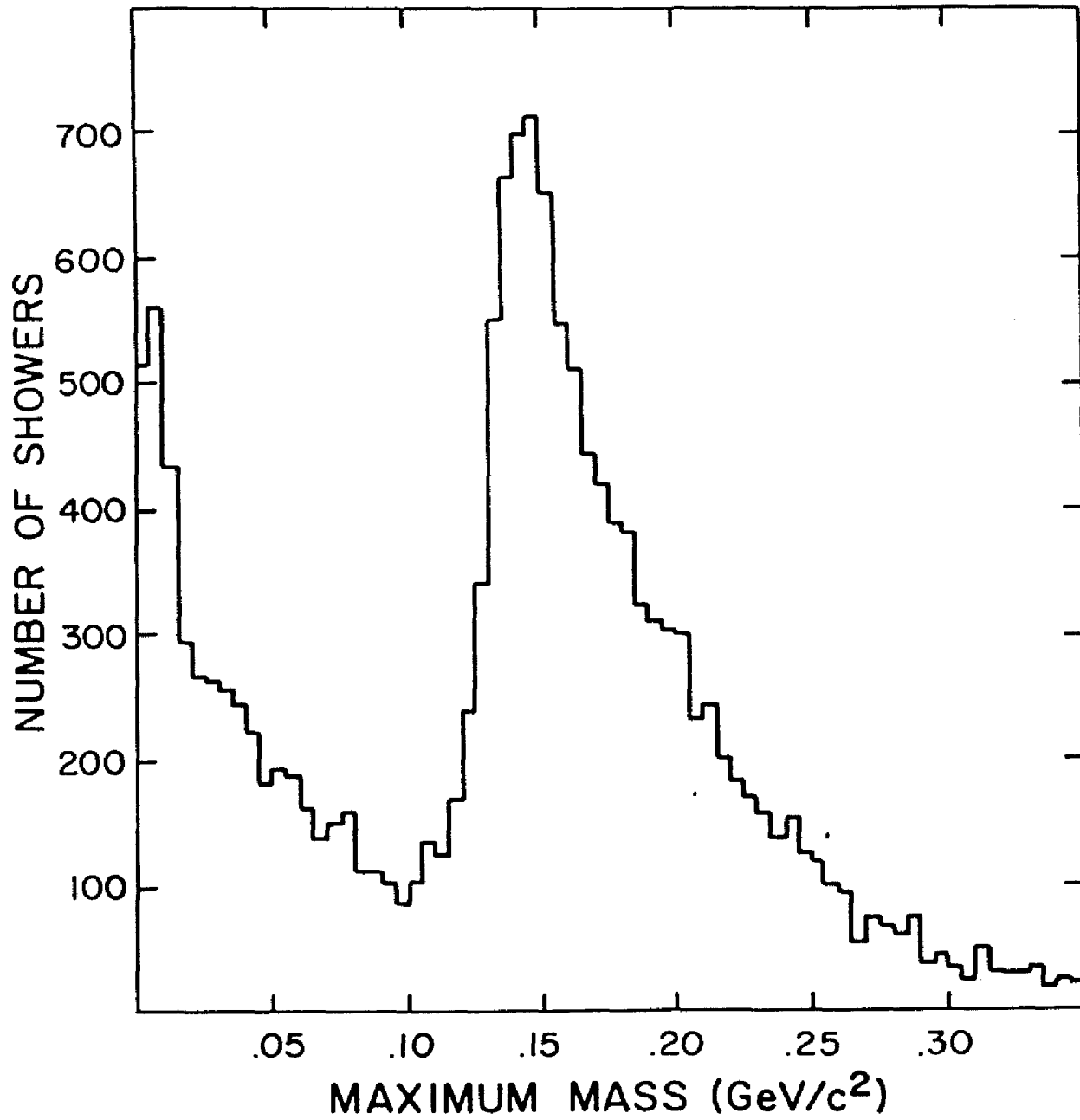


Figure 32 Maximum Mass for All Showers in 13 GeV/c Data

anticipated in the presence of any real $\gamma\gamma$ events, unless otherwise specified.

4.4.1 Measuring Effects of Cuts on Event Quality

We used several different methods to measure the efficiency and background levels, depending on the nature of the cut. The most sensitive and controversial cuts were those dealing with the presence of extra hits in the vetoes and in detector elements not assigned to showers. It was important to measure the effects of such cuts under the same conditions under which the data were taken, since there was a large amount of accidental vetoing at high beam intensities by hits from other interactions. We did not, however, have a large pure $\gamma\gamma$ signal in the 13 GeV/c data sample to tune on. The only events in the main data sample that we were sure were relatively background free were the $\pi^0\pi^0$ events. We subjected these events to the same cuts as used for the $\gamma\gamma$ sample and used the number of surviving events to estimate the efficiency of any possible $\gamma\gamma$ signal. In doing this we assumed that any potential $\gamma\gamma$ event suffered the same losses as the $\pi^0\pi^0$ events. We believe this was a good assumption simply because the area taken by a π^0 or single photon shower in the detector was very small compared with the total area available to detect additional photons.

4.4.2 Measuring the Background Level

In order to measure the background level it is sufficient to measure the number of $\gamma\gamma$ events, since essentially all those events were background from the $\pi^0\pi^0$ events. In our experiment, however, we wanted to adjust the cuts before analyzing all the data, so we predicted the $\gamma\gamma$ background on the basis of the number of $\pi^0\gamma$ events obtained in a small test sample. To do this we assumed that the probability that a π^0 would be detected as a single photon was the same for either or both π^0 's of a $\pi^0\pi^0$ event. This is shown to be a good approximation in Section 6.1. The expected background level is then:

$$\gamma\gamma/\pi\pi = (.5*(\pi\gamma/\pi\pi))^2$$

4.5 Event Selection - Cuts for Detecting Soft Photons

4.5.1 Veto Counter Cuts

The photon veto counters were the primary defense against wide-angle low-energy photons. All the veto counters had at least one updating discriminator with latch and TDC. Appendix B describes the tests performed to determine the best offline cuts for the veto counters. The best cuts, as determined by these tests, are summarized in Table 7. The downstream photon veto counters were the most important. The cuts based on these counters reduced the background by approximately 60%, with only a 9% loss in efficiency. This result does not fully represent the usefulness of these counters, since events with large pulse heights in the vetoes had already been eliminated by the hardware trigger. The target box photon vetoes reduced both the background and efficiency by about 7%. The charged particle vetoes, which should have been redundant with the hardware trigger, had very little effect.

TABLE 7

Veto Cut Requirements

Charged Particle Vetoes:	-6 < TOF < 6 ns
Target Box Photon Vetoes:	-2 < TOF < 1 ns
Downstream Photon Vetoes:	-4 < TOF < 4 ns
or:	(TOF < -25 ns and latch hit)

4.5.2 Extra Calorimeter Counter Cuts

A large fraction of the solid angle surrounding the target was filled by the detector. Low energy photons that hit the detector

could fail to penetrate deeply enough to be identified as a shower. These photons were detected in either the calorimeter counters or the hodoscope as extra hits, which did not overlap a shower. Such a hit had to have a TOF within the window of -10 to 10 ns to be considered real, but essentially all such hits appear to have been in-time. Figure 33 shows the expected efficiency and background levels as a function of a cut on the pulse height of extra calorimeter counters. We chose to cut at 7 ADC counts. With such a cut the background levels dropped by approximately 34% with only a 3% loss in efficiency.

4.5.3 Extra Hodoscope Peaks

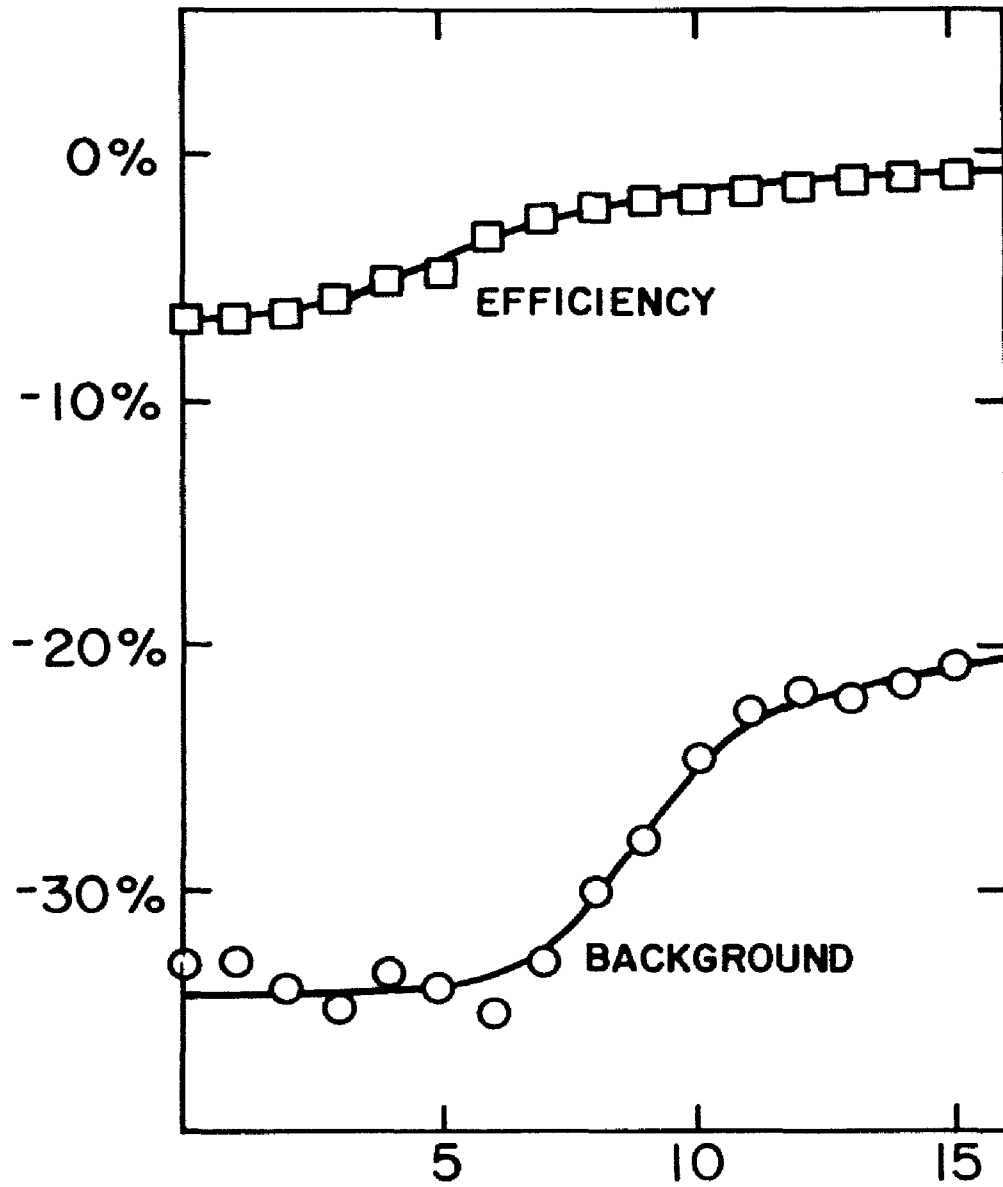
There were two basic types of extra hodoscope peaks, those with only one struck counter and those with more. A very low-energy photon shower would most likely be very small, hitting only one hodoscope counter in each layer, while high-energy showers would hit many counters. Appendix C describes the tests performed to determine the effectiveness of eliminating events with extra single counter hodoscope peaks. Basically, the best cuts eliminated events containing an extra hodoscope peak with a pulse height greater than 25 ADC counts. This corresponded roughly to 5 minimum ionizing particles.

4.5.4 Extra Hits in the Front Lead Glass Wall

If an electromagnetic shower penetrated to the front lead glass wall but was below threshold in both the rear lead glass wall and the hodoscope, its four-vector could not be calculated. These showers had very low energy and could be ignored without any change in the event kinematics, but their presence may have indicated the existence of an additional photon.

Appendix D describes the tests conducted to determine if these showers should be ignored or considered indications of an extra photon in the event. The results indicated that if such a shower had an overlapping calorimeter hit, it was sure to be an additional photon. The elimination of events with such showers reduced the background

EFFICIENCY AND BACKGROUND LEVELS



PULSE HEIGHT
THRESHOLD (ADC COUNTS)

Figure 33 Efficiency and Background vs. Calorimeter Pulse Height Cut

levels by 20% with only a 6% loss in efficiency. If the shower did not have an overlapping calorimeter hit, there was insufficient improvement in the background levels to warrant the loss in efficiency. Such showers were simply ignored.

4.5.5 Extra Hits in the Rear Lead Glass Wall

About 8% of the data events contained showers with no energy deposited in the front lead glass wall or the hodoscope. Such showers may have had overlapping calorimeter counters. Appendix E describes the studies that were performed to determine the effectiveness of eliminating events with such a shower. The results indicated that a modest increase of about 2% in the statistical significance of a $\gamma\gamma$ signal could have been obtained by cutting on the presence of such showers, but no cuts were made. These showers were ignored by the analysis program.

4.6 Event Selection - Identifying Symmetrically Decaying π^0 's

There were two ways in which a high-energy π^0 decaying symmetrically might have been misidentified as a single photon. The first occurred when one of the photons did not convert until after the hodoscope plane, causing only one shower to be detected by the hodoscope. The second occurred when the two photons lined up in the vertical dimension, as is described below.

4.6.1 Hodoscope - Rear Wall Position Matching Cut

A π^0 with one photon failing to convert before the hodoscope plane, and for which the two showers were not resolved by the rear lead glass wall matrix, could be identified by two methods. Such a shower appeared to have a larger transverse diameter than a shower caused by a single photon, and a cut based on the second moment of the energy distribution of a shower was effective in reducing such backgrounds. Unfortunately, such a cut eliminated a substantial fraction of the true single photon showers.

A better way of eliminating π^0 's with one photon failing to convert before the hodoscope plane was to match the shower position in the rear wall to that measured with the hodoscope. A true photon should match well, while a π^0 should have a large error, since one photon escaped detection in the hodoscope.

We formed the χ^2 of the match in position using the anticipated error in position in the two layers. This quantity is shown in Figure 34 for electrons of four different momenta. Figure 35 shows the expected $\pi^0 \gamma$ background as a function of this cut, as measured in the 13 GeV/c data. Most of the improvement was clearly made by cutting on a χ^2 so high as to be off scale. We chose a cut at a χ^2 of 15, which was certainly loose enough. The drop in efficiency at low χ^2 in Figure 35 occurred at the same location as the drop in the electron efficiency, which is calculated for 6 GeV electrons and shown in the same figure. This adds support to the theory that most of the surviving $\pi^0 \gamma$ events were events in which the missing photon was a wide-angle low-energy photon.

The effectiveness of this cut was easily determined by reanalyzing showers already determined to be π^0 's but removing one pair of hodoscope peaks to simulate an unconverted photon. Roughly 90% of such showers failed the χ^2 cut. Since only 6% of the π^0 's produce a photon that fails to convert before the hodoscope plane, it is clear that only .5% of the π^0 's feed down into the γ sample by such a mechanism.

4.6.2 Extra Single Hodoscope Peak Cut

If a π^0 decayed with the two photons lined up in the vertical dimension, as shown in Figure 36, it may have fed down into the gamma sample if one photon failed to penetrate to the rear lead glass wall. Events with such geometry were very easy to detect by the presence of an extra hodoscope peak with large pulse height in the plane with horizontal counters. Appendix C describes the tests performed to determine the effectiveness of eliminating events with such hodoscope

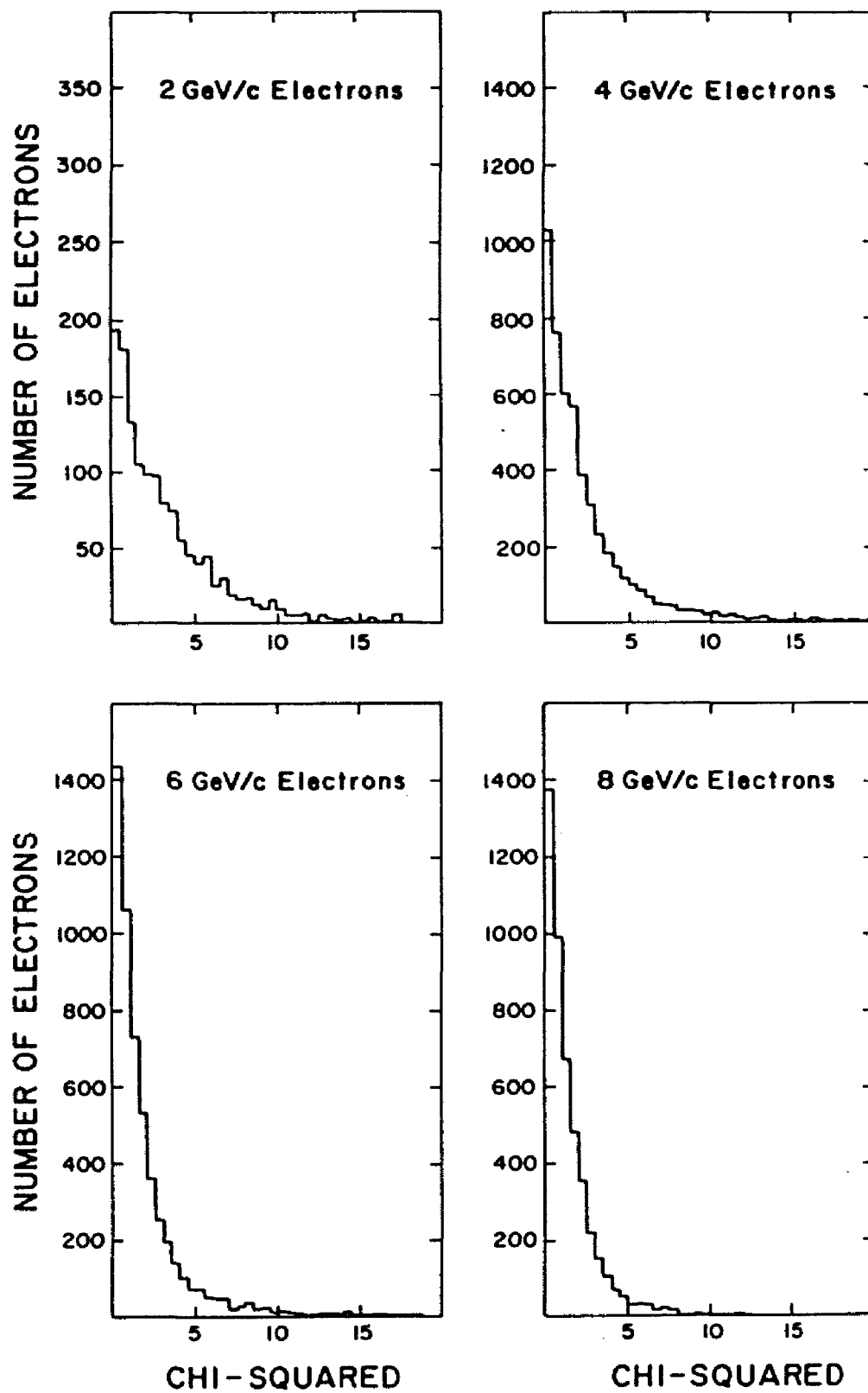


Figure 34 Position Matching χ^2 for Electrons

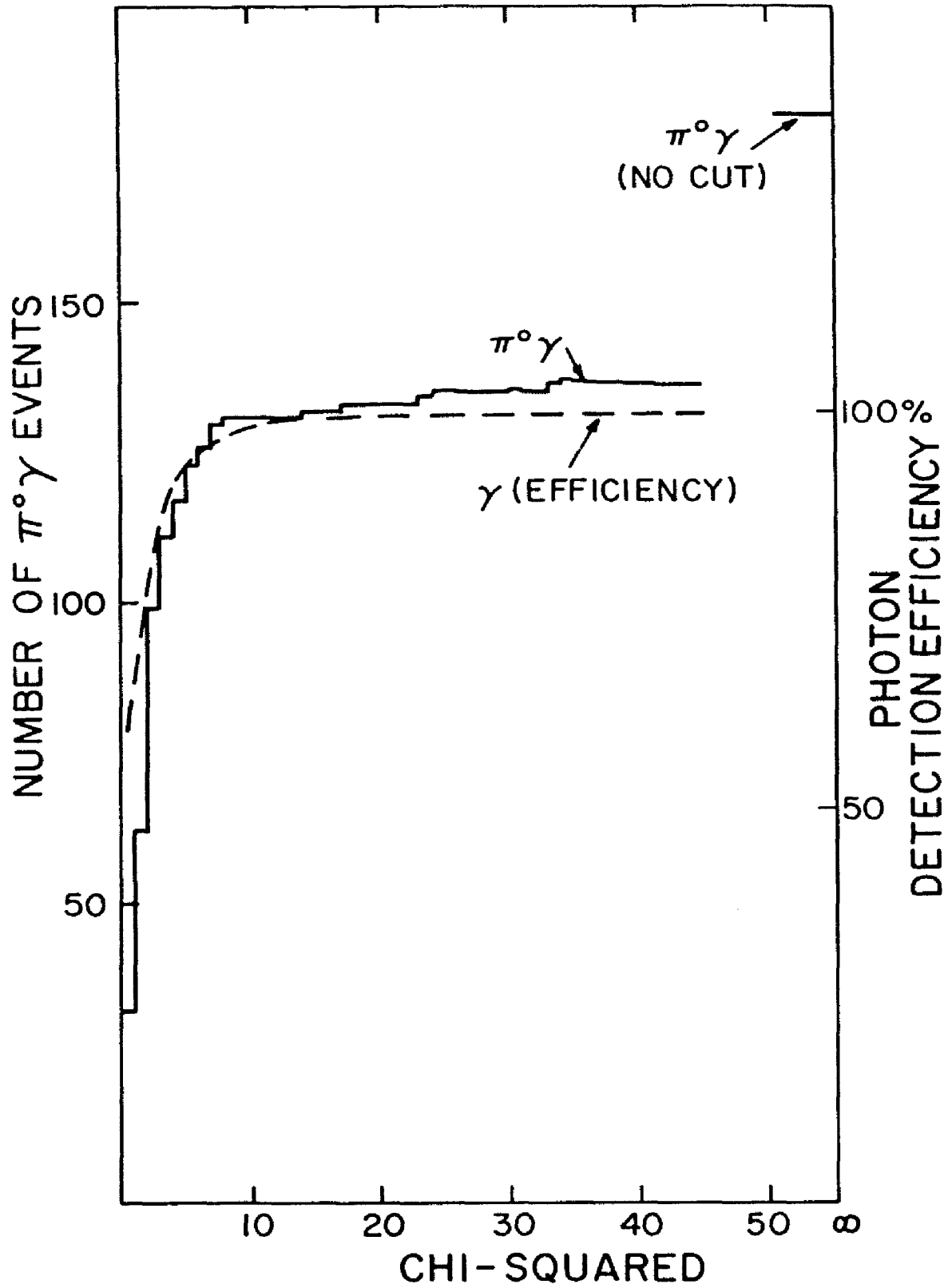


Figure 35 Measured Background and Expected Efficiency vs. Position Matching χ^2 Cut

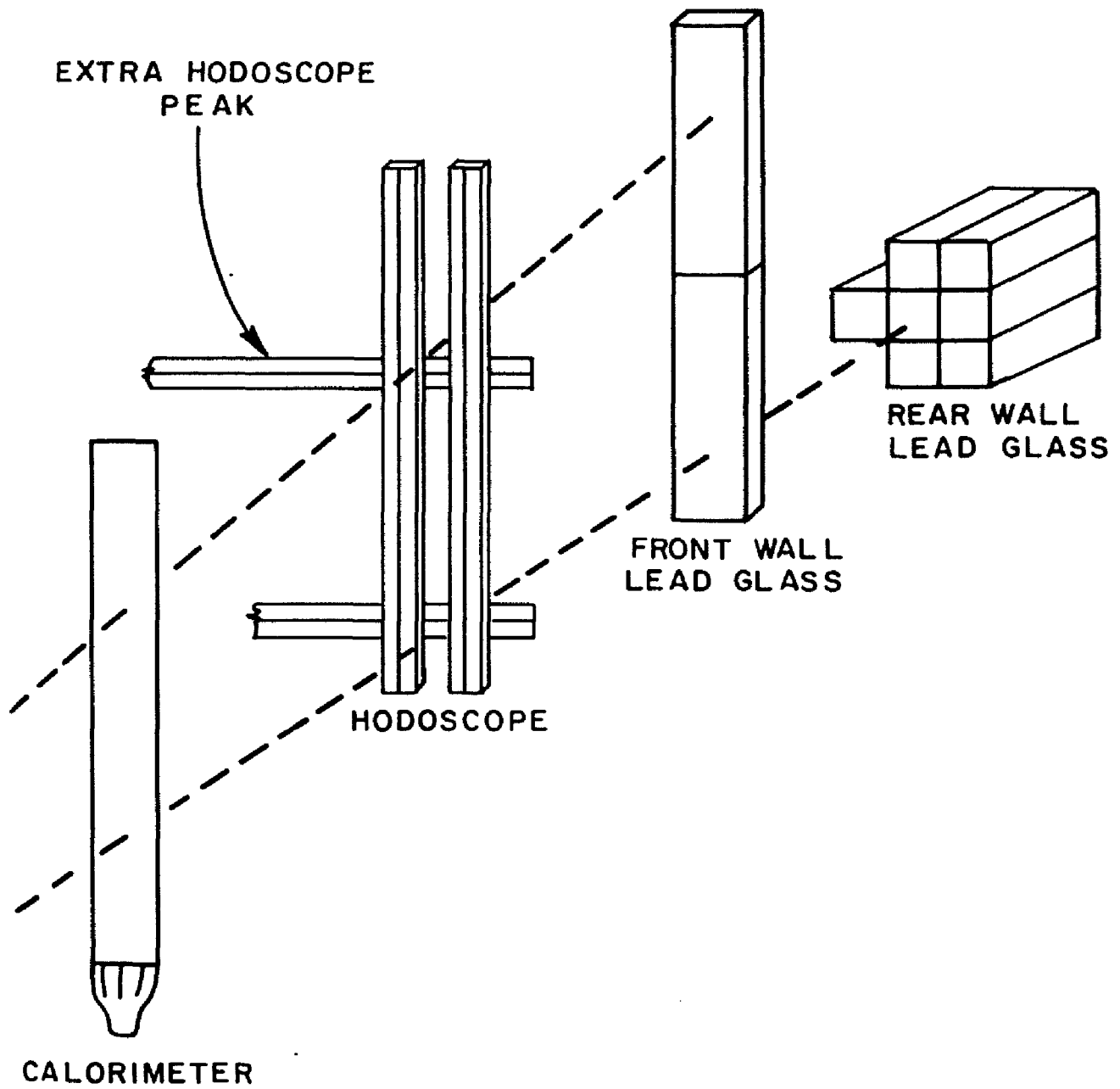


Figure 36 Background Generating Mechanism Caused by Front Lead Glass Wall Geometry

peaks. Essentially all such background events were eliminated with a cut placed at 24 ADC counts, resulting in a reduction of the background level by 16.5% with only a 1.5% loss in efficiency.

4.7 Event Selection - Elimination of Events with Missing Energy

In some rare cases a photon may have escaped through the beam hole in the veto counters or may have struck a momentarily dead veto counter. If the photon carried away a large amount of energy, its presence could be determined by cuts on the event kinematics, such as the total energy. We chose, rather, to select events whose missing mass was close to that of a neutron. An event with an extra unobserved particle should have had a larger missing mass than that of a neutron. Figure 37 shows the square of the missing mass for events that passed all the other cuts necessary to qualify for the $\gamma\gamma$ sample. There is a clear background, which we removed by requiring the square of the missing mass to be within the limits of -2 to 1.9 $(\text{GeV}/c^2)^2$.

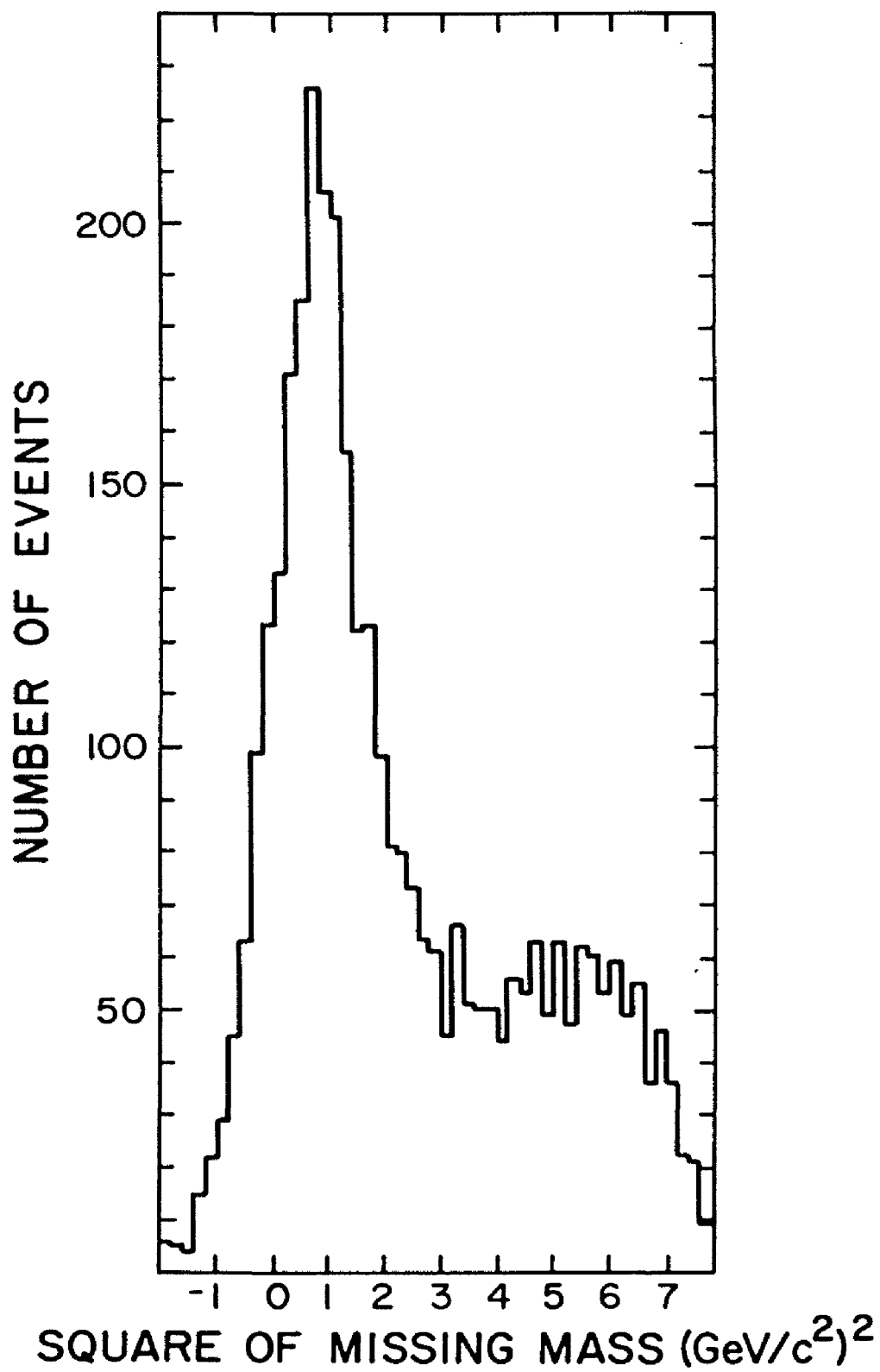


Figure 37 Square of Missing Mass for $\gamma\gamma$ Candidates in 13 GeV/c Run

Chapter V

MEASUREMENTS OF THE CROSS SECTIONS OF KNOWN RESONANCES

With our detector set up for the 13 GeV/c running the acceptance of the apparatus dropped rapidly below a mass of 1.8 GeV, as shown in Figure 38. To test our experiment, and to prove that it was working, we wanted to measure the cross sections of some well-established resonances, but there are no known resonances above 1.8 GeV that we could observe. In order to observe lower mass resonances we reduced the beam energy, which allowed these objects to decay with wider opening angles, thereby hitting the detector arms. In this manner we measured the cross sections of the η , η' , and the ω for 5 GeV/c beam momentum, and the η' at 8.5 GeV/c beam momentum. This chapter will describe the procedures used to determine those cross sections.

5.1 Calculation of Cross Sections

There are a large number of factors that entered into the calculation of the cross sections. Each reaction had a different set of small corrections, the most important of which will be described below.

5.1.1 Measuring the Geometrical Efficiency of the Apparatus - The Monte Carlo

The largest correction necessary to calculate a cross section was the geometrical acceptance, which was determined by a Monte Carlo simulation program. Events were generated in which sets of photon energy-momentum four-vectors were chosen to meet predetermined kinematic constraints, such as mass, momentum transfer, and decay angle in the rest frame. Other kinematic variables, such as the azimuthal angle and Fermi motion of the nucleus, were chosen at random. The incident beam momentum of each event was allowed to vary

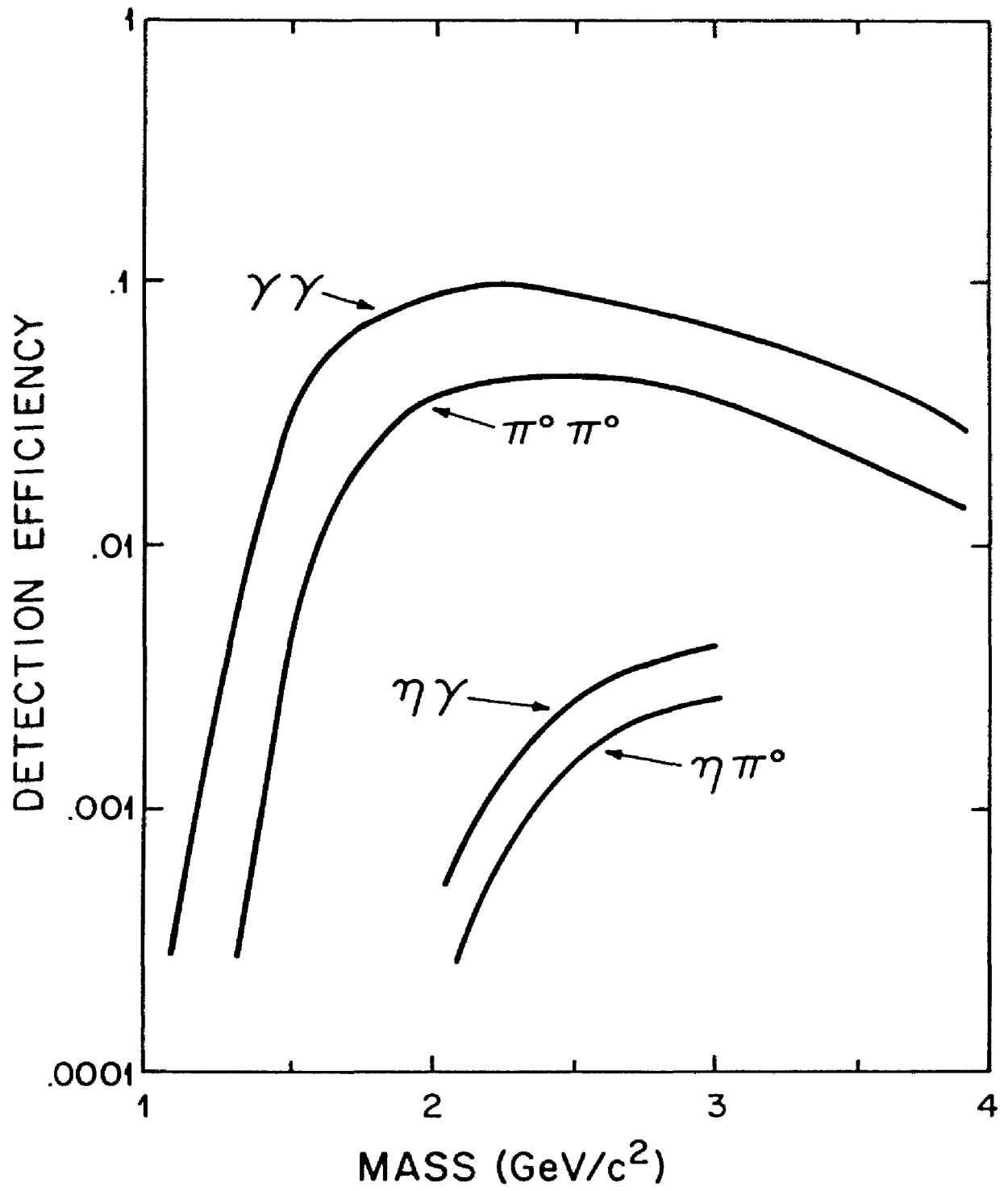
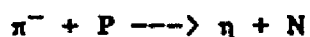


Figure 38 Acceptance vs. Mass for 13 GeV/c Beam Momentum

within the expected momentum bite of the beam, $\pm 1/2\%$, and was corrected for dE/dx losses in the target. The lateral location of the interaction within the target was chosen to allow for the expected beam profile, and the longitudinal location was chosen to allow for attenuation of the beam intensity within the target. In addition, if the reaction involved intermediate particles, such as π^0 's, the decay angles of the photons were chosen to be isotropic in the π^0 rest frame.

The fraction of the generated events captured by the apparatus was used to determine the acceptance. Events were lost if a photon missed the detector or if it converted within the target scintillator, thus vetoing the event. Random fluctuations that simulated the finite energy and position resolution of the detector were added to the four-vectors, which were then reconstructed using the same constrained fitting program that was used to reconstruct the data events. This fitting program adjusted the energies of the detected photons to allow the missing mass from the reaction to be that of a neutron. In this manner the detector's ability to reconstruct the kinematic quantities of interest, mass, $\cos(\theta)$, and t , was determined.

To measure a total cross section it was necessary to know the distributions in the kinematic variables and extrapolate our measurement to the full kinematic range. For most of the cross sections presented here this was done by generating the Monte Carlo events according to published distributions in the kinematic variables. This mode is acceptable for checking cross sections of reactions for which the production and decay kinematics are accurately known. The following reactions meet this requirement very well:



Our apparatus had good acceptance only at low $\cos(\theta)$, so the total cross sections of reactions of unknown spin alignment could not be

determined by our measurements alone. For some of the cross sections presented here this uncertainty in the expected kinematic distributions dominated the systematic errors.

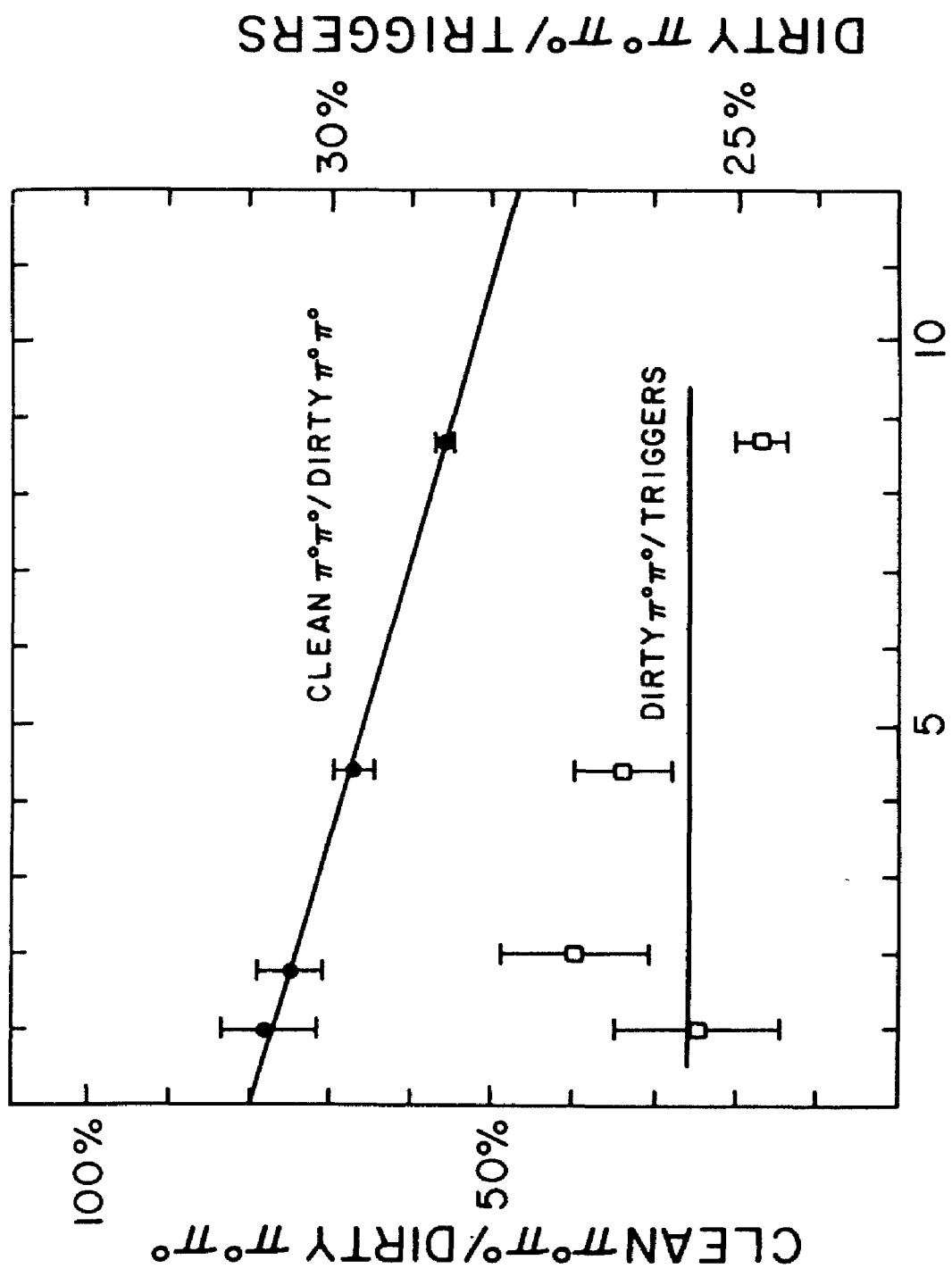
5.1.2 Rate Dependence to Acceptance After All Cuts

For the purpose of measuring the net loss in efficiency caused by the event selection cuts a second category of $\pi^0 \pi^0$ event was formed, the "dirty $\pi^0 \pi^0$ ". These events had to have two identified π^0 's within the fiducial volume, but no other cuts were made, and extra showers could be present. The normal $\pi^0 \pi^0$ events were a subset of the dirty $\pi^0 \pi^0$ events. As is shown in Figure 39, the fraction of data events labeled dirty $\pi^0 \pi^0$ was independent of beam intensity, while the fraction of good $\pi^0 \pi^0$ events fell from 80% at zero intensity to 58% at 8 MHz. This indicates a 34% loss in efficiency at 8 MHz.

To calculate the efficiency for $\gamma \gamma$ events we assumed that the rate dependence of the losses for $\gamma \gamma$ events was the same as for $\pi^0 \pi^0$ events. One indication that this was true was that the ratio of $\pi^0 \gamma$ events to $\pi^0 \pi^0$ events as a function of beam intensity was constant, as shown in Figure 40. We thus expect that most of the photons in the $\pi^0 \gamma$ events were true photons from π^0 decay, with the other photon undetected.

The fraction of events vetoed by the three types of veto counters as a function of beam intensity is shown in Figure 41. The largest effect was shown by the downstream photon vetoes, which vetoed 20% of the data events at 8 MHz compared with 5% at zero intensity. The target box photon vetoes eliminated a constant 11% of the data events, and the charged particle vetoes showed a small rise up to about 5%. The net rate dependence of the veto counters was about 14%. The remaining 20% of the total rate dependence was therefore caused by the other event selection cuts.

In addition to rate dependent losses, there was an intrinsic loss of otherwise good events, independent of beam intensity, caused by



BEAM INTENSITY (MHZ)

Figure 39 Ratio of Clean to Dirty $\pi^0 \pi^0$ vs. Beam Intensity

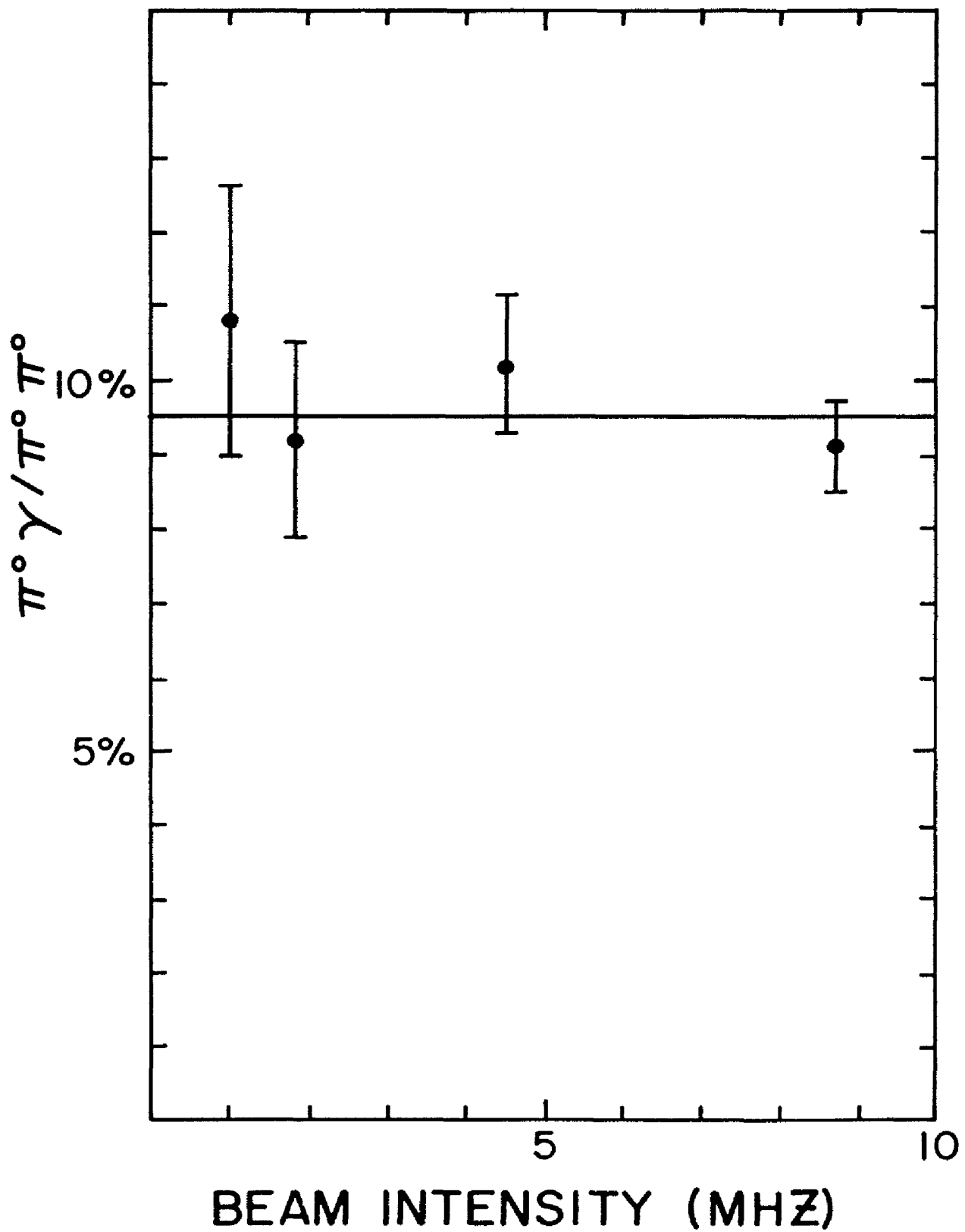


Figure 40 Background Level as Function of Beam Intensity

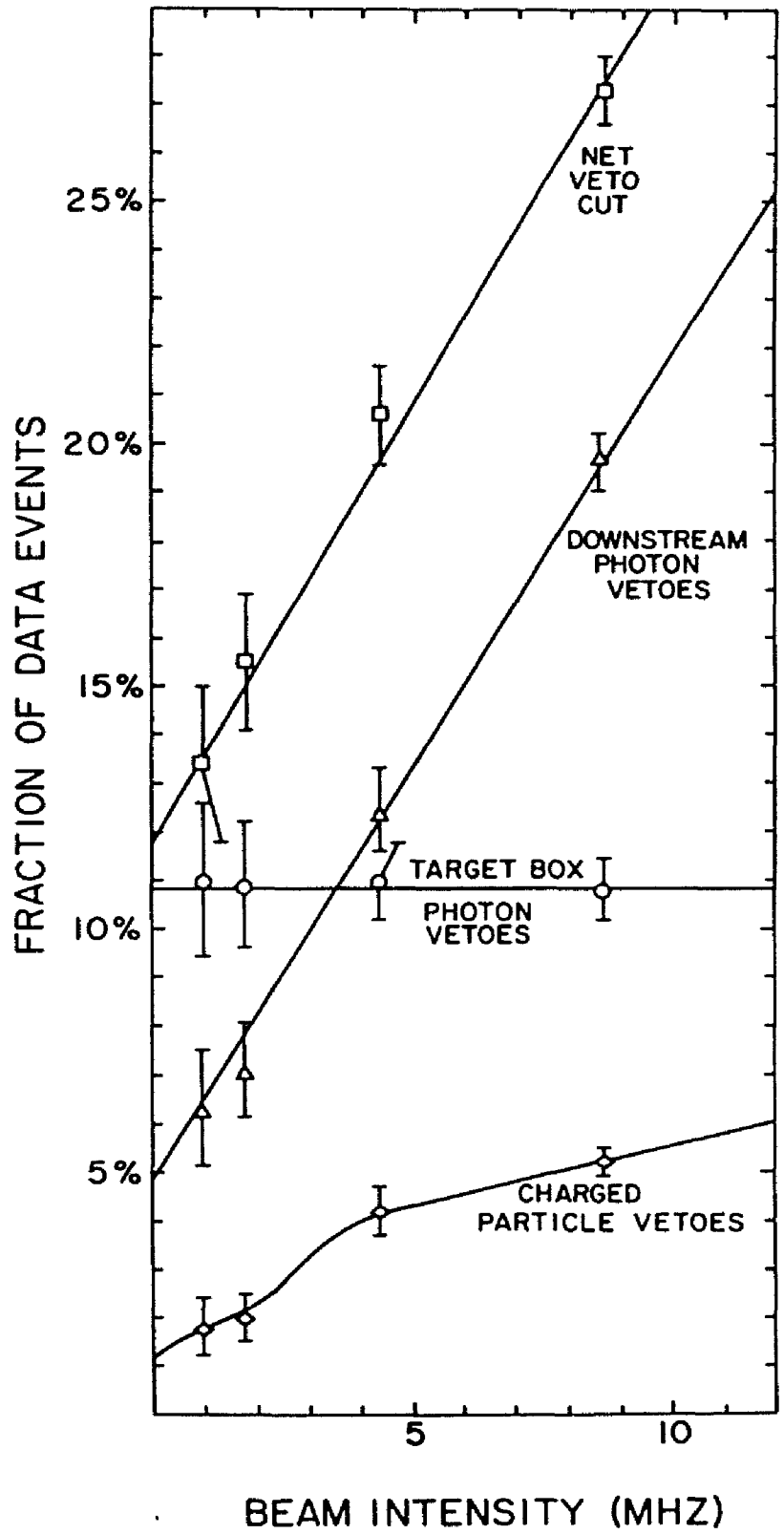


Figure 41 Fraction of Events Vetoed by Veto Counter Cuts vs. Beam Intensity

fluctuations in the electromagnetic shower being interpreted as signs of an additional photon. We estimated the photon detection efficiency by subjecting electrons³⁸ to the same cuts as $\gamma\gamma$ events and determining the number of surviving events. On the basis of the results, shown in Tables 8 through 12, we made a 20% correction to the cross section. In doing this we made the rather good assumption that the electromagnetic shower produced by an electron in our detector was indistinguishable from that of a photon.

We did not have a correspondingly pure sample of π^0 's to use in measuring the π^0 detection efficiency, but we did not need to make very tight cuts to identify $\pi^0\pi^0$ events. Figure 39 indicates that roughly 20% of the dirty $\pi^0\pi^0$ events were lost at low intensity, and 60% of these were vetoed by the veto counters. We assumed that all events that were vetoed by the veto counters at low rates were true background events, i.e., they were accompanied by another particle. This implies that roughly 8% of the true $\pi^0\pi^0$ events failed the event selection cuts at low intensity.

5.1.3 Effective Number of Target Nucleons

It is important to remember that our target was not pure hydrogen, but rather a mixture of hydrogen and carbon. This complicates matters tremendously, since data on the A dependence of cross sections are scarce, and the theoretical understanding of these effects is very crude. All cross sections presented in this thesis will be normalized to that expected from hydrogen by assuming that, due to shadowing effects, each carbon nucleus contains 3.3 effective protons rather than 6. This result has been confirmed³⁹ for η and π^0 production using carbon targets. In addition, a correction was made to allow for attenuation of the beam intensity as it passed through the $1/3$ interaction length target. We did not include any corrections for vetoing due to delta rays produced by the beam particle before it

³⁸ See Section 2.7.1 for a description of the electron runs.

³⁹ V. N. Bolotov, et al., Nuc. Phys. B85, p158 (1975).

TABLE 8

Electron Cut Summary for 2 GeV/c Electrons

Total number of events called electrons		1630
Events lost due to edge cuts	6	1624
Events lost due to lone front wall shower cut	29	1595
Events lost due to lone calorimeter hit cut	16	1579
Events lost due to lone hodoscope peak cut	13	1566
Events lost due to being called π^0 's	11	1555
Events lost due to presence of extra shower	26	1539
Events lost due to arm energy cut	17	1522
Events lost due to position matching cut	77	1445
Events lost due to 2 clusters in rear wall	2	1440
Total number of electrons passing all cuts		1440

TABLE 9

Electron Cut Summary for 4 GeV/c Electrons

Total number of events called electrons		6163
Events lost due to edge cuts	32	6131
Events lost due to lone front wall shower cut	52	6079
Events lost due to lone calorimeter hit cut	112	5967
Events lost due to lone hodoscope peak cut	88	5879
Events lost due to being called π^0 's	75	5804
Events lost due to presence of extra shower	28	5776
Events lost due to position matching cut	183	5593
Events lost due to 2 clusters in rear wall	17	5562
Total number of electrons passing all cuts		5562

TABLE 10

Electron Cut Summary for 6 GeV/c Electrons

Total number of events called electrons		6990
Events lost due to edge cuts	51	6939
Events lost due to lone front wall shower cut	51	6888
Events lost due to lone calorimeter hit cut	134	6754
Events lost due to lone hodoscope peak cut	155	6599
Events lost due to being called π^0 's	88	6511
Events lost due to presence of extra shower	32	6479
Events lost due to position matching cut	102	6377
Events lost due to maximum mass cut	3	6374
Events lost due to lack of hodoscope peaks	10	6364
Events lost due to 2 clusters in rear wall	19	6345
Total number of electrons passing all cuts		6345

TABLE 11

Electron Cut Summary for 8 GeV/c Electrons

Total number of events called electrons		6163
Events lost due to edge cuts	49	6114
Events lost due to lone front wall shower cut	30	6084
Events lost due to lone calorimeter hit cut	164	5920
Events lost due to lone hodoscope peak cut	127	5793
Events lost due to being called π^0 's	124	5669
Events lost due to presence of extra shower	28	5641
Events lost due to position matching cut	34	5607
Events lost due to maximum mass cut	35	5572
Events lost due to lack of hodoscope peaks	6	5566
Events lost due to 2 clusters in rear wall	36	5530
Total number of electrons passing all cuts		5530

TABLE 12

Electron Cut Summary for 10 GeV/c Electrons

Total number of events called electrons		5988
Events lost due to edge cuts	75	5913
Events lost due to lone front wall shower cut	34	5879
Events lost due to lone calorimeter hit cut	185	5694
Events lost due to lone hodoscope peak cut	137	5557
Events lost due to being called π^0 's	417	5252
Events lost due to presence of extra shower	167	5085
Events lost due to position matching cut	34	5051
Events lost due to maximum mass cut	173	4878
Events lost due to lack of hodoscope peaks	3	4875
Events lost due to 2 clusters in rear wall	45	4830
Total number of electrons passing all cuts		4830

interacted, or for events lost by being vetoed by the decay products originating from the remains of the carbon nucleus. These effects are expected to be small.

5.1.4 Neutron Self Vetoing

In most cases the neutron produced in the reaction escaped without detection. However, if the neutron was detected, it would appear to have been an additional photon in the event, thereby causing the event to be lost. Monte Carlo studies were performed to estimate the fraction of events lost due to the interactions of the neutron within the veto counters and the detector array. Roughly 7% of the neutrons interacted within the target itself. These interactions did not cause the elimination of the event but may have degraded the mass resolution by confusing the interaction location.

For an event to be lost the neutron must have interacted within the detector element and that interaction must have produced secondary particles capable of being seen by the detector element. Lead glass is a poor neutron detector, since the neutron energy must be high enough to produce π^0 's, which then are seen by their electromagnetic showers. Scintillator is a much better neutron detector, since it is sensitive to the low-energy proton produced by the charge exchange interaction. We used the model of Pollard⁴⁰ to estimate the interaction probability and "visibility factor" for neutrons in lead and plastic scintillator as a function of momentum, and we assumed that the lead glass was incapable of detecting the neutrons. Using the neutron momenta generated by the Monte Carlo, we estimated that overall roughly 12% of the events were lost due to the detection of the neutron in the veto counters and the detector.

⁴⁰ Paul L. Pollard (Ph.D. Thesis, University of California at Berkeley) LBL 5522 (1976).

5.2 Estimates of Systematic Errors

Systematic errors in measuring the cross section could occur as a result of a large number of causes, some of which are listed in Table 13 along with a crude estimate of their relative importance. In most cases the errors in the geometrical efficiency will dominate the systematic errors. A Taylor expansion of the acceptance was made as a function of several input parameters to the Monte Carlo, not all independent of one another. The results of these tests, which are displayed along with the other normalization information in the tables, were used to form a crude measurement of the total uncertainty by adding them in quadrature as if they were independent.

5.3 The Test Run Results

Most of the particles observed in the test runs were in a kinematic region where the acceptance was very sensitive to small changes in the detector geometry, making the measurements of their cross sections very sensitive to small systematic errors. The η' cross section at 5 GeV/c was, however, well suited for measurement by the detector.

5.3.1 Five GeV/c η'

Figure 42 shows the $\gamma\gamma$ mass spectrum, uncorrected by acceptance, obtained in the 5 GeV/c runs. Clear η and η' peaks are evident. A fit to the mass region of .82 to 1.04 GeV with the hypothesis of a linear background plus a gaussian peak yielded a χ^2 of 7.3 for 6 degrees of freedom. This fit yielded 240 η' events. Since at low mass the background from ω production, with one low-energy photon undetected, is expected to dominate the background, I made another fit to the mass region of .74 to 1.04 GeV with the hypothesis of a gaussian centered near .783 GeV, a quadratic background, and another gaussian centered near the η' . This fit yielded a χ^2 of 10.3 for 6 degrees of freedom, with 347 η' events, and is used for the calculation of the cross section.

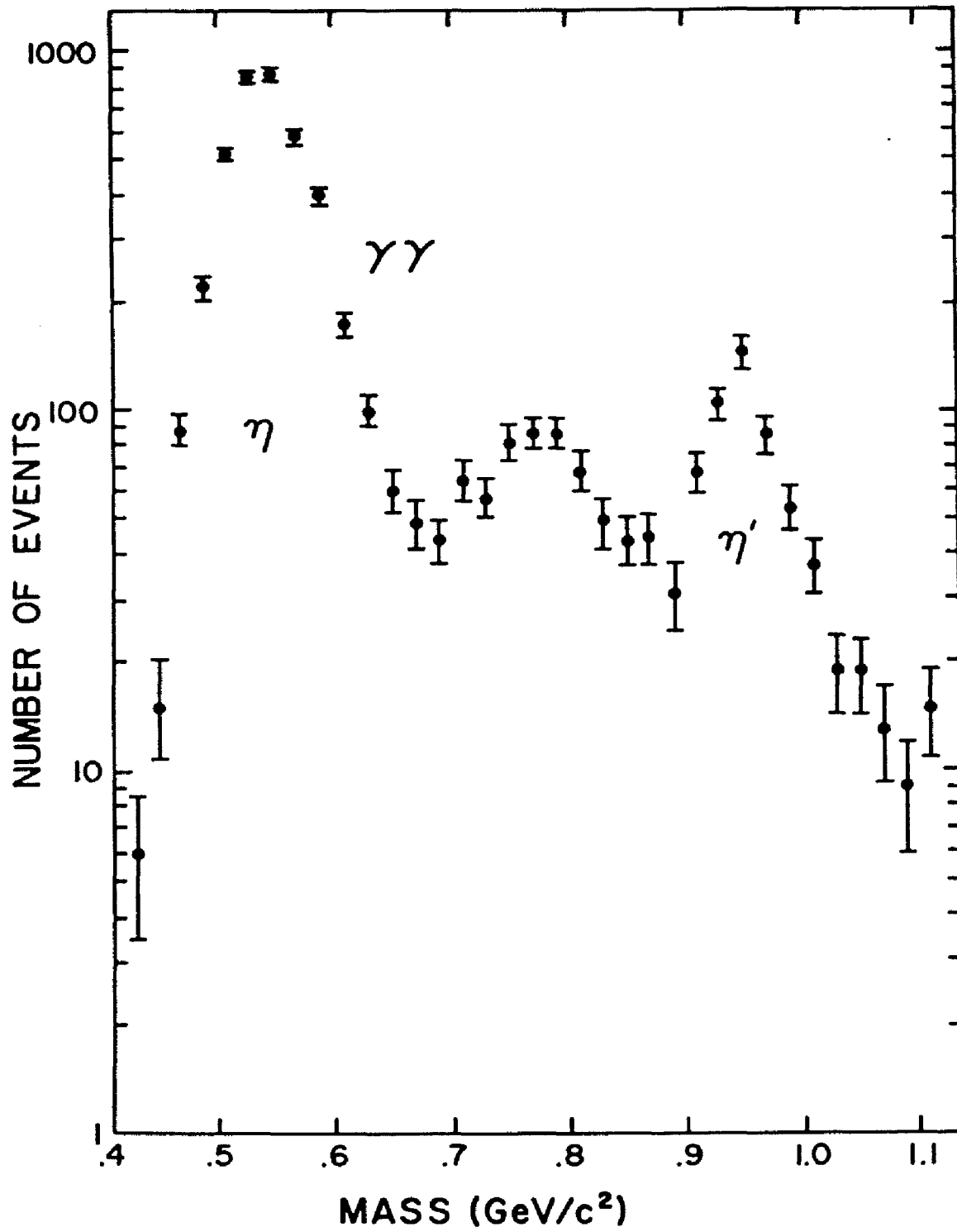


Figure 42 5 GeV/c $\gamma\gamma$ Mass Spectrum

TABLE 13

Summary of Systematic Errors

- 1) Geometrical efficiency (See Cross Section Tables)
 - a) Edge cuts
 - b) Beam energy
 - c) $\cos(\theta)$ distribution
 - d) T distribution
 - e) Beam centering
 - f) Beam profile
- 2) Number of live pions ($\leq 5\%$)
 - a) Dead time correction
 - b) Double counting of beam particles
- 3) Neutron self vetoing ($\leq 5\%$)
 - a) Cross section for vetoing
 - b) Detection efficiency of neutrons
 - c) Assumes no vetoing from nuclear breakup
- 4) Tight γ out efficiency ($\leq 5\%$)
 - a) Measured with electrons rather than photons
- 5) Rate dependence ($\leq 5\%$)
 - a) Measured only in test runs
 - b) Measured only for $\pi^+ \pi^0$ events
- 6) Nuclear Target
 - a) A dependence not known ($< 10\%$)

Net Normalization Error 14%

To calculate the acceptance for the η' we assumed a flat decay angular distribution and a differential cross section as measured by Stanton et al.²³ in 1979. Our measured cross section, which is shown in Table 14, is about a factor of two smaller than expected. This result, which is roughly 4 standard deviations from the expected result, may indicate the presence of increased shadowing in the carbon nucleus for the production of higher mass mesons. The measured width of the resonance, 62 MeV FWHM, agrees well with the Monte Carlo prediction of 73 MeV FWHM.

TABLE 14

Measurement of Five GeV/c η' Cross Section

Number of live pions	14.6 x 10 ⁹
Number of target protons	5.7 x 10 ²⁴
Neutron mass cut efficiency	.96
Neutron self vetoing	.88
Photon conversions in target	.81
Geometrical efficiency	.0240
Tight γ cut efficiency	.80
Photon must have hodoscope hits	.95
Rate dependence	.96

Systematic Errors

Detector inner edge cut	1%/cm	2.5%
Detector vertical dimensions	5%/cm	5%
Beam energy		.3%
Net normalization error (see text)		14%
Total systematic error		15%

Number of events 347 \pm 10.7%

$\sigma_B = 347$ nb	measured
600 nb	expected

5.3.2 Five GeV/c η

At 5 GeV/c the minimum opening distance of the two photons from η decay was smaller than the distance between the two detector arms, but an η that was produced with high "t", and that decayed very asymmetrically, could fit into the detector. Both photons in such an event were very close to the edge of the detector, making the acceptance very sensitive to small systematic effects. A fit to the mass region of .42 to .64 GeV with the hypothesis of a linear background plus a gaussian peak yielded a χ^2 of 12 for 6 degrees of freedom. No improvement was obtained with a quadratic background. To calculate the acceptance for the η a differential cross section as measured by Shaevitz et al.⁴¹ was used. The measured cross section, which is shown in Table 15, is about twice as large as the expected value. The measured width of this resonance, 85 MeV FWHM, agrees well with the Monte Carlo prediction of 74 MeV FWHM.

5.3.3 Eight GeV/c η'

Figure 43 shows the $\gamma\gamma$ mass spectrum, uncorrected by acceptance, obtained in the 8.5 GeV/c runs. A clear η' peak is evident. A fit to the mass region of .82 to 1.04 with a simple gaussian resonance and no background yielded a χ^2 of 4.9 for 8 degrees of freedom. For 8.5 GeV/c beams the acceptance for the η' was similar to that of the η at 5 GeV/c. The measurement of this cross section was therefore just as difficult and also subject to large systematic errors. The measured cross section, which is shown in Table 16, is about 1 standard deviation from the expected value. The measured width of the resonance, 97 MeV FWHM, also agrees well with the Monte Carlo prediction of 71 MeV FWHM.

Since both this and the preceding reaction are very sensitive to the acceptance of the experiment, they provided a unique opportunity to test our understanding of the acceptance of the experiment with the Monte Carlo. The experimentally measured $\cos(\theta)$ and "t" distributions

⁴¹ M. H. Shaevitz, et al., Phys. Rev. Lett. 36, p5 (1976).

TABLE 15

Measurement of Five GeV/c η Cross Section

Number of live pions	14.6 x 10 ⁹
Number of target protons	5.7 x 10 ²⁴
Neutron mass cut efficiency	.96
Neutron self vetoing	.88
Photon conversions in target	.74
Geometrical efficiency	.0027
Tight γ cut efficiency	.80
Photon must have hodoscope hits	.95
Rate dependence	.96

Systematic Errors

Detector inner edge cut	5%/cm	12.5%
Detector vertical dimensions	7%/cm	7%
Beam energy		14%
Target position	2.5%/cm	5%
Net normalization error (see text)		14%
Total systematic error		25%

Number of events 5020 \pm 3%

$\sigma.B = 49 \mu\text{b}$	measured
26.6 μb	expected

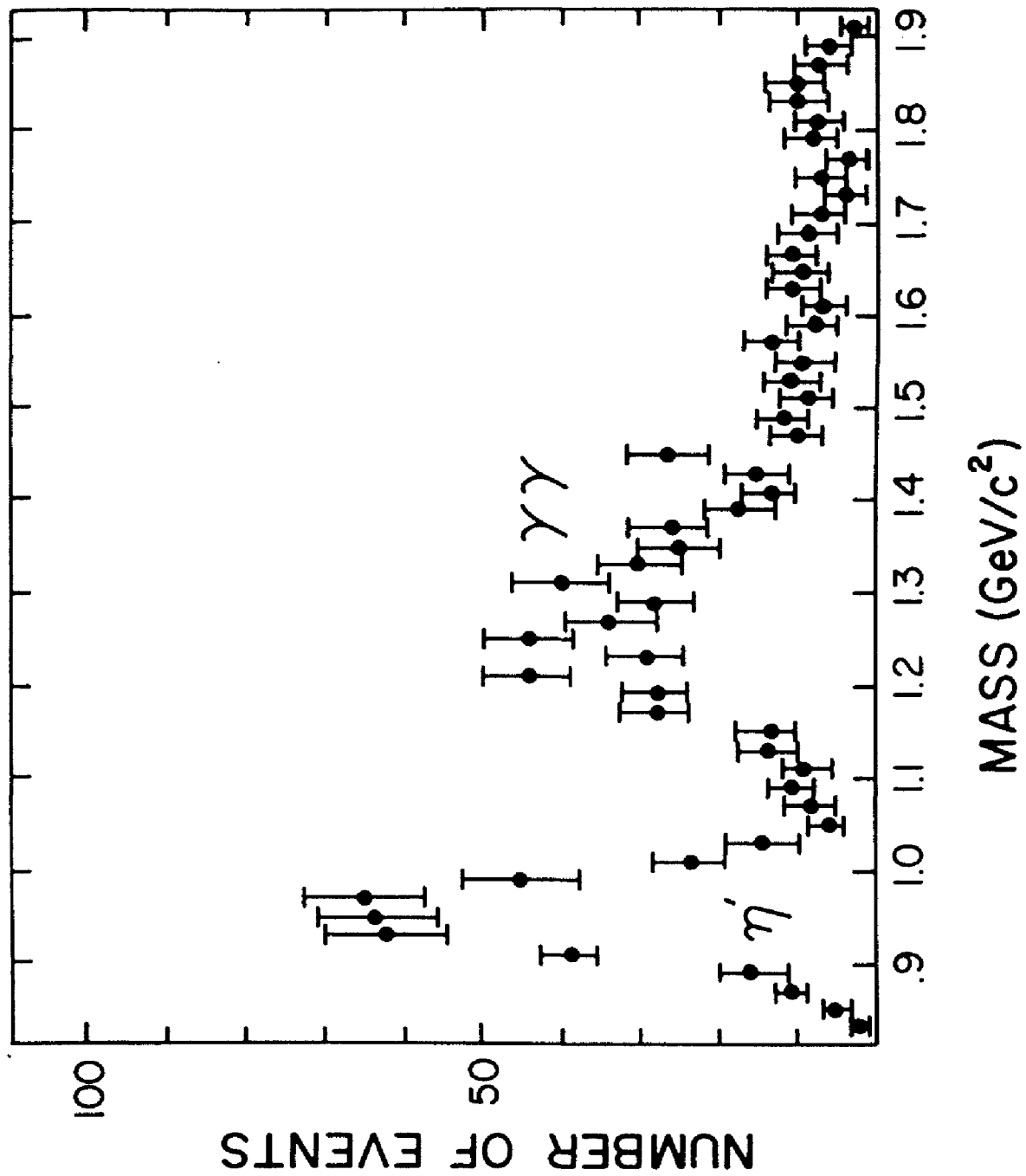


Figure 43 8.5 GeV/c γ Mass Spectrum

TABLE 16

Measurement of Eight GeV/c η' Cross Section

Number of live pions	91 x 10 ⁹	
Number of target protons	5.7 x 10 ²⁴	
Neutron mass cut efficiency	.94	
Neutron self vetoing	.88	
Photon conversions in target	.72	
Geometrical efficiency	.0046	
Tight γ cut efficiency	.80	
Photon must have hodoscope hits	.95	
Rate dependence	.85	
Systematic Errors		
Detector inner edge cut	7%/cm	17%
Detector vertical dimensions	7%/cm	7%
Beam energy		18%
Target position	6%/cm	12%
Beam centering and profile		5%
Net normalization error (see text)		14%
Total systematic error		33%
Number of events	337.4 \pm 5.3%	
$\sigma.B = 367$ nb	measured	
300 nb	expected	

were shown to be in adequate agreement with those predicted by the Monte Carlo for these reactions.

5.3.4 Five GeV/c ω

Figure 44 shows the $\pi^0 \gamma$ mass spectrum, uncorrected by acceptance, obtained in the 5 GeV/c runs. A clear ω peak stands out in the plot. A fit to the mass region of .7 to .9 GeV with the hypothesis of a linear background plus a gaussian peak yielded a χ^2 of 5.2 for 5 degrees of freedom. To determine the acceptance for this reaction experimental information describing the production and decay angular distributions was used in the Monte Carlo. We used the differential cross section of Anderson et al.⁴² to obtain the results listed in Table 17. This result agrees remarkably well with previous measurements, which are summarized by Holloway et al.⁴³

The full width of the ω peak, 99 MeV, is almost double the 55 MeV full width predicted by the Monte Carlo. This was the worst failure of the Monte Carlo in predicting the mass resolution of a narrow resonance and may indicate that the error in the reconstructed energy of low-energy photons may be larger than estimated.

⁴² J. C. Anderson, et al., Phys. Lett. 45B, p165 (1973).

⁴³ L. E. Holloway, et al., Phys. Rev. D 8, p2814 (1973).

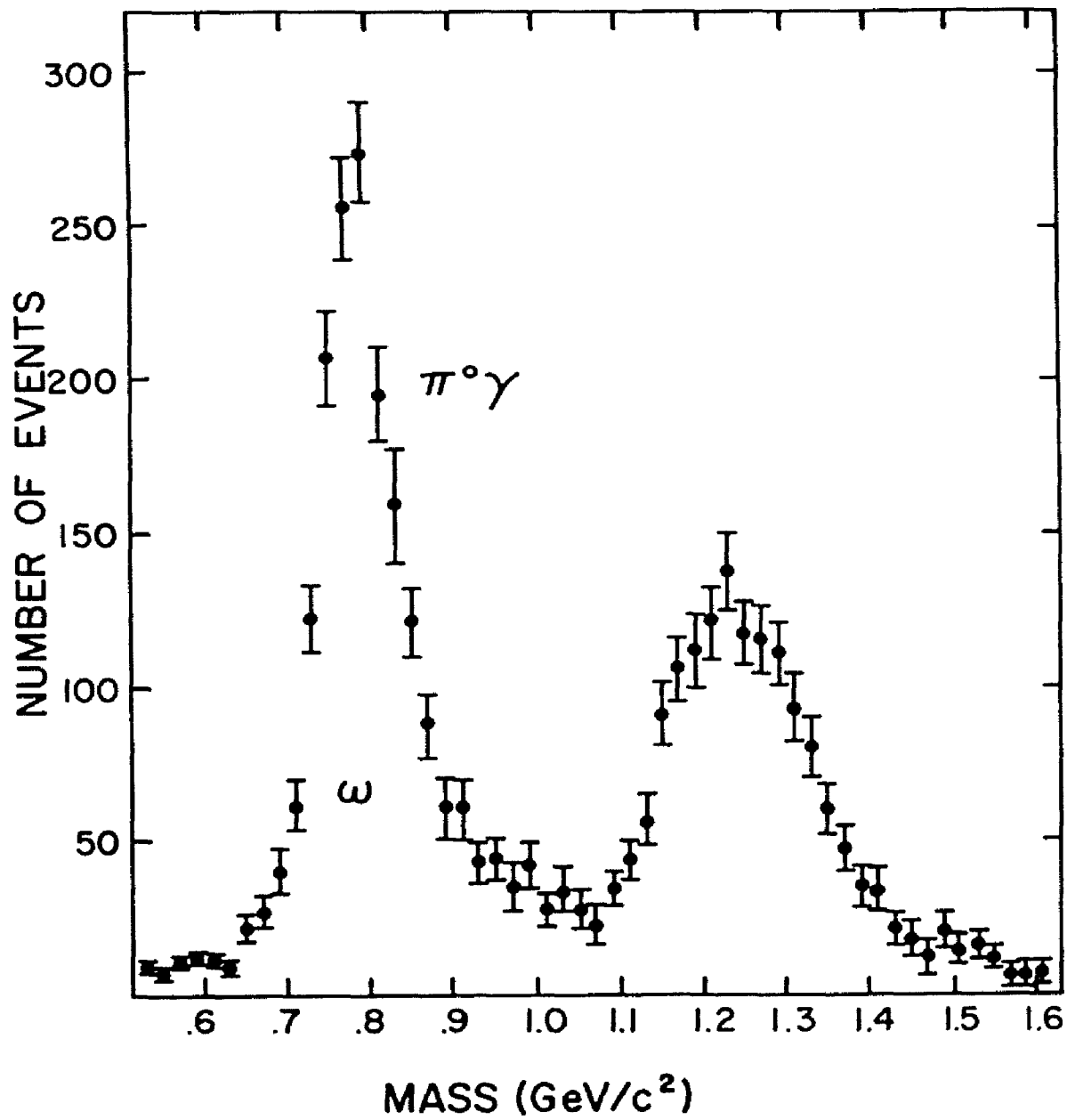


Figure 44 5 GeV/c $\pi^0 \gamma$ Mass Spectrum

TABLE 17

Measurement of Five GeV/c ω Cross Section

Number of live pions	14.6 x 10 ⁹
Number of target protons	5.7 x 10 ²⁴
Neutron mass cut efficiency	.96
Neutron self vetoing	.88
Photon conversions in target	.70
Geometrical efficiency	.0025
Tight γ cut efficiency	.90
Photon must have hodoscope hits	.97
Rate dependence	.96
Clean π^0 cuts	.97

Systematic Errors

Detector inner edge cut	2.8%/cm	7%
Detector vertical dimensions	8%/cm	8%
Beam energy		2%
Net normalization error (see text)		14%
Target position	.5%/cm	1%
Beam centering and profile		10%
Total systematic error		21%

Number of events 1226 \pm 11%

$\sigma.B = 12.3 \mu\text{b}$	measured
15.8 μb	expected

Chapter VI

RESULTS - SEARCH FOR NARROW TWO PHOTON RESONANCES

The major goal of this experiment was to search for narrow resonances decaying into two photons in the Charmonium mass region. The analysis of the data in this region is complete, and its interpretation is clear since the acceptance of the experiment was essentially constant in this region. These results will be presented in this chapter. The analysis of the rest of the data, however, is not complete.

Some possibly interesting effects will be seen in several of the reactions near the low-mass cut-off in acceptance, but comments on the existence of these effects, or their interpretation, cannot be made. The analysis of these effects requires a detailed knowledge of the acceptance of the experiment near the low-mass cut-off region, information that is not available at present.

6.1 Feed-down from $\pi^0 \pi^0$ Events

As is emphasized in Chapter 2, the main source of background for this experiment was from the feed-down of π^0 's into the photon data samples. The term "feed-down" refers to the process where a π^0 was produced in the reaction but was misidentified as a single photon. A very simple model for the shape of the background spectra was obtained by assuming the probability of π^0 feed-down to be a universal constant, independent of the invariant mass of the pair of π^0 's, or whether one or both π^0 's feed-down. If this was true, and there were no true $\gamma \gamma$ or $\pi^0 \gamma$ events in the mass region, the shape of the mass spectra should be the same in the $\pi^0 \gamma$ and $\gamma \gamma$ spectra as in the $\pi^0 \pi^0$ spectra. This of course assumes that there were no other strong sources of events that could feed-down into those mass spectra, such

as $\eta \pi^0$ events or $\eta \eta$ events. Feed-down from such events should be suppressed both by the 38% branching ratio of the η into the two photon decay mode, and by the fact that such events are much rarer than $\pi^0 \pi^0$ events. Our measurements of some of these cross sections will place limits on their contributions to the background in the $\pi^0 \gamma$ and $\gamma \gamma$ reactions.

To test the simple feed-down assumption I have displayed the $\pi^0 \pi^0$, $\pi^0 \gamma$, and $\gamma \gamma$ mass spectra obtained in the 8.5 GeV/c run together in Figure 45. The smooth curves drawn through the $\pi^0 \gamma$ and $\gamma \gamma$ spectra represent the expected background levels assuming a π^0 feed-down probability of 7.14%. The shape of the $\pi^0 \pi^0$ spectrum clearly matches both the $\pi^0 \gamma$ and the $\gamma \gamma$ spectrum well at masses above 1.6 GeV, where the acceptance was stable. A one parameter fit to the $\gamma \gamma$ mass region of 1.6 to 2.2 GeV, allowing the π^0 feed-down probability to vary, yielded a χ^2 of 18.6 for 19 degrees of freedom with a π^0 feed-down probability of $8 \pm .4\%$. The simple feed-down hypothesis clearly provided an adequate description of the data in this region.

A one parameter fit to the $\pi^0 \gamma$ mass region of 1.6 to 2.2 GeV, with the same hypothesis, yielded a χ^2 of 47.9 for 20 degrees of freedom with a π^0 feed-down probability of $7.7 \pm 1.3\%$. In this case there was a clear deviation from the simple feed-down hypothesis, but the $\pi^0 \gamma$ sample was large enough to be sensitive to feed-down from other channels, such as $\pi^0 \eta$, at the level of a few percent.

6.1.1 Limits on Narrow $\gamma \gamma$ Resonances in the 1.6 to 1.9 GeV Mass Range

To place a limit on the possible production of resonances with a width much smaller than the experimental resolution of roughly 120 MeV a fit was made to determine the best gaussian shape that could be put into the spectrum. For all the cases described below the gaussian width was allowed to vary within 10% of the Monte Carlo predicted value, and the amplitude was allowed to be either positive or negative. If the resultant amplitude of the gaussian was negative, I

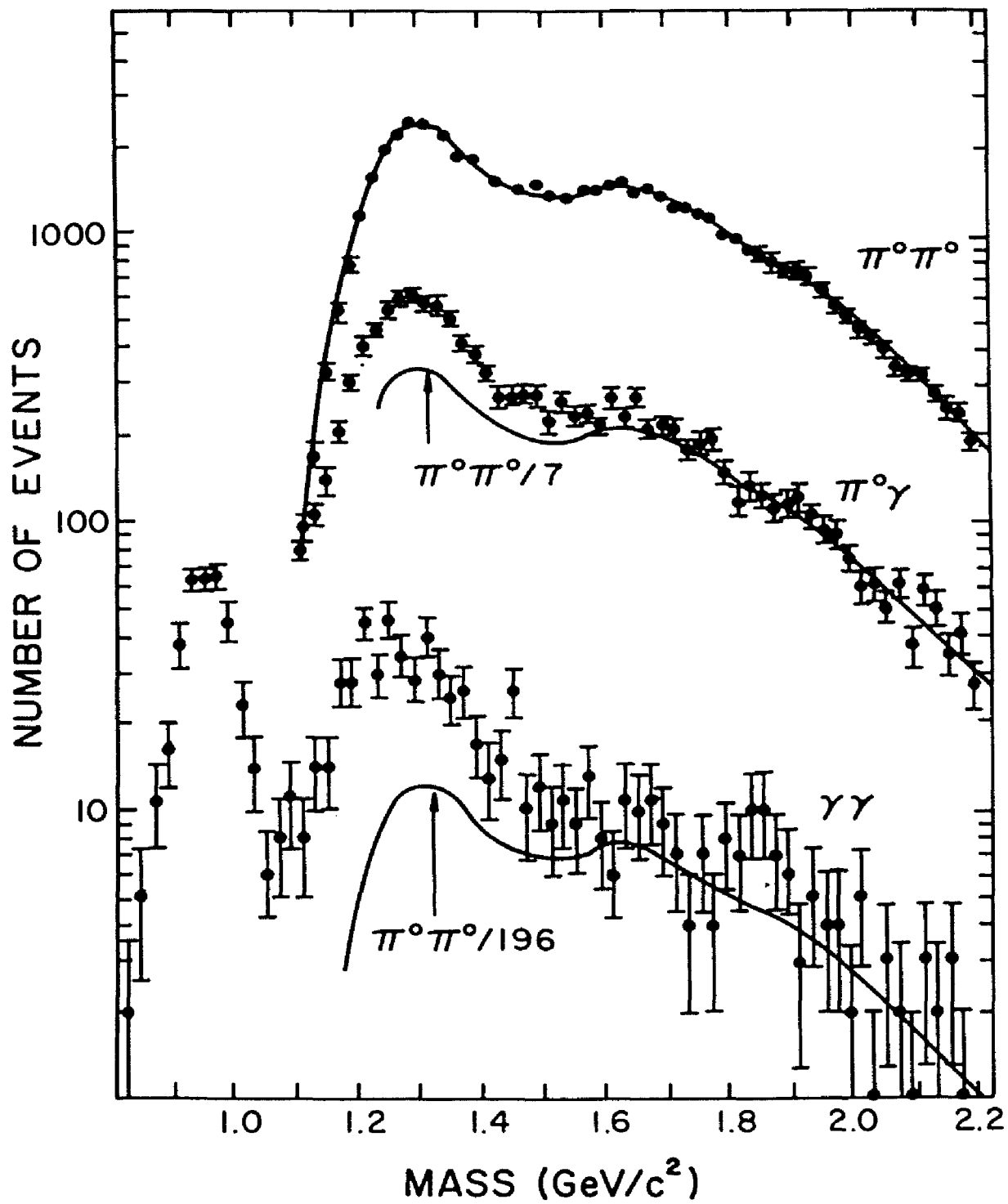


Figure 45 8.5 GeV/c $\pi^0\pi^0$, $\pi^0\gamma$, and $\gamma\gamma$ Mass Spectra

considered the measured cross section to be zero, and the 90% confidence level upper limit was simply 1.6 times the error on the amplitude. If the resultant amplitude of the gaussian was positive, I considered it to be an experimentally measured cross section. This cross section was added to 1.6 times the error on the amplitude to obtain the 90% confidence level upper limit.

I used the simple feed-down hypothesis to model the background shape in the mass region of 1.6 to 1.9 GeV, which was divided into 7 regions, each 50 MeV wide. For each region I fit the mass spectrum between 1.6 and 2 GeV with the hypothesis of simple feed-down plus a gaussian resonance constrained to be centered somewhere within the mass region under test. Table 18 shows the results of this fit and the limits placed on the cross section for each of the mass intervals. No resonances are seen in this mass region, and the 90% confidence level upper limits vary from 1.2 to 3.6 nb, with the average being 2.1 nb.

6.1.2 Limits on $X(2.83)$ Production

Figure 46 shows the $\pi^0 \pi^0$, $\pi^0 \gamma$, and $\gamma \gamma$ mass spectra obtained in the 13 GeV/c running. The smooth curves drawn through the $\pi^0 \gamma$ and $\gamma \gamma$ spectra are simply the background expected for a π^0 feed-down probability of 4.5%. These curves clearly fit the data well through most of the region between 2.2 and 3.2 GeV, with two exceptions being the region around 2.8 GeV in the $\gamma \gamma$ mass spectrum and 2.4 GeV in the $\pi^0 \gamma$ mass spectrum. In addition, the region near 2.2 GeV in the $\pi^0 \gamma$ spectrum shows some structure incompatible with a smooth deviation from the simple feed-down mechanism. The interpretation of these effects in the $\pi^0 \gamma$ spectrum requires an investigation of the possibility of feed-down from more complex final states and will not be discussed in this thesis.

A one parameter fit to the region of 2.2 to 3.2 GeV in the $\gamma \gamma$ mass spectrum, with the hypothesis of simple feed-down from the $\pi^0 \pi^0$

Table 18

Mass Region Under Test (GeV)	Gaussian Width (MeV)	Best Fit Mass (MeV)	Best Fit Width (MeV)	$\chi^2/D.F.$ of Fit	Feed-Down from $\pi^0\pi^0$	Gaussian Amplitude (Events)	90% C.L. Limit
1.625-1.675	66-80	1675±42	80	18.6/19	.0064	-5±8.4	1.8 nb
1.675-1.725	68-83	1725±33	68	16.4/19	.0068	-12±7.0	1.5 nb
1.725-1.775	70-85	1734±16	70	16.2/19	.0068	-12±7.0	1.6 nb
1.775-1.825	72-88	1825±30	72	14.9/19	.0058	12.5±7.3	3.5 nb
1.825-1.875	74-90	1838±17	74	14.4/19	.0058	12.9±7.1	3.6 nb
1.875-1.925	76-93	1925±50	76	18.5/19	.0064	-2.5±4.8	1.2 nb
1.925-1.975	78-96	1940±42	78	18.5/19	.0065	-2.5±5.5	1.4 nb

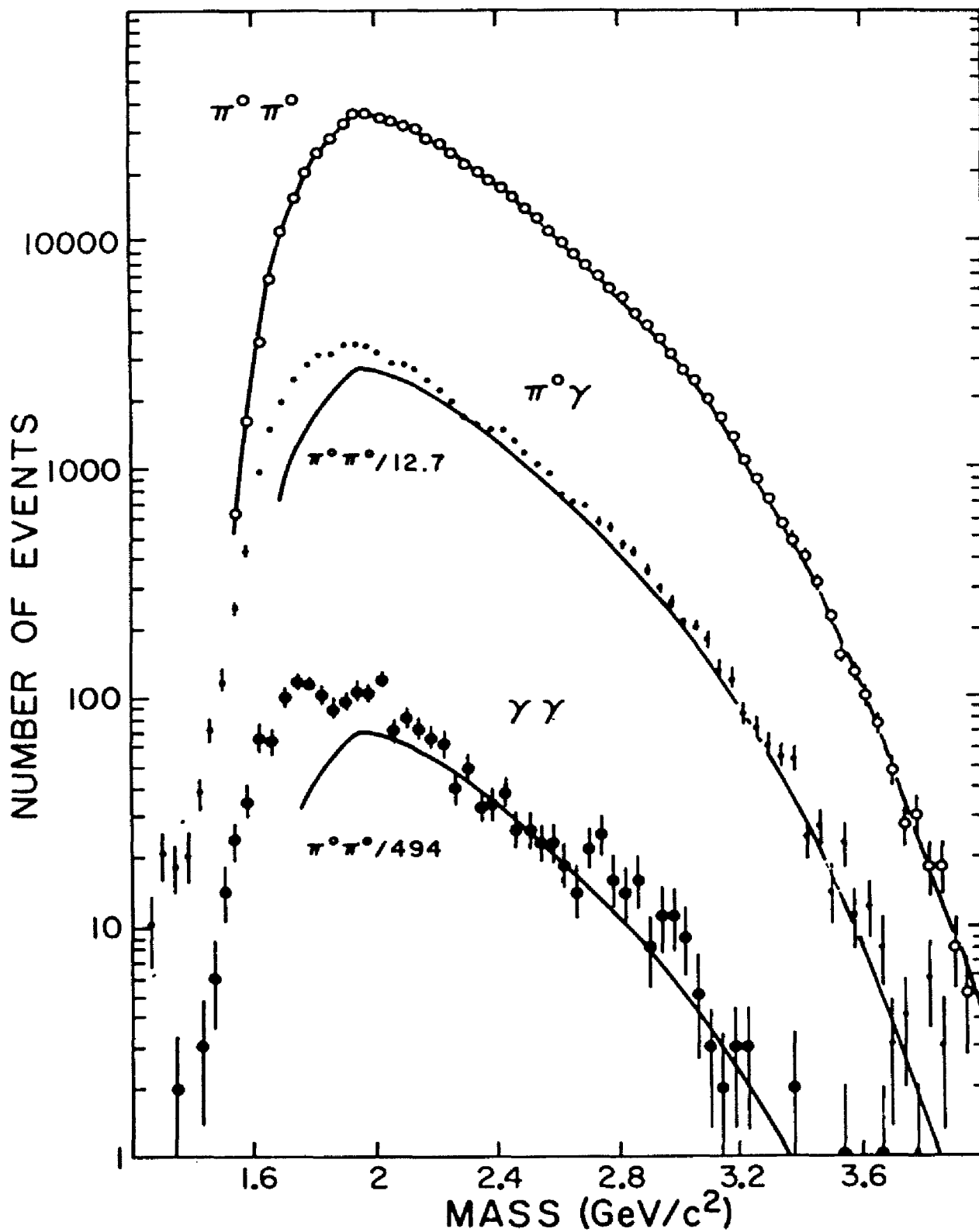


Figure 46 13 GeV/c $\pi^0 \pi^0$, $\pi^0 \gamma$, and $\gamma \gamma$ Mass Spectra

spectrum, yielded a χ^2 of 30.7 for 23 degrees of freedom with a π^0 feed-down probability of 4.6%. This fit is shown as the solid line in Figure 47.

In order to place a limit on the existence of narrow resonances in the 2.3 to 3.0 GeV mass range I divided that mass region into 15 regions, each of which was 50 MeV wide. Each region was fit with the hypothesis of simple feed-down, as described above, plus a gaussian resonance, whose center was constrained to be within the mass region under test. The results, listed in Table 19, show that the best fit was obtained with a gaussian resonance in the mass region of 2.775 to 2.825 GeV. This fit yielded a χ^2 of 20.6 for 20 degrees of freedom with a π^0 feed-down probability of 4.5% and is shown as the dashed line in Figure 47. The resultant gaussian was centered at $2.78 \pm .043$ GeV and had a width of 124 MeV, consistent with our expected resolution at this mass. This is roughly a 2.7 standard deviation effect. The systematic error on the reconstructed mass may be as high as 1 to 2 percent.

Based on the normalization factor listed in Table 20, the amplitude of 27.5 ± 10 events is interpreted as a 90% confidence level upper limit of 114 pb for the production of a resonance at 2.78 GeV. This normalization factor was calculated assuming the signal to be from a spin zero resonance with a differential cross section similar to that of the η' :

$$d\sigma/dt = (1-38t)e^{9.1t}$$

Table 21 shows the expected change in the acceptance for several differential cross sections. The acceptance is stable to a few percent over this wide range of input distributions.

Table 19

Mass Region Under Test (GeV)	Gaussian Width (MeV)	Best Fit Mass (MeV)	Best Fit Width (MeV)	$\chi^2/D.F.$ of Fit	Feed-Down from $\pi^0\pi^0$	Gaussian Amplitude (Events)	90% C.L. Limit
2.325-2.375	78-95	2325±45	95	27.4/20	.00221	-27.±14.	67 pb
2.375-2.425	80-98	2375±42	98	29.1/20	.00217	-11.±13.	60 pb
2.425-2.475	83-101	2470±32	101	27.8/20	.00219	-21.±12.	55 pb
2.475-2.525	86-105	2475±50	105	27.8/20	.00219	-22.±12.	55 pb
2.525-2.575	88-108	2525±43	108	28.8/20	.00217	-15.±11.	49 pb
2.575-2.625	91-111	2618±32	91	29.4/20	.00215	-11.±7.8	35 pb
2.625-2.675	94-114	2675±32	114	30.0/20	.00208	8.4±11.	69 pb
2.675-2.725	96-118	2725±87	118	24.0/20	.00201	22.4±10.	104 pb
2.725-2.775	99-121	2775±50	121	20.7/20	.00199	27.0±10.	115 pb
2.775-2.825	102-124	2780±43	124	20.6/20	.00199	27.4±9.8	114 pb
2.825-2.875	104-127	2825±32	127	22.0/20	.00200	24.5±9.9	105 pb
2.875-2.925	107-131	2875±39	131	24.0/20	.00202	20.0±8.9	88 pb
2.925-2.975	109-134	2925±50	134	24.5/20	.00203	18.0±8.4	80 pb
2.975-3.025	112-137	2975±38	137	25.3/20	.00205	14.5±7.7	67 pb
3.025-3.075	115-140	3025±32	115	27.5/20	.00207	8.9±5.9	45 pb

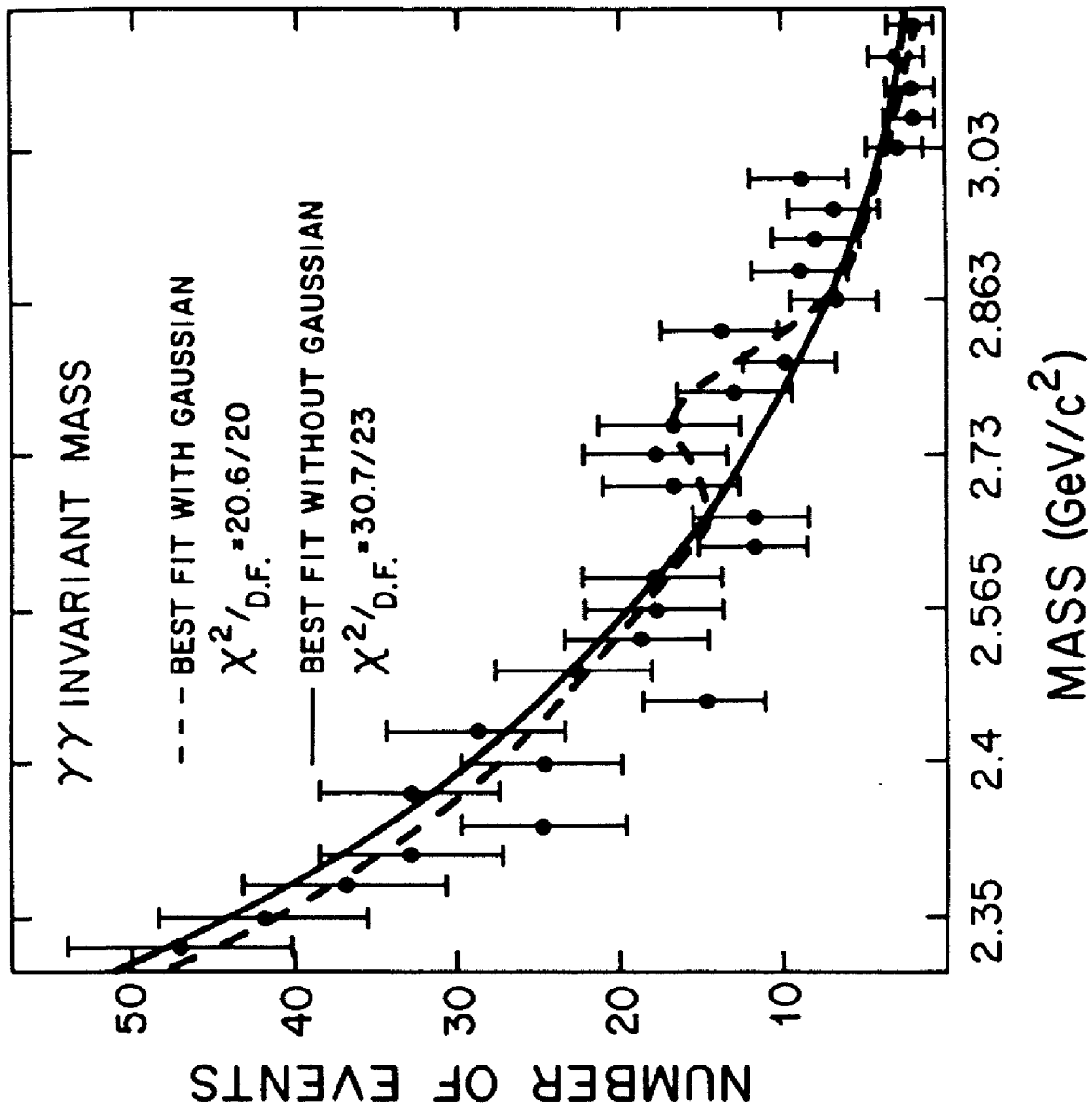


Figure 47 13 GeV/c γ Mass Spectrum with Fits

TABLE 20

Calculation of 13 GeV/c $\gamma \gamma$ Sensitivity

(For mass of 2.8 GeV)

Number of live pions	3.19×10^{12}
Number of target protons	5.7×10^{24}
Neutron mass cut efficiency	.94
Neutron self vetoing	.88
Photon conversions in target	.74
Geometrical efficiency	.065
Tight γ cut efficiency	.80
Photon must have hodoscope hits	.95
Rate dependence	.70

Systematic Errors

Detector inner edge cut	1%/cm	2.5%
Detector vertical dimensions	4%/cm	4%
Net normalization error (see text)		14%
Total systematic error		15%

$\sigma.B = 2.6$ pb per event

TABLE 21
Change in $\gamma\gamma$ Acceptance with Different
Differential Cross Sections

<u>Differential Cross Section</u>	<u>Percentage Change</u>
$(1-38t)_{e^{9.1t}}$	0%
$(1-38t)_{e^{12t}}$	+4.0%
$(1-38t)_{e^{6t}}$	-6.7%
$(1-60t)_{e^{9.1t}}$	0%
$_{e^{9.1t}}$	+3.8%

6.1.3 Limits on Other Narrow $\gamma\gamma$ Resonances in the 2.2 to 3.0 GeV Mass Range

To place an upper limit on the production of narrow resonances at masses other than 2.78 GeV in the $\gamma\gamma$ mass spectrum I used the background shown as the dashed line in Figure 47, including the gaussian resonance. This function, although it certainly could have been improved, provided an adequate description of the $\gamma\gamma$ spectrum. I divided the mass spectrum into 15 different mass regions and fit the spectrum with the hypothesis of that background plus a second gaussian resonance, whose center was constrained to be within the mass region under test. The results of this fit are listed in Table 22. The best fit was obtained with a second gaussian resonance centered at 2.98 GeV, but this was only a 2 standard deviation effect, which was statistically insignificant.

6.1.4 Limits on Narrow $\gamma\gamma$ Resonances in the 1.3 to 1.6 GeV Mass Range

A beam momentum of 8.5 GeV/c was a good choice for a search for narrow resonances decaying into two photons in the 1.2 to 2 GeV mass range. Figure 43 shows an expanded view of the $\gamma\gamma$ mass spectrum obtained with about three days of data taking at this beam momentum.

Table 22

Mass Region Under Test (GeV)	Gaussian Width (MeV)	Best Fit Mass (MeV)	Best Fit Width (MeV)	$\chi^2/D.F.$ of Fit	Gaussian Amplitude (Events)	90% C.L. Limit
2.325-2.375	78-95	2325±50	78	19.8/17	-10.±11.	53 pb
2.375-2.425	80-98	2425±50	98	20.3/17	-5.5±11.	52 pb
2.425-2.475	83-101	2472±45	83	19.7/17	-10.±9.4	44 pb
2.475-2.525	86-105	2475±42	86	19.7/17	-10.±9.5	44 pb
2.525-2.575	88-108	2525±45	108	20.2/17	-6.5±10.	46 pb
2.575-2.625	91-111	2625±50	91	19.9/17	-6.9±8.1	36 pb
2.625-2.675	94-114	2633±27	94	19.9/17	-7.1±8.1	36 pb
2.675-2.725	96-118	2725±48	96	20.5/17	2.7±8.1	43 pb
2.725-2.775	99-121	2725±50	99	20.5/17	2.6±8.4	43 pb
2.775-2.825	102-124	2791±32	102	20.5/17	-1.9±8.5	36 pb
2.825-2.875	104-127	2875±35	127	19.0/17	9.0±7.9	57 pb
2.875-2.925	107-131	2925±33	131	16.3/17	13.6±7.6	66 pb
2.925-2.975	109-134	2975±50	119	14.6/17	13.2±6.9	61 pb
2.975-3.025	112-137	2982±26	112	14.6/17	12.7±6.3	57 pb
3.025-3.075	115-140	3025±32	115	16.4/17	9.8±5.8	47 pb

Without a proper Monte Carlo simulation of the feed-down the background in this mass region cannot be predicted from the $\pi^0 \pi^0$ spectrum. Instead, in order to place a limit on the production resonances near the E(1420), I divided the mass spectrum into 11 mass intervals, each 50 MeV wide, and subjected each region to the fitting procedure described below.

For each region the Monte Carlo predicted resolution width was calculated. The entire mass spectrum in the region of 1.2 to 2 GeV, with the exception of the points lying within 1 full width of the center of the mass region under test, was fit to a 6th order polynomial. This polynomial was then used as the background for the entire mass spectrum. A gaussian peak was then added to the background function, whose center was constrained to be within the mass region under test. The results of this fit are listed in Table 23. In the two mass intervals nearest the E(1420) the upper limits were 2.75 and 1.53 nb. I took the average of these two results to place a limit of 2.1 nb, 90% confidence level, on the production cross section times branching ratio for the E(1420). The normalization factor, shown in Table 24, was calculated assuming a spin of zero and a differential cross section of:

$$d\sigma/dt = e^{8t}$$

6.2 Exotic Channels

The acceptance of our experiment to reactions with an η in the final state was small, but nevertheless we obtained a significant exposure. Figure 48 shows the invariant mass of photon pairs detected on a single arm of the detector during the 13 GeV/c data run. A clear η peak is seen with less than 10% background. Most of these η s were associated with either a π^0 or a photon on the other arm. In very rare events an η was detected on both arms. These η s may in fact have been caused by background processes, so our measurements of the $\eta \eta$ cross section should be interpreted as an upper limit.

Table 23

Mass Region Under Test (GeV)	Gaussian Width (MeV)	Region of Polynomial Fit (GeV)	χ^2 /D.F. of Poly. Fit	χ^2 /D.F. of Gauss Fit	Best Fit Mass (MeV)	Gaussian Amplitude (Events)	90% C.L. Limit
1.325-1.375	59	1.2-1.291, 1.409-2.0	.85	31.4/30	1325±38	27.0±11.7	5.17 nb
1.375-1.425	61	1.2-1.339, 1.461-2.0	.78	31.9/31	1425±7	10.4±9.3	2.75 nb
1.425-1.475	63	1.2-1.387, 1.513-2.0	.75	31.9/31	1450±37	1.3±8.3	1.53 nb
1.475-1.525	66	1.2-1.434, 1.566-2.0	.80	31.8/31	1475±8	11.8±9.0	2.62 nb
1.525-1.575	68	1.2-1.482, 1.618-2.0	1.03	32.3/31	1525±25	-2.4±7.5	1.17 nb
1.575-1.625	71	1.2-1.529, 1.671-2.0	.97	33.5/31	1625±8	17.8±7.7	2.78 nb
1.625-1.675	73	1.2-1.577, 1.723-2.0	.95	29.7/31	1659±16	16.7±7.2	2.51 nb
1.675-1.725	75	1.2-1.625, 1.775-2.0	.84	30.5/31	1725±31	-8.1±6.5	.91 nb
1.725-1.775	78	1.2-1.672, 1.828-2.0	.82	27.8/31	1747±16	-19.±5.8	.78 nb
1.775-1.825	80	1.2-1.720, 1.880-2.0	.81	29.4/31	1825±31	12.2±6.8	1.86 nb
1.825-1.875	82	1.2-1.768, 1.932-2.0	.91	28.3/31	1833±14	18.1±6.8	2.26 nb

TABLE 24

Calculation of Eight GeV/c E(1420) Sensitivity

Number of live pions	91 x 10 ⁹
Number of target protons	5.7 x 10 ²⁴
Neutron mass cut efficiency	.94
Neutron self vetoing	.88
Photon conversions in target	.79
Geometrical efficiency	.0425
Tight γ cut efficiency	.80
Photon must have hodoscope hits	.95
Rate dependence	.85

Systematic Errors

The acceptance for the E(1420) at 8.5 GeV/c is similar to that for the η' at 5 GeV.

That result is used here:

Total systematic error	15%
------------------------	-----

$\sigma.B = 107$ pb per event

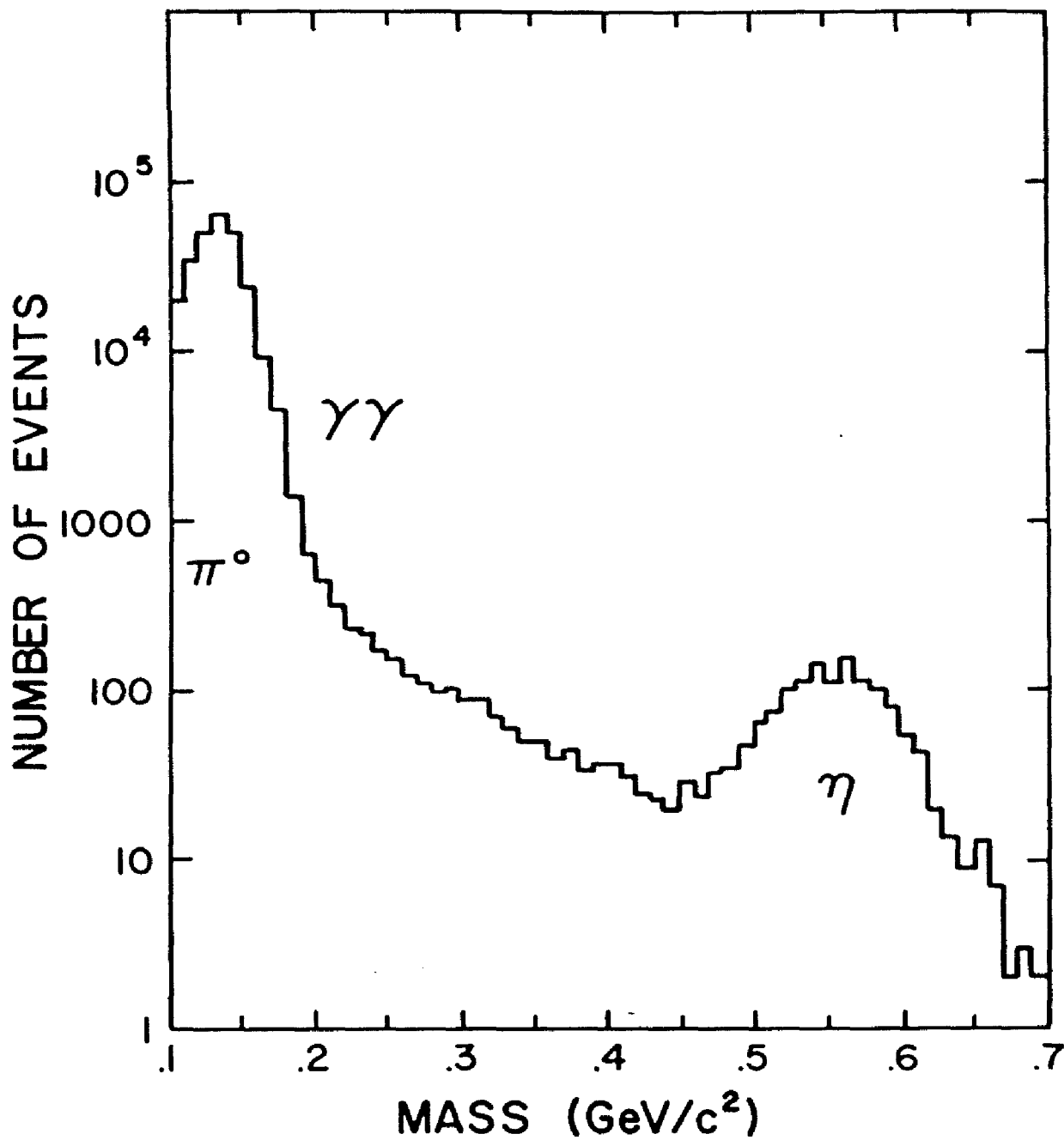


Figure 48 $\gamma\gamma$ Mass Spectrum on One Arm for 13 GeV/c Data

6.2.1 $\eta \pi^0$ Cross Section

Figure 49 shows the $\eta \pi^0$ mass spectrum obtained in the 13 GeV/c running. No structure is seen that has a width compatible with the predicted mass resolution of 120 MeV. The sensitivity for this reaction was calculated to be 160 pb per event at a mass of 2.8 GeV, as is shown in Table 25, assuming unpolarized or spin 0 resonance production with a differential cross section of:

$$d\sigma/dt = e^{8t}$$

Our measurement of this cross section allowed us to estimate that roughly 3% of the $\gamma \gamma$ events and 10% of the $\pi^0 \gamma$ events were actually feed-down from the $\eta \pi^0$ events.

6.2.2 $\eta \eta$ and $\eta \gamma$ Cross Sections

Figure 50 shows the $\eta \eta$ and $\eta \gamma$ mass spectra obtained in the 13 GeV/c data runs. The normalization factors for these reactions were calculated assuming the production of an unpolarized resonance with a differential cross section as stated above for the $\eta \pi^0$ events. The sensitivity for the $\eta \gamma$ final state was 100 pb per event, as is shown in Table 26, and the sensitivity for the $\eta \eta$ final state was 5 nb per event, as is shown in Table 27. This measurement of the $\eta \eta$ cross section allowed us to estimate that roughly 2% of the $\gamma \gamma$ events were actually feed-down from the $\eta \eta$ events. The number of $\eta \gamma$ events was roughly consistent with being a result of feed-down from the $\eta \eta$ events, although "roughly" in this context means "within a factor of five". Further Monte Carlo studies should improve these results.

6.3 Conclusion

We have set a sensitive upper limit on the production of the η_c and the X(2.83) in pion nucleon interactions. Figure 51 shows the 90% confidence level upper limit obtained for narrow resonances as a function of mass for the 8.5 and 13 GeV/c data runs. Although the statistical fluctuation seen in our data at 2.78 GeV was not signifi-

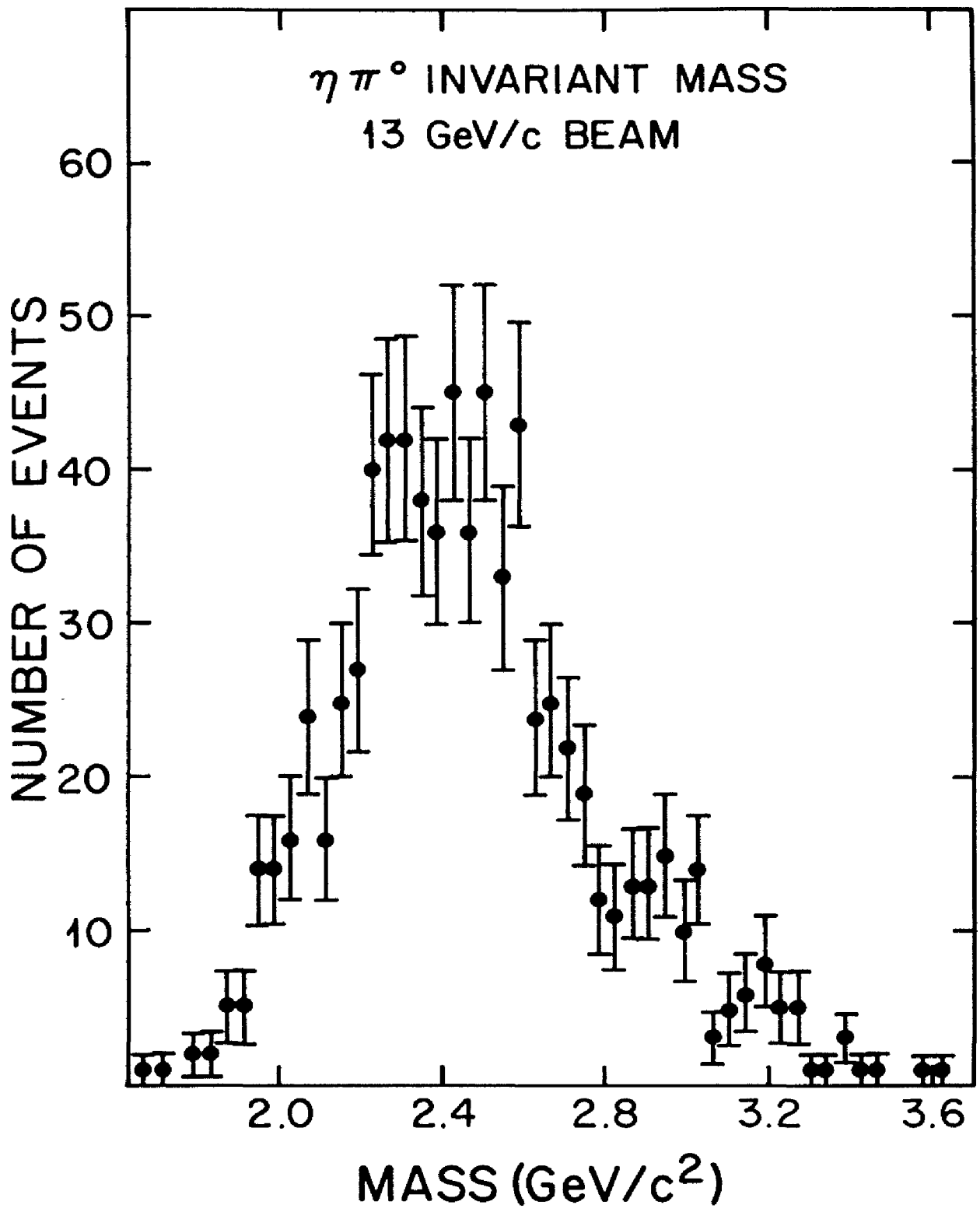


Figure 49 13 GeV/c $\eta \pi^0$ Mass Spectrum

TABLE 25

Calculation of 13 GeV/c η π^0 Sensitivity

(For mass of 2.8 GeV)

Number of live pions	3.19 x 10 ¹²
Number of target protons	5.7 x 10 ²⁴
Neutron mass cut efficiency	.94
Neutron self vetoing	.88
Geometrical efficiency	.0022
Tight event cut efficiency	.80
η mass window	.9
Rate dependence	.70
$\eta \rightarrow \gamma \gamma$.38

Systematic Errors

Detector inner edge cut	2%/cm	5%
Detector vertical dimensions	11%/cm	11%
η mass cut		10%
Net normalization error (see text)		14%
Total systematic error		21%

$\sigma.B = 158$ pb per event

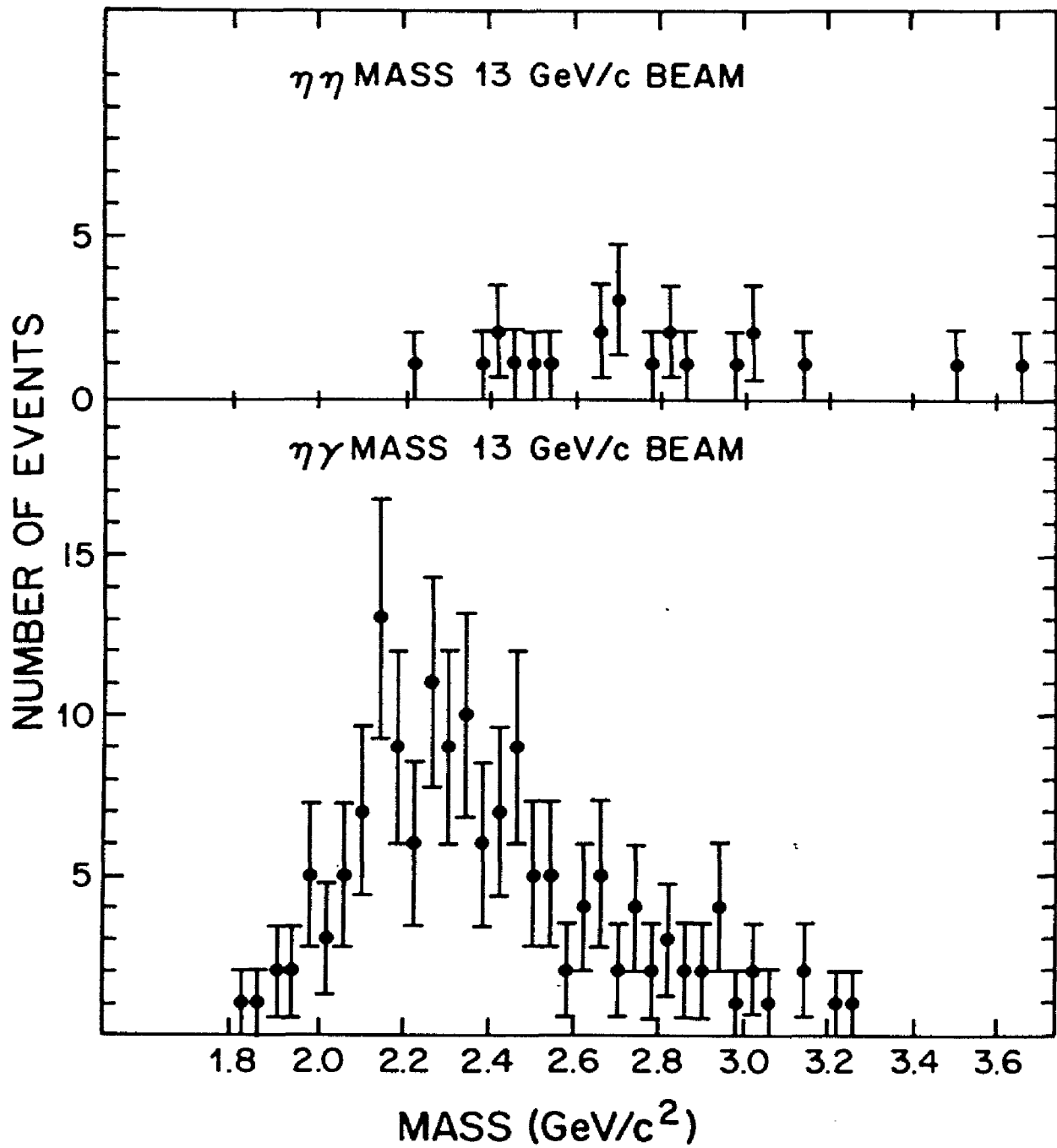


Figure 50 13 GeV/c η η and η γ Mass Spectra

TABLE 26

Calculation of 13 GeV/c η γ Sensitivity

(For mass of 2.8 GeV)

Number of live pions	3.19×10^{12}
Number of target protons	5.7×10^{24}
Neutron mass cut efficiency	.94
Neutron self vetoing	.88
Geometrical efficiency	.0034
Tight γ cut efficiency	.90
Photon must have hodoscope hits	.97
Tight event cut efficiency	.95
η mass window	.9
Rate dependence	.70
$\eta \rightarrow \gamma \gamma$.38

Systematic Errors

The acceptance for the η γ final state is similar to that for the η π^0 final state. That result is used here:

Total systematic error 21%

$\sigma.B = 98$ pb per event

TABLE 27

Calculation of 13 GeV/c η η Sensitivity

(For mass of 2.8 GeV)

Number of live pions	3.19 x 10 ¹²
Number of target protons	5.7 x 10 ²⁴
Neutron mass cut efficiency	.94
Neutron self vetoing	.88
Geometrical efficiency	.00018
Tight event cut efficiency	.95
η mass window	.8
Rate dependence	.70
$\eta \rightarrow \gamma \gamma$.144

Systematic Errors

Detector inner edge cut	6%/cm	12%
Detector vertical dimensions	14%/cm	14%
Target position	1%/cm	2%
η mass cut		14%
Net normalization error (see text)		14%
Monte Carlo statistics		25%
Total systematic error		37%

$\sigma.B = 4.8$ nb per event

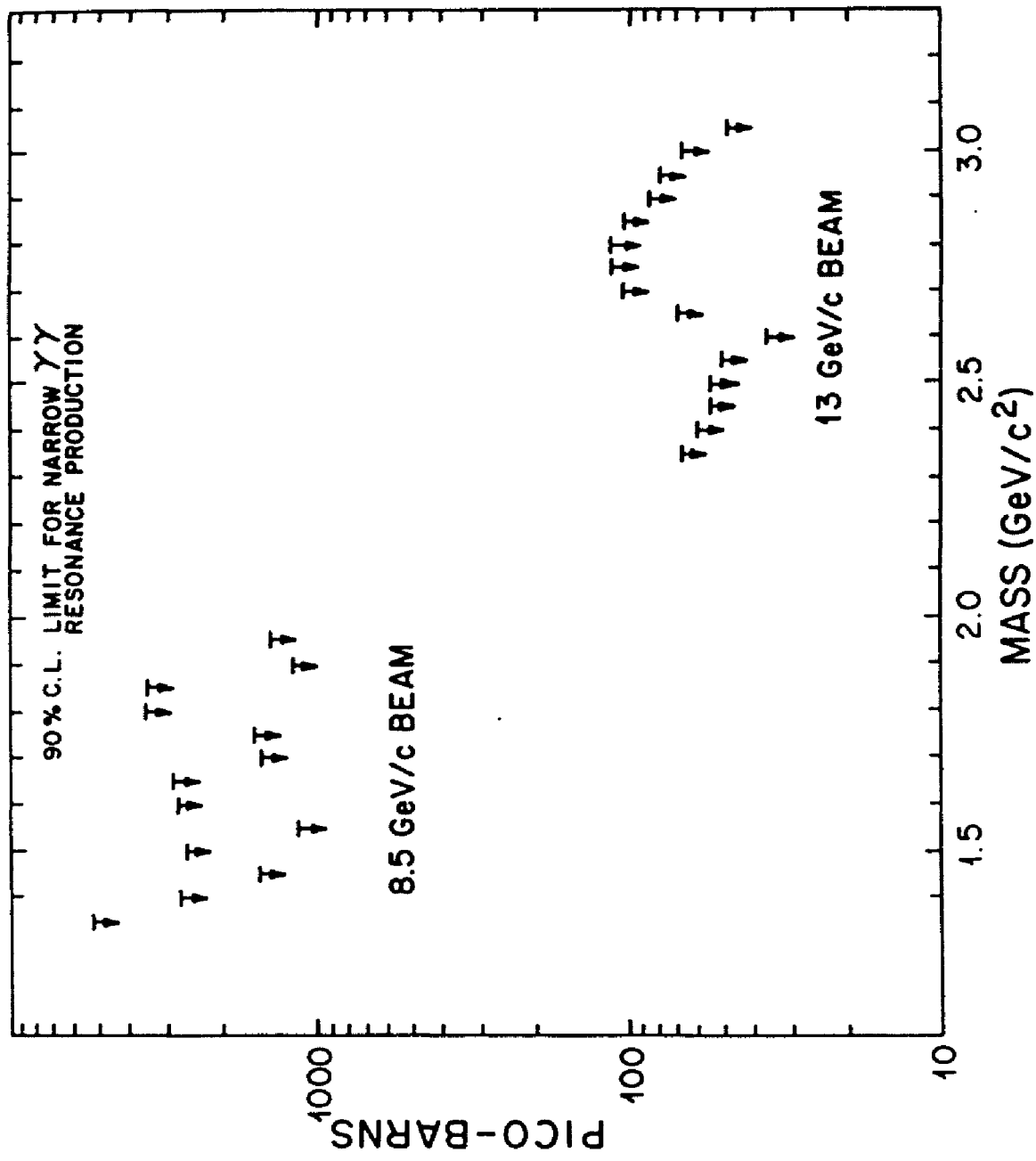


Figure 51 Upper Limit on γ Cross Sections for Resonances Much Narrower Than Our Resolution

cant enough to be interpreted as a resonance, it is curious that it appeared near the same mass as the result of Apel et al.⁶. To compare our results with theirs we must ask the question: can a resonance have a cross section of 200 ± 100 pb at a beam momentum of 40 GeV/c, and 71 ± 25 pb at a beam momentum of 13 GeV/c? We are helped by the fact that Apel et al.⁶ made a cut on t of $.15$ (GeV/c)², which was comparable to our t_{\min} of $.14$ (GeV/c)². This eliminates the possibility that the cross section was suppressed at our beam momentum by a large phase space factor brought about by the production of a resonance with a steep differential cross section. The only way for the two measurements to be in agreement is for the cross section to vary as:

$$\sigma = p^{0 \pm .6} \int_{t_{\min}}^{t_{\max}} f(t) dt$$

The function $f(t)$ should be similar to the η' differential cross section. Such a momentum dependence is not expected for the η_c , nor for any other ordinary meson.

6.4 Future Prospects

We seem to have been unfortunate in that most of the possibly interesting effects in our data appear to have occurred near the low-mass cut-off regions of the acceptance. The proper interpretation of such effects requires the use of a Monte Carlo simulation program, and although we have such a program, it will require up to several hundred hours of computer time for an extensive investigation of the acceptance. In addition, for events with η_s in the final state, we have not used all the available information in reconstructing the final state. In the near future plots of the reconstructed mass made

by constraining the η mass to be correct will be available. The Monte Carlo simulation program indicates that the mass resolution is improved by a factor of two by this constraint, and preliminary results indicate that this improved resolution may bring out some interesting effects.

The major limitation of this experiment was the background from the $\pi^0 \pi^0$ reaction. The measured feed-down probability of 4.5%, as discussed above, when corrected for the difference in acceptance for $\gamma \gamma$ and $\pi^0 \pi^0$ events, yields an actual feed-down probability of 3.1% for the 13 GeV/c runs and 3.25% for the 8.5 GeV/c runs. Unfortunately this was not good enough to obtain the sensitivity needed to observe the true high mass $\gamma \gamma$ signals, which should exist at a level one to two orders of magnitude smaller than our limit. All evidence points to our major problem being the loss of low-energy photons in the veto counters. There are two ways this problem can be suppressed. If the beam energy is raised, the energy of the photons from π^0 decay also increases, making them easier to detect. The π^0 feed-down probability should be inversely proportional to the beam momentum, and therefore the background in the $\gamma \gamma$ mass spectrum should drop inversely proportional to the square of the beam momentum. Unfortunately the cross section for the production of most particles falls with increasing beam energy.

A more direct method of detecting the low-energy photons, and thus eliminating the background, is simply to use a better detector. Such a photon detector should have a high efficiency for the detection of low-energy photons, but need not have good energy or spatial resolution. It should also have good time resolution, since some of the veto counters are hit by the reaction by-products of essentially every beam interaction.

Appendix A
SOLVING HODOSCOPE COUNTER OVERLAP PROBLEMS

This appendix will describe the procedures invoked when several showers were connected by hodoscope peaks. This processing was only necessary to obtain good pattern recognition efficiency for π^0 's and other particles with two or more photons close together on the detector arm. Therefore none of what is described below is relevant to the $\gamma\gamma$ analysis.

Each match between a hodoscope peak and a shower was entered into a table. For instance, a hodoscope peak that intersected two showers was entered twice into the table, with each entry roughly representing a possible photon assignment. The pulse height correction for attenuation in the hodoscope counters was made using individually measured attenuation curves for each counter interpolated to the shower position. The resulting corrected pulse height was stored in the table.

After all entries were made, the table was broken into connected groups, which were groups of entries in the table of intersections that were all linked to one another, either by common showers or common peaks. Attempts were then made to identify false entries and remove them from the list. A few typical connected groups of intersections are shown in Figure 52, in which the straight lines represent hodoscope peaks and the circles represent showers.

The first selection was made on the basis of pulse height and was applied to connected groups with more than one shower as well as to groups with a single shower that had more than two peaks in either dimension. Both the horizontal and vertical hodoscopes should have seen the same number of electrons and positrons from the shower and thus have had the same pulse height. The corrected pulse heights of

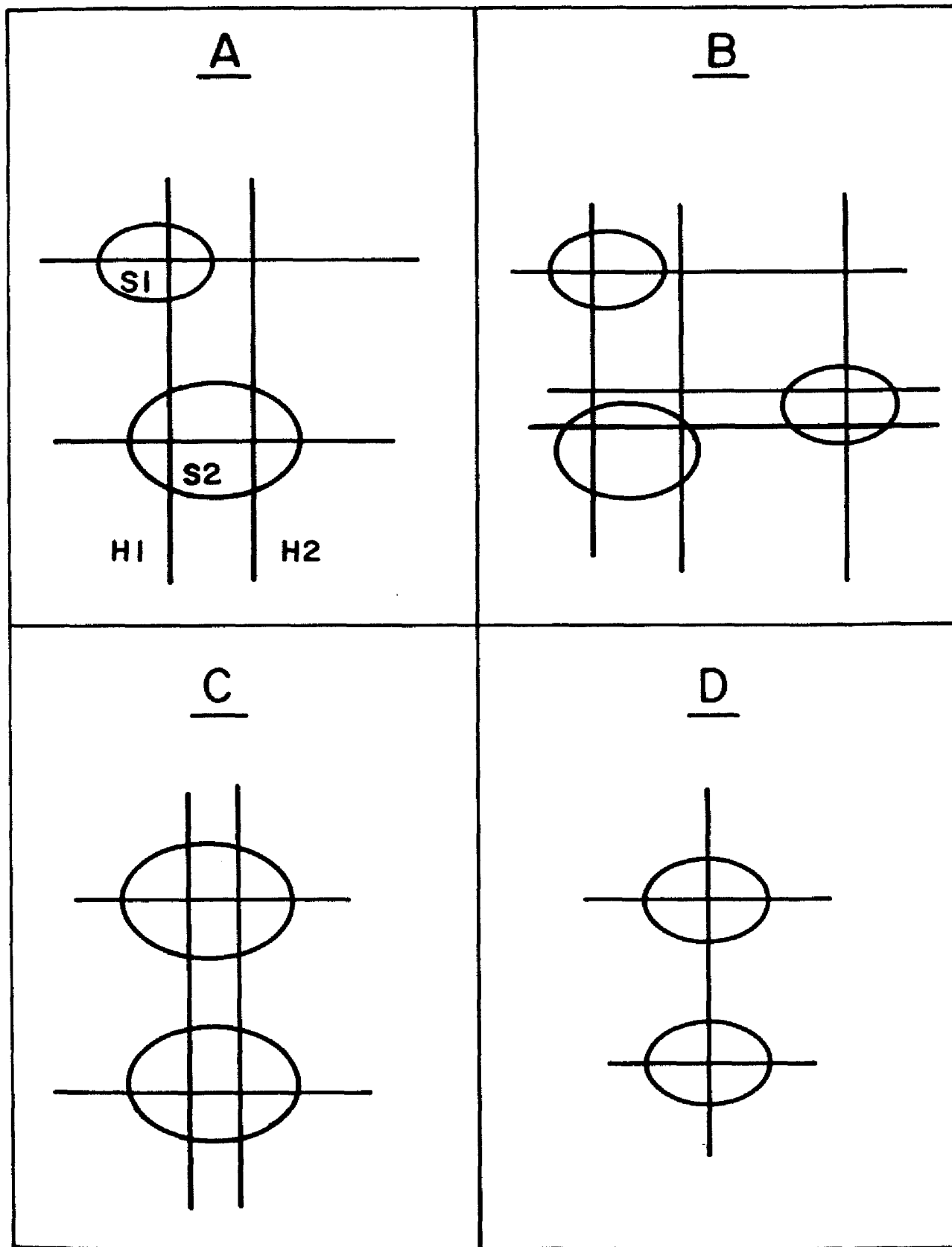


Figure 52 Typical Hodoscope Peak Groupings

all hodoscope peaks assigned to a shower were compared, and an intersecting peak was eliminated if its pulse height did not match that of any other peak in the other dimension within a factor of 7. This was a very loose cut.

The remaining entries in the table of overlaps between hodoscope peaks and showers were then rearranged into connected groups and submitted to a second selection routine. This routine made "topological" selections, eliminating hodoscope peak intersections with showers that did not appear consistent with the other intersections within the group. Figure 52.A shows a simple and common example of the type of problem solved by this procedure. Clearly in this example peak H1 belongs to shower S1 and peak H2 belongs to shower S2. To describe the decision-making process used to make such selections some simple jargon must be defined:

An "exclusive peak" was a hodoscope peak that overlapped only one shower.

A "conflicting peak" was a hodoscope peak that overlapped more than one shower.

Ideally all hodoscope peaks would have been exclusive. Likewise all showers would have had an equal number of exclusive peaks in each dimension. The following selection rules were used to determine which peaks could be removed, thereby creating a more ideal situation. If a shower had an exclusive peak in a particular dimension and also had any number of conflicting peaks in that same dimension, those conflicting peaks were candidates for elimination. Candidates for elimination were removed if they overlapped just one other shower and that shower had no exclusive peaks in the same dimension. Situations such as shown in Figure 52.A and Figure 52.B were completely resolved by this procedure.

There were a few other common ambiguities that still remained, some of which are shown in Figure 52.C and Figure 52.D. To resolve

these ambiguities the list of remaining overlaps between hodoscope peaks and showers was again broken into connected groups and submitted to a third selection process. This process acted only on two special types of cases, the simplest examples of which are shown in Figures 52.C and 52.D. In cases such as Figure 52.C the peak assignments that provided the best matches to the pulse heights in the other dimension were kept. In the case shown in Figure 52.D, which was clearly caused by the overlap of two photons within one hodoscope peak, both intersections would be kept and the pulse height of the peak would be split proportional to the pulse heights in the other dimension of each shower. Any remaining connected groups of hodoscope peaks were not broken up, but the pulse heights of the affected peaks were divided among the showers proportional to the energy deposited in the front and rear lead glass walls.

Appendix B

TUNING THE VETO COUNTER CUTS

This appendix will describe the tests that were performed to determine the best cuts for the veto counters. Figure 53 shows histograms of the TOF distributions in the three types of veto counters for data events. The task of the analysis program was to eliminate events with real signals in these counters without too much loss of good events. In this appendix the charged particle vetoes will be referred to as the "A" vetoes, the target box vetoes will be referred to as the "S" vetoes, and the downstream photon vetoes will be referred to as the "I" vetoes.

B.1 Tuning the Veto Time of Flight Windows

Figure 54 displays the expected efficiency and background as a function of the upper and lower TOF window edges for the I and S veto counters. In each of the four cases we see that the background level remains flat with the cut far away from the interaction time and takes a sudden jump near the interaction time as the veto counters become inefficient. As the window was widened, the chance of vetoing on an out-of-time interaction was increased and the efficiency was correspondingly reduced. The slopes of the efficiency curves were used to determine the benefits of widening or narrowing the TOF windows. For the upper edge of the windows the efficiency changed 1-2% per nano-second of change. For the lower edge the efficiency changed .2-.4% per nano-second of change. I chose a TOF window of -4 to 4 ns for the I vetoes and -2 to 1 ns for the S vetoes.

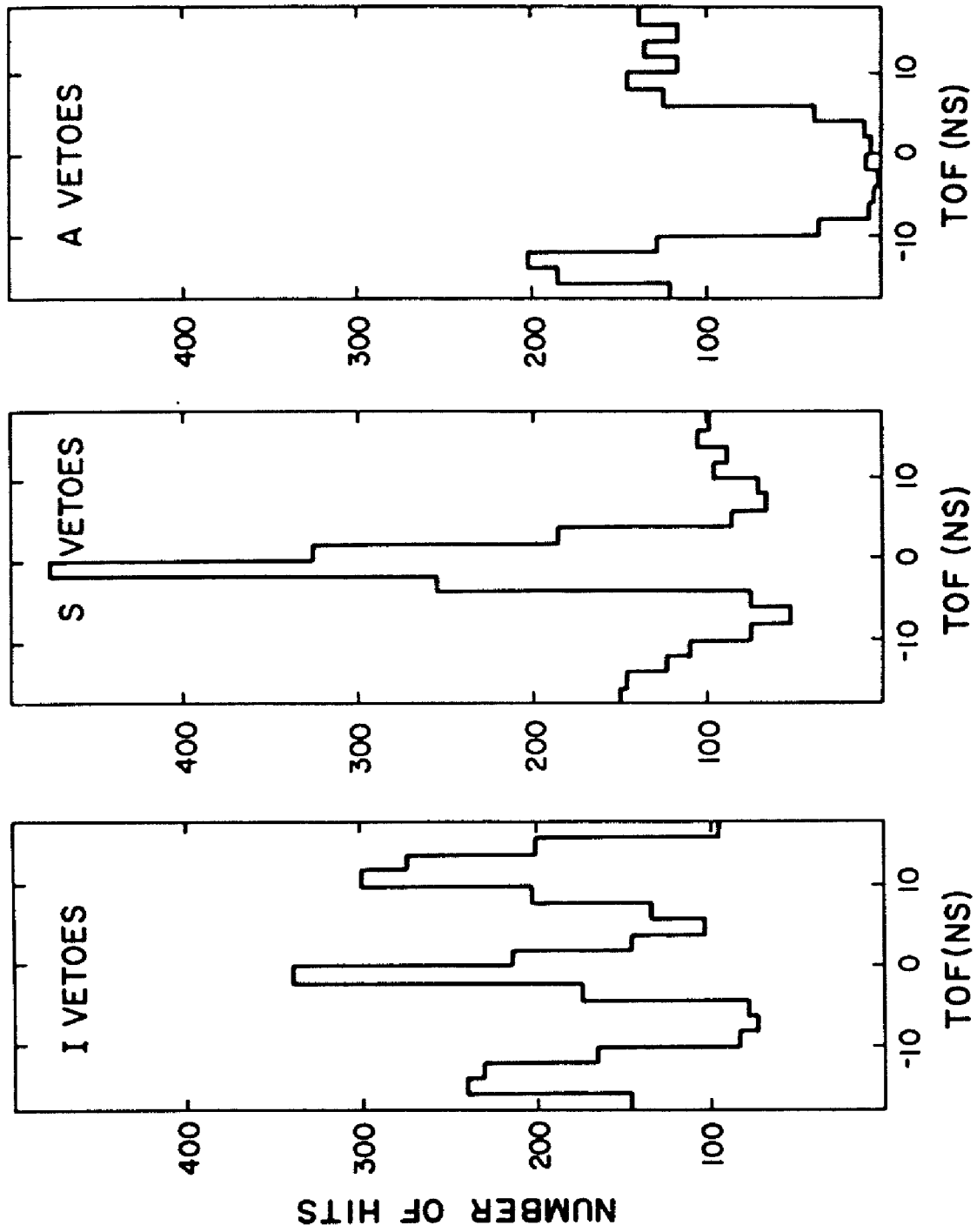


Figure 53 Veto Counter TOFs in Data Triggers

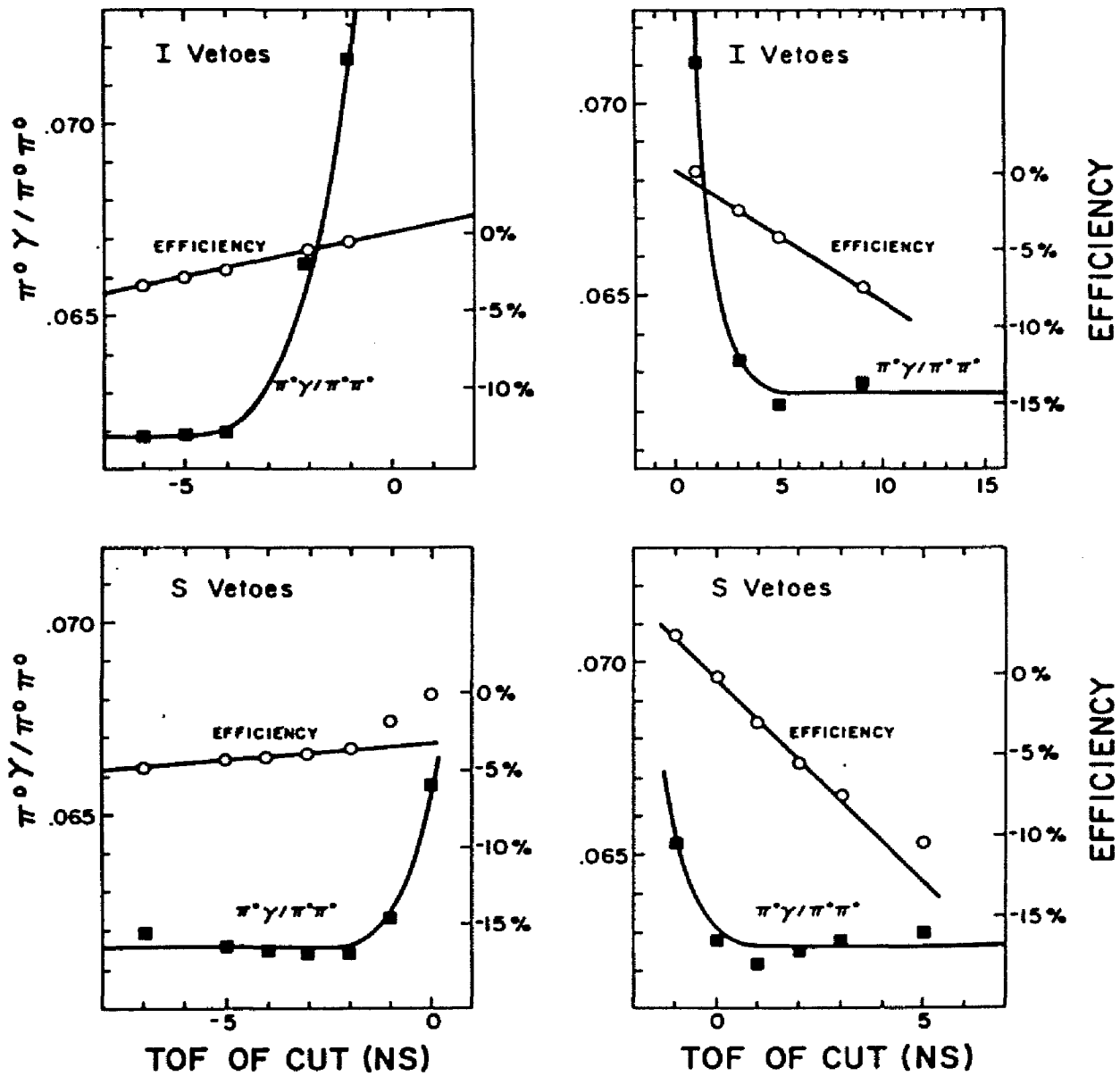


Figure 54 Efficiency and Background vs. I and S Veto Counter TOF Cuts

B.2 Investigation of Uses of the ADC and Latch Information

In the tests described below the "standard" veto cut for the I and S vetoes used only the TOF information. The windows used were the same as those chosen above. The standard A veto cut used both the latch and TOF information. An event was vetoed if it had an A veto hit with both a latch bit set and a TOF within the window of -6 to 6 ns.

The first four entries in Table 28 show the results obtained, first with all the veto cuts in effect, and then with each of the three types of veto cut removed. The A vetoes were clearly unimportant, vetoing only .15% of the dirty $\pi^0 \pi^0$ events and an unmeasurable fraction of the $\pi^0 \gamma$ events. The I vetoes were the most important vetoes for reducing the background. They reduced the background level by 51% while decreasing the efficiency by only 8.7%. The S vetoes showed some effect, by reducing the background levels by 6%, but the price paid in the efficiency was 7%.

A large fraction of the I veto counter hits with a latch signal had a measured TOF of zero. These hits were caused by two particles hitting the veto counter, one very early that stopped the TDC, and one that came later and set the latch bit. The later hit could have been a real hit, which we wanted to veto. The results labeled "test A" in Table 28 were obtained by vetoing events that had an I veto counter with a TOF of less than -20 ns and a latch bit set. There was a clear improvement in the background levels.

The next question regarded the proper use of the ADC information. In order to minimize accidental vetoing we could have required the veto counter to have a pulse height above a certain threshold before vetoing the event. Tests G and H indicated that the use of the S veto ADC information had no measurable effect. Tests B - E studied this effect in the I vetoes. There was a clear effect, but the best results were obtained with no pulse height requirements in the I vetoes.

TABLE 28
Veto Cut Performance

Conditions	PIPI	PIGAM	PIPI/DPIPI	PIGAM/PIPI
Normal Veto Cut	2632	161	0%	0%
No I Veto Cut	2860	264	8.7%	50.0%
No S Veto Cut	2819	183	7.1%	6.0%
No A Veto Cut	2636	161	0%	0%
Test A (See Below)	2501	146	-5.0%	-4.6%
Test B (See Below)	2568	153	-2.4%	-2.6%
Test C (See Below)	2571	155	-2.3%	-1.5%
Test D (See Below)	2574	155	-2.2%	-1.6%
Test E (See Below)	2587	160	-1.7%	1.0%
Test F (See Below)	2504	146	-4.9%	-4.7%
Test G (See Below)	2503	146	-4.9%	-4.7%
Test H (See Below)	2505	146	-4.8%	-4.7%
Test I (See Below)	2530	150	-3.9%	-3.1%
Test J (See Below)	2528	146	-4.0%	-5.6%
Test K (See Below)	2428	140	-7.8%	-5.7%

Test A	-	I vetoes on latch with TOF < -20 ns
Test B	-	I vetoes on latch with TOF < -20 ns All I vetoes require PH > 20 All S vetoes require PH > 30
Test C	-	I vetoes on latch with TOF < -20 ns All I vetoes require PH > 30 All S vetoes require PH > 30
Test D	-	I vetoes on latch with TOF < -20 ns All I vetoes require PH > 40 All S vetoes require PH > 30
Test E	-	I vetoes on latch with TOF < -20 ns All I vetoes require PH > 50 All S vetoes require PH > 30
Test F	-	I vetoes on latch with TOF < -20 ns, PH > 30 S vetoes on latch with TOF > 150 ns All S vetoes require PH > 30
Test G	-	I vetoes on latch with TOF < -20 ns, PH > 30
Test H	-	I vetoes on latch with TOF < -20 ns, PH > 30 All S vetoes require PH > 30
Test I	-	I vetoes on latch with TOF < -40 ns, PH > 30
Test J	-	I vetoes on latch with TOF < -30 ns, PH > 30
Test K	-	I vetoes on latch with TOF < -10 ns, PH > 30

Since the latch cut was effective in the I vetoes, the same was

tried for the S vetoes. These counters had a different brand of TDC, which responded differently to early hits. The proper thing to do in this case was to veto on latch hits with TDC overflows. No measurable improvement was observed in test F and H.

It appears that the original latch cut in test A was the most effective cut. Tests H, I, J, and K show the effect of moving the TOF threshold for this cut. The results are plotted in Figure 55. The background seems to level off at a TOF of about -25 ns, while the efficiency begins to drop. I therefore chose a final I veto latch cut with TOF less than -25 ns.

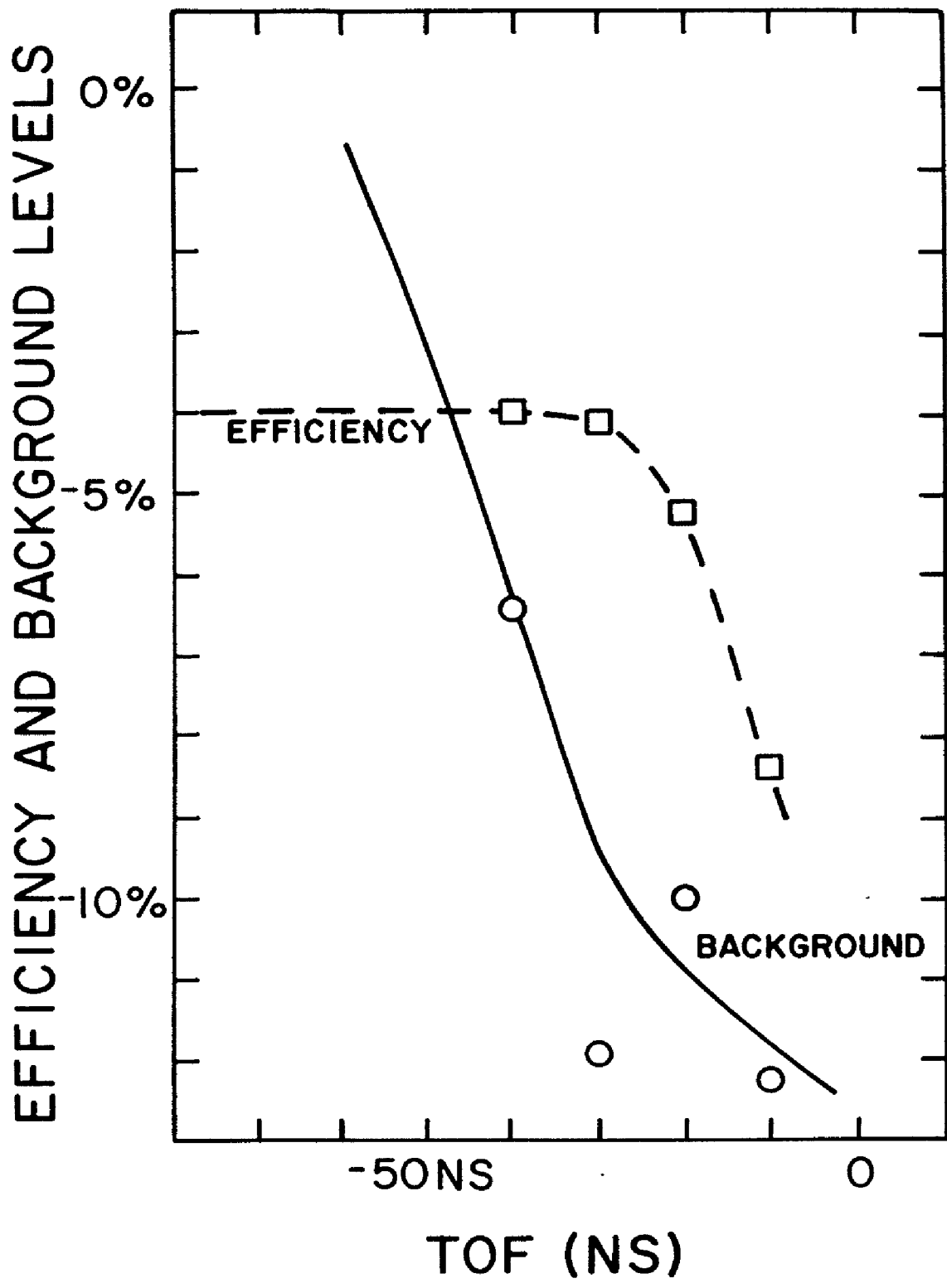


Figure 55 Efficiency and Background vs. TOF Threshold on Veto Counter Latch Cut

Appendix C

TUNING THE EXTRA HODOSCOPE COUNTER PEAK CUTS

In this appendix I will describe the methods used to establish the cuts based on extra hodoscope peaks. No check was made to determine if these peaks were associated with an extra calorimeter hit, but since essentially all extra calorimeter hits caused the elimination of the event, the cuts described here only apply to events without extra calorimeter hits.

Extra hodoscope peaks were divided into categories based on their dimension and the number of hodoscope counters in each peak. The term "horizontal peak" refers to a peak in the hodoscope plane with horizontal counters, and likewise for the "vertical peaks". I divided the peaks into the following five categories, each of which was subjected to a different cut.

- 1) Horizontal peaks with 1 counter
- 2) Horizontal peaks with more than 1 counter
- 3) Vertical peaks with 1 counter
- 4) Vertical peaks with more than 1 counter
- 5) Pairs of horizontal and vertical hodoscope peaks matching in pulse height

The TOF distributions of all four categories of hodoscope peaks were similar. A sample plot is shown in Figure 56. In all cases I required the hodoscope peak TOF to be within the window of -6 to 6 ns if the event was to be vetoed. Those peaks with a TOF outside of this window were ignored, while the peaks with TOF within the window were subjected to a pulse height cut. If the pulse height threshold was exceeded by an extra hodoscope peak, the event was rejected as being likely to contain an extra photon.

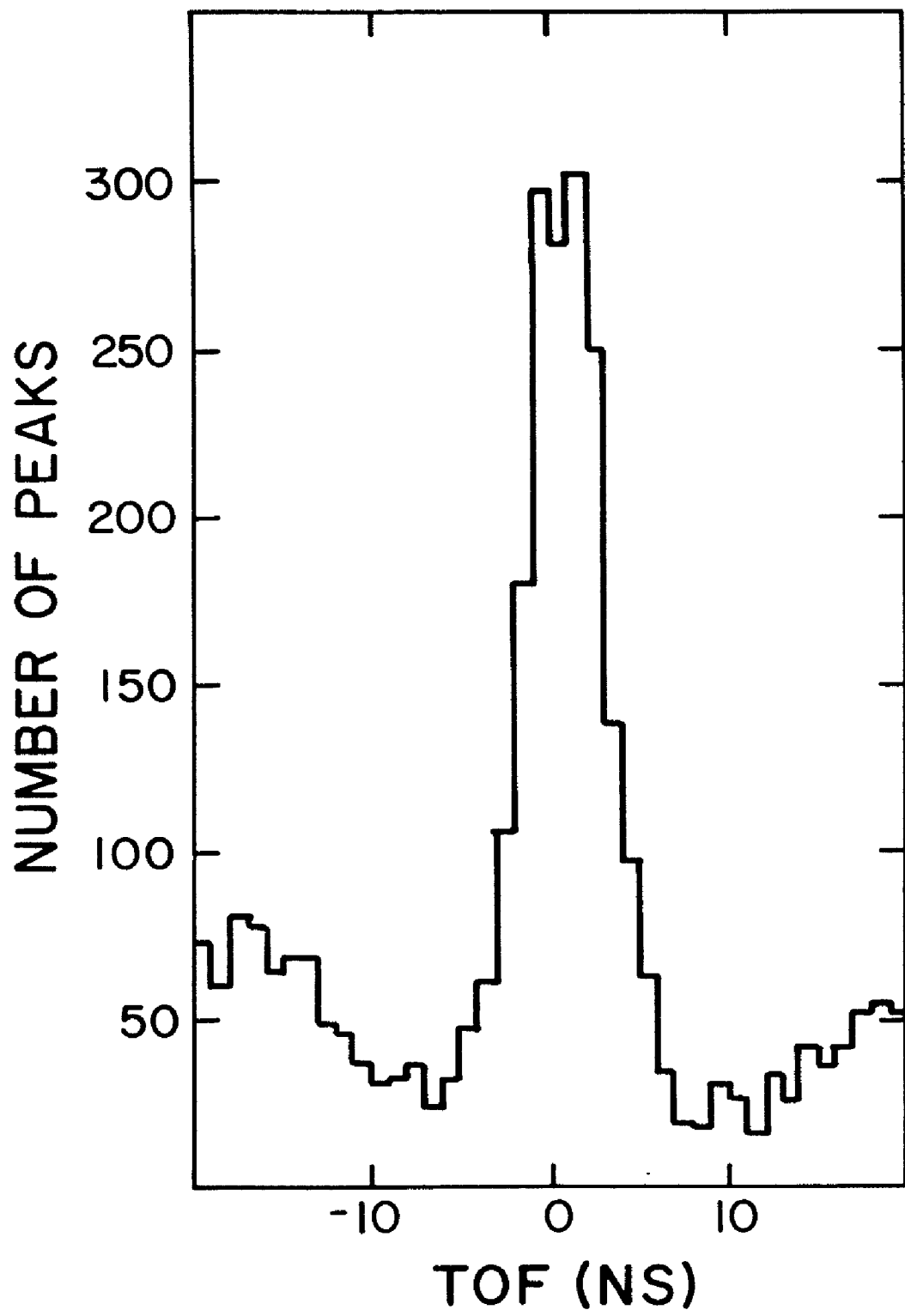


Figure 56 TOF of Extra Hodoscope Peaks

C.1 Cuts on Extra Hodoscope Peaks with More Than One Counter

The best improvement in the quality of the analysis was obtained by cutting on extra horizontal hodoscope peaks with two or more counters, as is shown in Figure 57. These peaks indicated the presence of a photon that converted too early to penetrate to the rear lead glass wall, and whose front wall energy was assigned to another shower. The data indicate that these were all large pulse height peaks, with none having a pulse height less than 24 ADC counts. I picked a cut of 24 ADC counts, where I expected a 16.5% improvement in the statistical significance of the $\gamma\gamma$ signals with only a 1.5% loss in efficiency.

Because of the asymmetry of the geometry of the front lead glass wall, it was expected that the vertical hodoscope peaks would play a lesser role in distinguishing multiple photon showers of the type described above. The test results showed no change in the background levels in response to a cut on the vertical peaks. No cut was made on these extra hodoscope peaks.

C.2 Cuts on Extra Hodoscope Peaks with One Counter

The extra hodoscope peaks with only one counter were expected to identify a different sort of photon than those described above. In this case the photon was expected to be of very low energy. Photons of this low an energy were difficult to detect. If they were detected, what was observed was often only one electron or positron in a single layer of the detector. In the hodoscope a single electron was expected to give a signal of about 7 ADC counts.

Figure 58 shows the expected efficiency and background levels as a function of this cut for extra peaks in both dimensions. It is clear that the cuts did indeed lower the background levels, but unfortunately the efficiency fell steeply as the cut was tightened. I chose a cut at a pulse height of 25 ADC counts, where I expected a modest

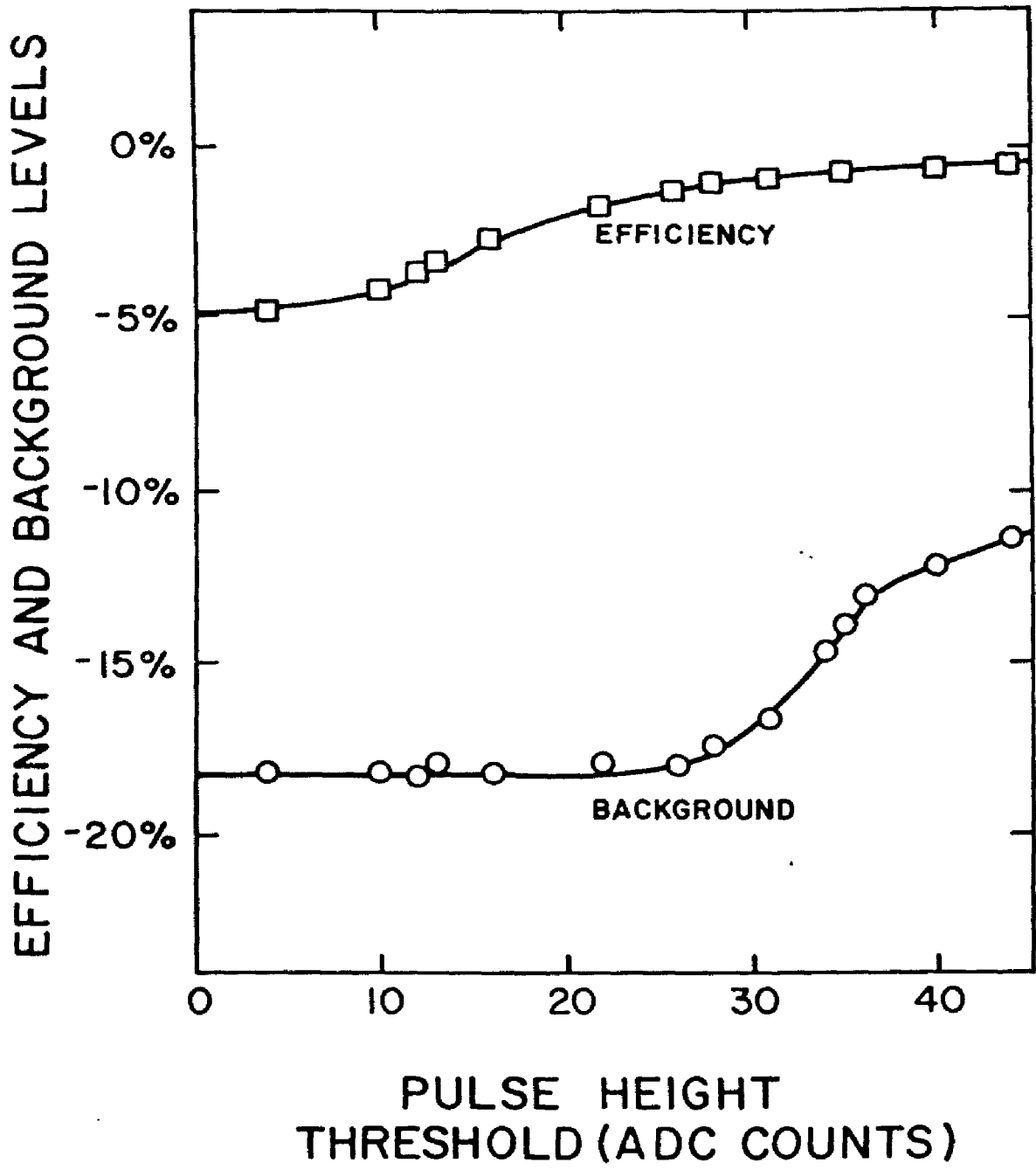


Figure 57 Efficiency and Background vs. Cut on Pulse Height of Extra Two Slit Horizontal Hodoscope Peaks

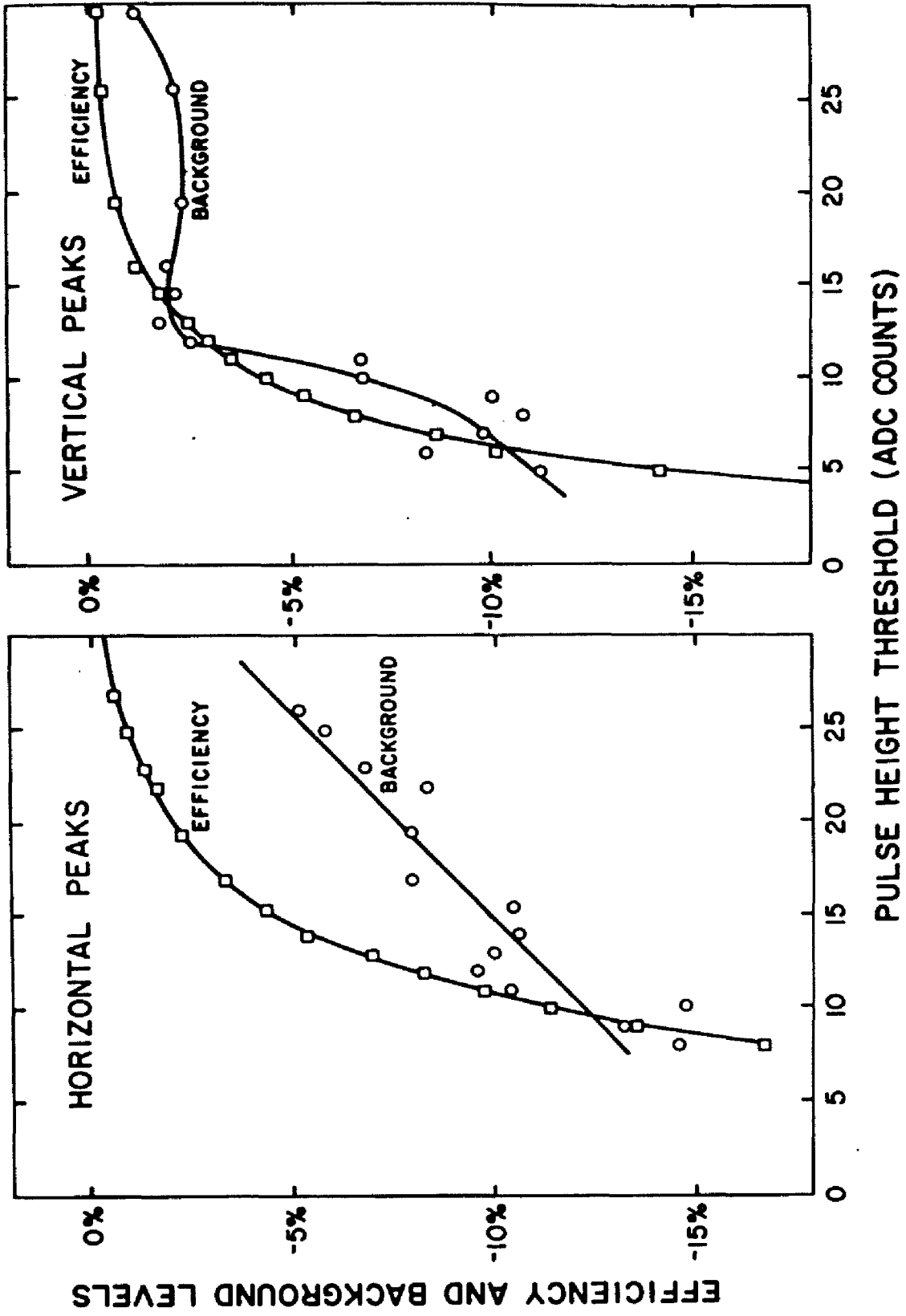


Figure 58 Efficiency and Background vs. Cut on Pulse Height of
Extra One Slant Hodoscope Peaks

6% increase in the statistical significance of any $\gamma\gamma$ signals with a 1% loss in efficiency.

C.3 Cuts on Extra Hodoscope Peak Pairs

The final cut using the extra hodoscope peaks was on pairs of peaks that matched in pulse height. Figure 59 shows the estimated efficiency and background as a function of a cut based on the sum of the pulse heights of the two peaks. I placed the cut at a pulse height of 28 ADC counts, where I expected to obtain a 6% improvement in the statistical significance of the $\gamma\gamma$ signals with a 1% loss in efficiency.

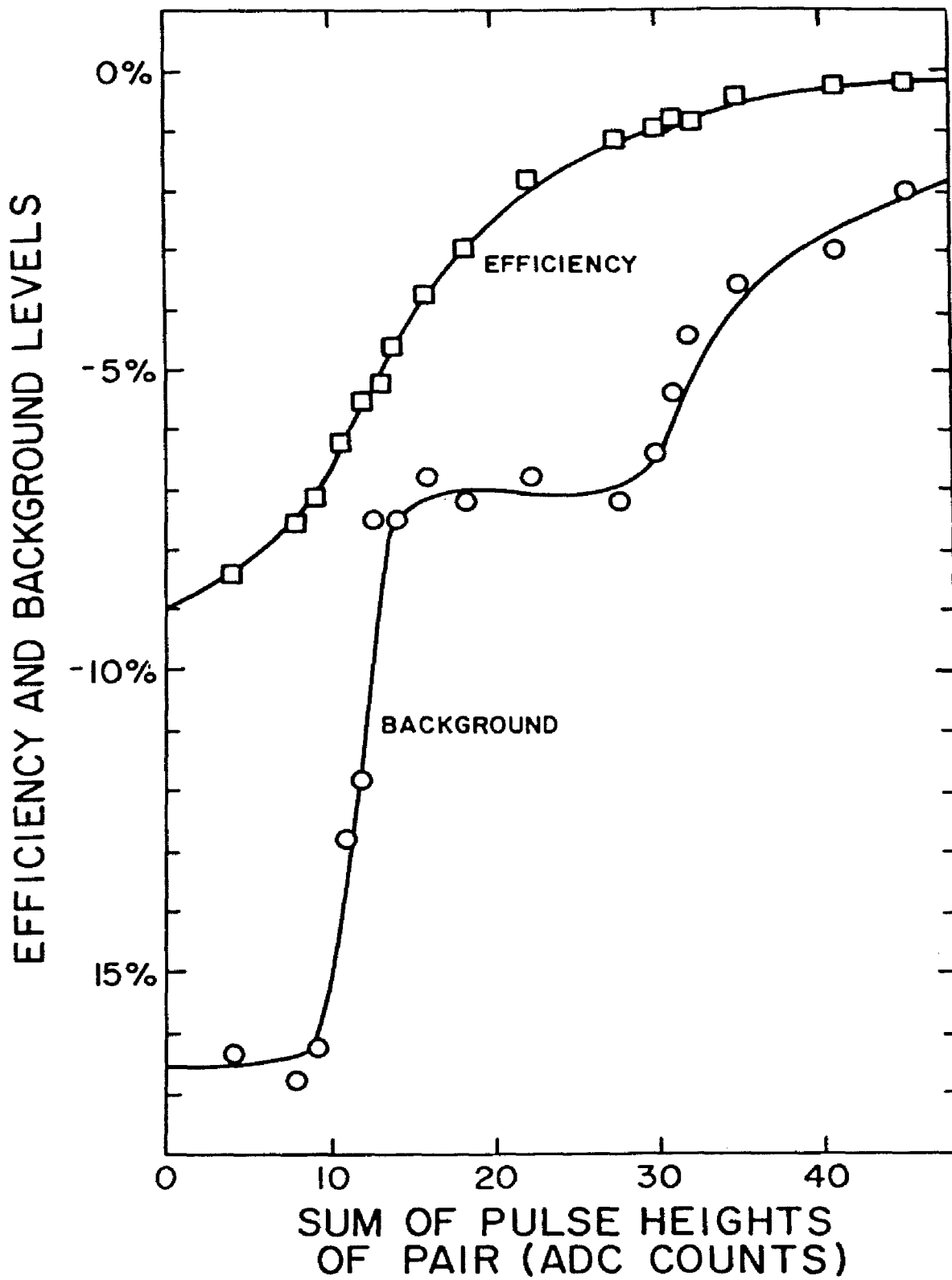


Figure 59 Efficiency and Background vs. Cut on Sum of Pulse Heights of Extra Hodoscope Peak Pairs

Appendix D
TUNING THE EXTRA FRONT WALL SHOWER CUT

This appendix will describe the results of studies done to determine the best way to treat events with a "lone front wall shower". These showers had no overlapping rear wall or hodoscope counter hits but may have had overlapping calorimeter hits.

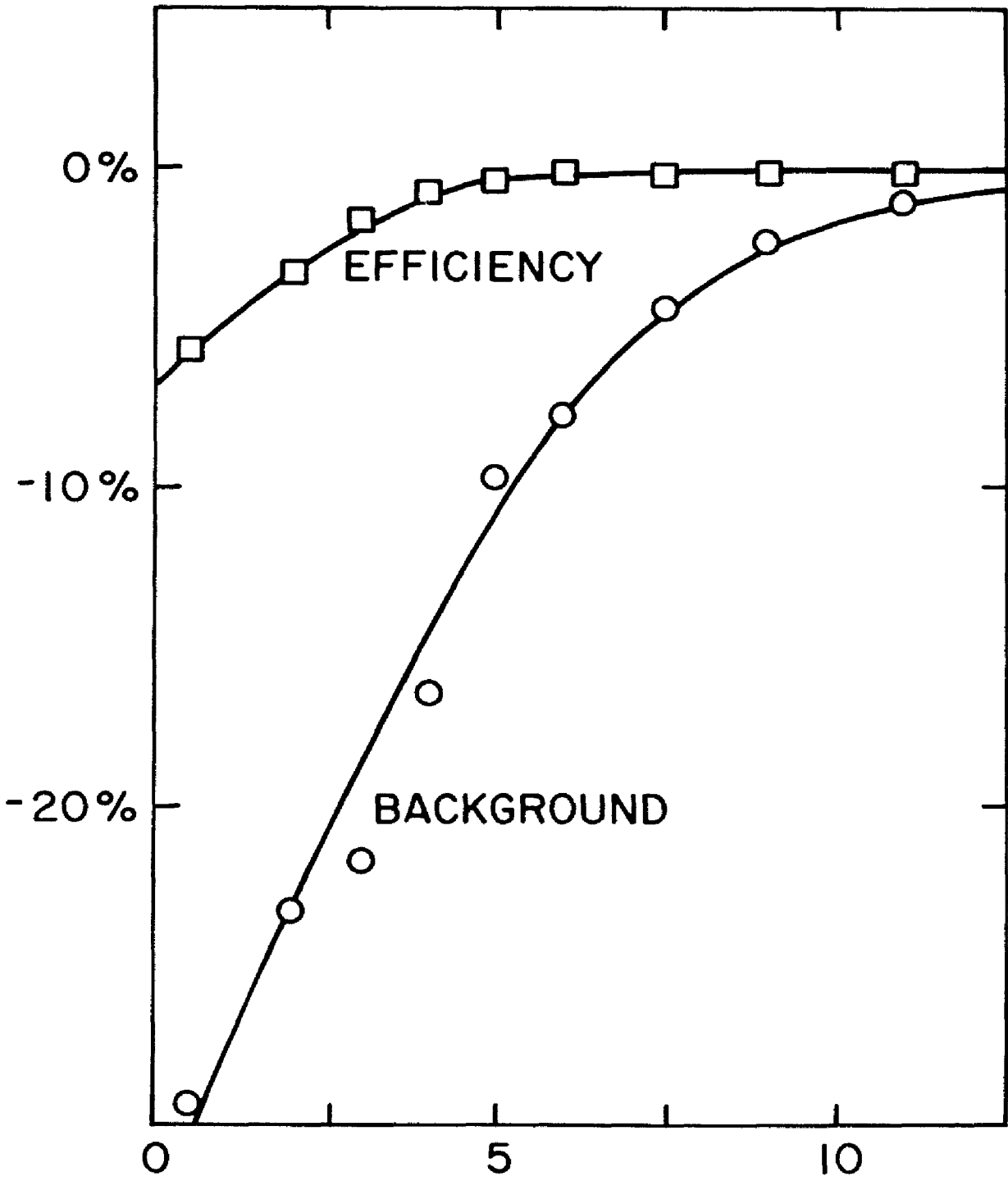
The lone front wall showers were divided into two categories based on whether or not the shower had overlapping calorimeter hits. Essentially all such showers consisted of a single hit block. Each category will be subject to a different cut. The two categories are:

- 1) Front wall shower with calorimeter hits
- 2) Front wall shower without calorimeter hits

If the shower had calorimeter hits, the TOF information of those counters was used rather than the TOF information of the front wall blocks. For such showers the TOF of one calorimeter counter was required to be within the window of -7 to 7 ns if the event was to be rejected. Roughly 10% of the showers failed this cut and were ignored. Figure 60 shows the estimated efficiency and background as a function of a cut based on the pulse height of the front wall blocks in such a case. It is clearly best to veto all such events regardless of pulse height. Using this cut, I expected an improvement of 20% in the statistical significance of any $\gamma\gamma$ signal with only a 6% loss in efficiency.

In the case of lone front wall showers without calorimeter hits, the TOF information of the lead glass block was used. Figure 61 shows the TOF distribution in the front lead glass wall for such showers. The TOF of one block in the shower was required to be within the window of -10 to 8 ns if the event was to be rejected. If this condition was not met, the shower was ignored. These showers were

EFFICIENCY AND BACKGROUND LEVELS



PULSE HEIGHT
THRESHOLD (ADC COUNTS)

Figure 60 Efficiency and Background vs. Pulse Height Cut on Front Wall Showers with Cal. Hits

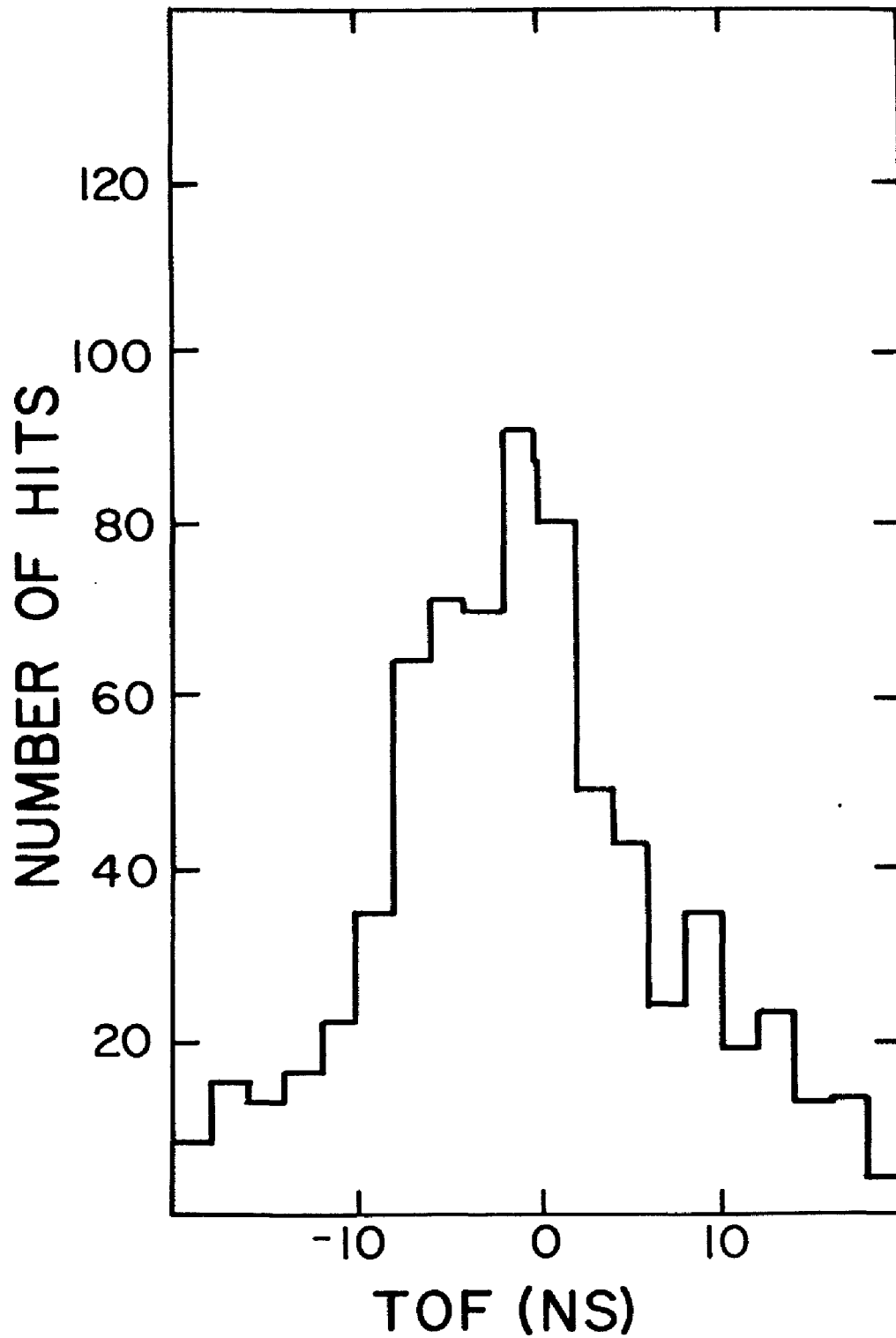


Figure 61 TOF of Front Lead Glass Wall Counters for Lone Front Wall Showers without Cal. Hits

subjected to a pulse height cut, and the estimated efficiency and background levels as a function of this cut are shown in Table 29. There was clearly some improvement in the background levels, but the price paid in the efficiency was too high. I decided not to reject events due to the presence of these showers.

TABLE 29

Efficiency and Background vrs Cut on Lone Front

Wall Shower Pulse Height

<u>Cut Threshold</u>	<u>Efficiency</u>	<u>Background</u>
.5 ADC counts	-13.7%	-11.8%
2 ADC counts	-9.4%	-9.0%
3 ADC counts	-5.5%	-3.4%
4 ADC counts	-2.4%	-.1%
5 ADC counts	-1.1%	0%

Appendix E
PROCESSING OF LONE REAR WALL LEAD GLASS SHOWERS

Showers that consisted of only rear lead glass blocks were difficult to explain. It was very unlikely that a real photon could have penetrated to that depth in the detector without converting. This was confirmed by the fact that these showers were present in only a few percent of the reconstructed π^0 s. Approximately 8% of the data triggers contained such showers. More than 92% of these showers consisted of a single hit rear lead glass block. Figure 62 shows the TOF measured in the rear lead glass wall for these showers with and without the requirement of overlapping calorimeter hits. There is a clear in-time peak, which is only slightly reduced by requiring the presence of a calorimeter hit.

The test results presented here differ from the previous tests in that all the data were used. This allowed the background levels to be predicted using the $\gamma \gamma$ events. To be considered real the TOF of the rear lead glass block was required to be within the window of -7 to 5 ns. Showers with TOFs outside of this window were ignored. The test results indicated that roughly 1.3% of the $\pi^0 \pi^0$ events and 4.7% of the $\gamma \gamma$ events would be eliminated if such showers were considered to be real.

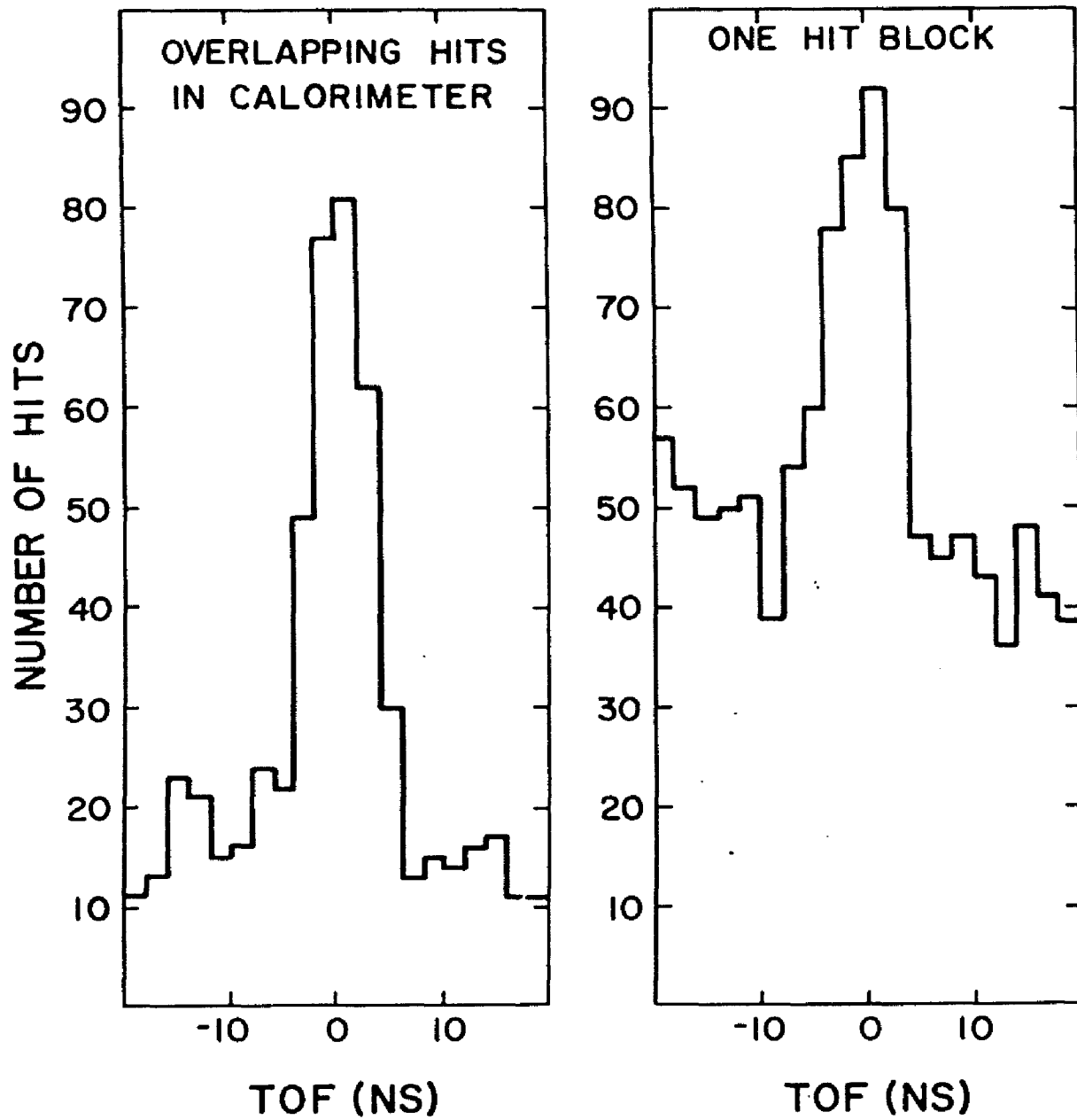


Figure 62 TOF in Rear Lead Glass Wall for Lone Rear Wall Showers